Analysis of Civil Aircraft Propulsors with Boundary Layer Ingestion

by

David Kenneth Hall

B.S.E., Duke University (2008)
S.M., Massachusetts Institute of Technology (2011)

Submitted to the Department of Aeronautics and Astronautics
in partial fulfillment of the requirements for the degree of

Doctor of Philosophy in Aeronautics and Astronautics

at the

MASSACHUSETTS INSTITUTE OF TECHNOLOGY

February 2015

Signature redacted

Author ....
Department of Aeronautics and Astronautics
January 14, 2015

Certified by....... Signature redacted ....
Edward M. Greitzer
H.N. Slater Professor of Aeronautics and Astronautics
Thesis Committee Chair

Signature redacted

Certified by.. ....
Choon Sooi Tan
Senior Research Engineer
Thesis Committee

Signature redacted

Certified by.............. ....
Mark Drela
Terry J. Kohler Professor of Fluid Dynamics
Thesis Committee

Signature redacted

Certified by.............. ....
Nicholas A. Cumpsty
Professor Emeritus, Imperial College
Thesis Committee

Signature redacted

Accepted by.......... ....
Paulo Lozano
Associate Professor of Aeronautics and Astronautics
Graduate Committee Chair

Analysis of Civil Aircraft Propulsors with Boundary Layer Ingestion

by

David Kenneth Hall

Submitted to the Department of Aeronautics and Astronautics
on January 14, 2015, in partial fulfillment of the
requirements for the degree of
Doctor of Philosophy in Aeronautics and Astronautics

Abstract

This thesis describes (i) guidelines for propulsor sizing, and (ii) strategies for fan turbomachinery conceptual design, for a boundary layer ingesting (BLI) propulsion system for advanced civil transport aircraft. For the former, configuration performance analysis shows BLI yields a reduction in mechanical power required to propel a given aircraft. For the latter, fan turbomachinery design attributes are identified to mitigate the impact of BLI inlet distortion on propulsor performance.

The propulsion system requirements are determined using a mechanical energy analysis, in which the performance of the airframe and propulsor are characterized in terms of sources and sinks of power. Using this framework, the propulsor can be sized based on the performance of the isolated airframe. Analysis of the power savings due to BLI (from reduction of viscous dissipation both in the aircraft wake and the propulsor jet) leads to scaling choices for the sizing of propulsor simulators for wind tunnel experiments to assess BLI benefit.

Fan stage distortion response is assessed computationally for a range of turbomachinery design parameters and for distortions characteristic of BLI. The numerical results show the importance of three-dimensional flow redistribution upstream of the fan, and indicate that, for the parameters examined, non-axisymmetric fan stators have the largest effect on decreasing blade row velocity distortions and thus mitigating losses due to flow non-uniformity.

Thesis Committee Chair: Edward M. Greitzer
Title: H.N. Slater Professor of Aeronautics and Astronautics

Thesis Committee: Choon Sooi Tan
Title: Senior Research Engineer

Thesis Committee: Mark Drela
Title: Terry J. Kohler Professor of Fluid Dynamics

Thesis Committee: Nicholas A. Cumpsty
Title: Professor Emeritus, Imperial College

Acknowledgments

There are many people to acknowledge for their contributions to the work that ultimately resulted in this thesis. First, I'd like to thank my advisors, Professor Ed Greitzer and Dr. Choon Tan. Their guidance, both in technical matters and in how to conduct effective research, has been nothing short of excellent. Working with them has been a pleasure, and I look forward to continuing to do so in the future. The guidance of Professor Mark Drela and Professor Nick Cumpsty also deserves special recognition; although my interactions with them were less frequent than with the other half of my thesis committee, their technical insight and advice over the years has been no less valuable. I'd also like to thank Professor Zoltán Spakovsky and Dr. Alejandra Uranga for serving as readers on my thesis defense committee and for their helpful comments on drafts of this thesis.

This research was carried out as part of the NASA Fixed Wing Project under Cooperative Agreement NNX11AB35A. I gratefully acknowledge the financial support of the NASA Fundamental Aeronautics Program, as well as the use of the NASA R4 fan geometry used in Chapter 5.

My work benefited from technical discussions with various experts in the field outside of MIT. In particular, I'd like to mention Alan Epstein, Wes Lord, and Jayant Sabnis of Pratt & Whitney, Greg Tillman of United Technologies Research Center, and John Adamczyk, Randy Chriss, and Michael Hathaway of NASA.

I'm thankful to have been able to participate in such an ambitious and exciting research endeavor. The success of the project is a testament to the hard work and professionalism of the MIT N+3 team members: Cécile Casses, Alex Espitia, Adam Grasch, Arthur Huang, Michael Lieu, Dr. Sho Sato, Nina Siu, Dr. Neil Titchener, Dr. Alejandra Uranga, and Elise van Dam. It has been a joy working with all of them.

For the last six years, the Gas Turbine Lab has been something of a second home for me, and there are many members of the GTL who have helped along the way. First, I'd like to thank the members of "Team Body Force," Max Brand, Dr. Jeff Defoe, Anjaney Kottapalli, Dr. Claudio Lettieri, Dr. Andreas Peters, and Will Sorensen, each of whom at some point provided assistance in understanding and implementing the source term (or "body force") method described in Chapter 5. Second, I'd like to thank my fellow GTL network administrators, Jeff Defoe, Andreas Peters, David Clifton, and Andras Kiss; special

thanks also to Professor Spakovszky for giving me the opportunity to give something back to the lab while learning a useful new skill by serving in this capacity. Third, I'd like to mention the other (former) PhD candidates who at one point occupied desks in 31-259, Dr. Jon Everitt, Dr. Andreas Peters, and Dr. Sho Sato (the other member of "Team Power Balance"), for daily interactions both technical and non-technical. I'd also like to thank Robin Courchesne-Sato, without whom work at the GTL would certainly grind to a halt.

Finally, I'd like to thank my friends and family for keeping me going as I pursued my degree. I've made many great friends during my time in Cambridge, and I'd like to specifially mention Leah, Juan, Bill, Ronan, Katie, Sarah, Rob, and Kevin for their friendship over the years. Last but not least I'd like to thank my family, both here in Massachusetts and from back home in North Carolina, especially Papa, Christine, Mom, and Dad, for their constant love and support.

Contents

List of Figures

List of Tables

Nomenclature

A_{jet}	propulsor jet area
AR	blade aspect ratio
B	number of blades/vanes
c	chord
C_D	drag coefficient $(= D/(\frac{1}{2}\rho_\infty V_\infty^2 \mathcal{S}_{\text{ref}}))$
C_{P_K}	mechanical flow power coefficient $(= P_K/(\frac{1}{2}\rho_\infty V_\infty^3 \mathcal{S}_{\text{ref}}))$
C_X	net streamwise force coeffient $(= X/(\frac{1}{2}\rho_\infty V_\infty^2 \mathcal{S}_{\text{ref}}))$
C_Φ	dissipation coefficient $(= \Phi/(\frac{1}{2}\rho_\infty V_\infty^3 \mathcal{S}_{\text{ref}}))$
D	drag force
D_i	induced drag
DF	diffusion factor
d_{fan}	fan diameter
$\dot{\mathcal{E}}$	mechanical energy deposition rate
$\dot{e}$	energy source term
F	thrust force
$\boldsymbol{f}$	momentum source term
f_ℓ	flow-parallel momentum source
f_n	flow-normal momentum source
f_{BLI}	boundary layer ingestion fraction
H	circumferential average annulus height
H^*	boundary layer kinetic energy shape factor $(= \theta^*/\theta)$
h	annulus height
h_t	stagnation enthalpy
$\dot{\mathcal{K}}$	mechanical energy flux
L	axial length

$\dot{m}$	propulsor mass flow rate
$\dot{m}_{\text{corr}}$	corrected mass flow $(= \dot{m}\sqrt{T_t/T_{\text{ref}}}/(p_t/p_{\text{ref}}))$
N_{eng}	number of engines or propulsors
$\hat{n}$	blade camber surface normal
P	circumferential average static pressure
P_t	circumferential average stagnation pressure
P_K	mechanical flow power
p	static pressure
p_t	stagnation pressure
q	dynamic pressure $(= \frac{1}{2}\rho V^2)$
R	annulus mean radius
r	radius
$\mathcal{S}$	area
T	static temperature
T_t	stagnation temperature
U_{tip}	fan tip speed $(= \Omega r_{\text{tip}})$
U, V	circumferential average axial, tangential velocities (Ch. 4)
u, v, w	Cartesian velocity components
u_e	boundary layer edge velocity
$\boldsymbol{V}$	velocity vector
V	velocity magnitude
$\boldsymbol{W}$	rotor relative velocity vector
W	rotor relative velocity magnitude
X	net streamwise force
x, y, z	Cartesian coordinates (x axial, $y = R\theta$ circumferential in Ch. 4)
x, r, θ	cylindrical coordinates
α	absolute flow angle
β	reduced frequency, rotor-relative flow angle
$\Delta C_{\Phi_{\text{prop}}}$	additional dissipation coefficient attributed to propulsor integration
δ	boundary layer thickness
δ_K	boundary layer kinetic energy excess thickness
η_f	fan efficiency

η_p	propulsive efficiency
θ	boundary layer momentum thickness (Ch. 3), circumferential coordinate (Ch. 4-6)
θ^*	boundary layer kinetic energy thickness
λ	local flow deviation angle
ξ	blade stagger angle
ρ	density
Φ	dissipation
ϕ	flow coefficient $(= V_x/(\Omega r_{\text{tip}}))$
ψ	stagnation enthalpy rise coefficient $(= \Delta h_t/(\Omega r_{\text{tip}})^2)$
ψ_{TT}	total pressure rise coefficient $(= \Delta p_t/(\rho(\Omega r_{\text{tip}})^2))$
Ω	rotor rotation rate

Acronyms

BLI	boundary layer ingestion
FPR	fan pressure ratio
PFEI	payload fuel energy intensity
PSC	power savings coefficient

Subscripts

fuse	fuselage
inl	propulsor inlet
out	propulsor outlet
surf	surface
TE	trailing edge
x	axial component
∞	free stream

Superscripts

$'$	non-BLI quantity (Ch. 3), perturbation quantity (Ch. 4)
$\overline{\quad}^{\theta}$	circumferential average

Chapter 1

Introduction

The concept of boundary layer ingestion (BLI) is illustrated in Figure 1-1. For conventional propulsion without BLI, the airframe drag, equal to the momentum deficit in the downstream wake, must be balanced by the engine thrust, equal to the excess momentum in the propulsor jet. The excess kinetic energy in both wake and jet are lost as viscous dissipation, resulting in additions to the propulsive power needed to produce the thrust. With BLI, a portion of the airframe boundary layer is passed through the propulsor, reducing the wake momentum deficit and jet kinetic energy. The condition of zero net momentum downstream is thus achieved with a reduction in wasted kinetic energy in the combined wake and jet flow, leading to decreased propulsive power and, ultimately, fuel burn.

A number of challenges exist in design and analysis of BLI aircraft configurations and their propulsion systems. One is that the definition of the propulsion system requirements becomes more difficult because the concepts of thrust and drag become ambiguous with

Figure 1-1: Boundary layer ingestion reduces wasted energy both in the wake of the airframe being propelled and in the jet downstream of the propulsor (adapted from Drela [1])

a tightly integrated propulsion system. The disturbance pressure field of the propulsor will alter the surface forces on the airframe, so the engine thrust requirement cannot be determined based on the drag of the isolated airframe. A second effect is that the ingested boundary layer flow enters the propulsor at reduced momentum flux, relative to free stream stagnation conditions typically seen at the engine inlet. Both these effects modify the power that needs to be added to the flow by the propulsor in order to maintain zero net force on the aircraft at the cruise condition.

A second challenge with BLI is that part of the benefit can be offset by decreased engine performance, particularly that of the bypass fan stage, which may be adversly affected by the presence of inlet distortion. The spatial non-uniformity in flow conditions across the height of the boundary layer presents non-uniform and unsteady conditions to the fan as it rotates through the boundary layer, so that part of the fan is always operating at "off-design" conditions with reduced efficiency.

The objective of this thesis is to address these two challenges at the conceptual design level. We propose a methodology for characterizing the propulsion system requirements in terms of flow mechanical energy, eliminating the difficulties of momentum-based accounting, and providing a procedure for engine sizing based on the performance of an isolated airframe. We also examine the sensitivity of blade row performance with inlet distortion to changes in various propulsor design parameters, to determine attributes of fan stage design and installation that mitigate the adverse effect of BLI on engine performance. The analyses in this thesis can thus serve as a reference early in the design process of fan stages for new BLI applications.

1.1 Approach

The propulsion system requirements are determined using the power balance method of Drela [2]. Rather than considering the forces on the aircraft, the performance of the airframe and engine are characterized in terms of sources and sinks of mechanical energy. Energy related quantities analagous to thrust, drag, and propulsive efficiency are defined, and it is shown that the BLI benefit can be explained as the combined effect of a decrease in effective airframe drag and an increase in propulsive efficiency; for the cases considered here, the latter is the dominant effect. The impact of propulsion system sizing and fan efficiency on BLI aircraft fuel burn are assessed using the TASOPT aircraft configuration optimization tool [3].

Viewing the system performance in terms of mechanical energy also provides insight into appropriate propulsion system scaling for powered wind tunnel models and for comparison between integrated and conventional podded propulsion system configurations. In this context, complementary experiments have been carried out using powered wind tunnel models with propulsor simulators sized according to the scaling rules presented in this thesis [4].

The impact of BLI inlet distortion on fan stage turbomachinery performance is assessed using two internal flow analyses. First, a linearized description is introduced and applied to quasi-two-dimensional (x, θ) flow simulating a fan stage to assess the sensitivity of blade row performance to changes in the turbomachinery design and installation. Second, a three-dimensional non-axisymmetric throughflow analysis is developed and applied to different fan stage geometries to assess the effectiveness of strategies for distortion tolerance arising from the two-dimensional description.

For both the external and internal flow analysis, we consider only the performance at the cruise design point. The majority of aircraft fuel burn occurs at cruise, and the viability of BLI should be confirmed at the propulsor design point before considering any off-design analysis. We limit ourselves to incompressible flow. Neglecting the effect of compressibility in the subsonic external flow may change numerical results by a few percent, but trends with the design variables should not be affected [3]. Similarly for internal flow, the relevant flow mechanisms that drive fan stage performance with inlet distortion have been shown to be insensitive to Mach number [5].

1.2 Contributions

1. BLI fuel burn benefit is shown to be enabled by increased propulsive efficiency for a given fan size. The power requirements of BLI configurations are quantified in terms of (i) the performance of the airframe to be propelled and (ii) the sizing of the propulsor, using the power balance method. Optimization of BLI and non-BLI configurations shows minimum fuel burn occurs in both configurations at approximately equal engine mass flow, with a reduction in required propulsive power in the BLI configuration due

to a reduction in viscous dissipation in the propulsor jet and airframe wake. The former is by far the dominant feature of the configuration examined.

2. Scaling for powered wind tunnel models used to experimentally assess BLI benefit has been defined based on analysis of power savings with BLI. Experimental results show power savings consistent with mechanical energy analysis of the wind tunnel models, confirming the BLI benefit and validating the power balance analysis for highly integrated aircraft configurations.

3. The impact of changes in fan efficiency on BLI fuel burn benefit has been evaluated for a proposed BLI aircraft configuration. Changes in fan efficiency are shown to have a small effect on overall BLI fuel burn benefit (less than 1% increase in fuel burn per 1% decreases in fan efficiency). Futher, they do not impact the optimal propulsor sizing. The sizing analysis (external flow problem) and fan performance analysis (internal flow problem) can thus each be carried out independently.

4. An analysis for simulating fan performance with three-dimensional inlet distortions has been developed. The flow through the fan blading is modeled using steady distributed momentum and energy sources on an axisymmetric grid. The source distributions are determined as a function of specified blade geometry. The formulation allows approximate calculation of non-axisymmetric flow fields that capture the relevant flow redistribution and distortion transfer at a reduced computational cost compared to full-wheel unsteady calculations, and without any a priori flow or performance data.

5. Flow mechanisms that determine conditions at the blade rows in fan stages with BLI are identified. The analysis shows that three-dimensional upstream flow redistribution results in rotor inlet conditions not predicted by two-dimensional compressor distortion response analysis. The rotor distortion transfer, downstream flow behavior, and rotor-stator interactions, however, are captured well by a linearized two-dimensional analysis.

6. Fan stage turbomachinery design attributes that can potentially mitigate the impact of BLI inlet distortion on propulsor performance are identified. It is found that effective non-axisymmetric stator design can (i) reduce velocity distortions and thus mitigate losses in the rotor and (ii) reduce losses in the stator by tailoring the geometry to

accept the incoming distortion downstream of the rotor.

1.3 Thesis Outline

Background on BLI and turbomachinery distortion response, including a review of the relevant literature, is provided in Chapter 2. Chapter 3 presents an analysis of BLI benefit and propulsor sizing, including the impact of reduced fan efficiency due to inlet distortion. Chapter 4 contains a linearized actuator disk distortion response analysis for two-dimensional fan stage blade-to-blade flows, which is used to identify design attributes that have the potent to mitigate the impact of inlet distortion on propulsor performance. Chapter 5 contains a description of an approximate analysis for turbomachines, which is used in Chapter 6 to assess the impact of various changes in fan stage design on performance with BLI inlet distortion. Conclusions and recommendations for future work are given in Chapter 7.

Chapter 2

Background

This chapter provides an overview of previous work related to aircraft propulsion with BLI. The chapter is divided into two broad categories, BLI aircraft performance and turbomachinery distortion response. A survey of the relevant literature is given on these topics, including a description of the power balance methodology used in Chapter 3, an overview of compressor distortion response modeling methodologies, and results from recent work on fan stages with BLI-type inlet distortions.

2.1 BLI Aircraft Performance

The concept of boundary layer ingestion as a way to reduce required propulsive power has been understood for some time. In marine applications, the location of a ship's propeller close to the trailing edge of the hull makes BLI inevitable. For design, the effect of BLI has typically been considered as an increase in propulsive efficiency for a required thrust [6] [7]. Betz [8] accounts for BLI benefit in this way, but provides a conceptual description of the benefit of re-energizing part of the wake of a body.

Smith [9] presents BLI as a means of increasing the efficiency of aircraft propulsors. The BLI benefit is quantified in terms of propulsive efficiency, defined as the product of free stream velocity and the drag of the propelled body (i.e., the drag power of the body) divided by the power added to the flow by the propulsor. This definition captures the beneficial effect of BLI, since the power added decreases with BLI, but it neglects that the force on the body will change due to the pressure field of an integrated propulsor.* Smith

---

*As a result of this definition, propulsive efficiencies greater than unity can be attained. Smith acknowlalso defines a power-saving coefficient, used to compare the performance of BLI and non-BLI configurations. The analysis presented in Chapter 3 proceeds in a manner similar to Smith, but uses a framework based on mechanical energy analysis.

2.1.1 Commerical Aircraft Concepts

In recent years, commercial aircraft concepts using BLI have been proposed. The work of the Cambridge-MIT Silent Aircraft Initiative (SAI) resulted in a hybrid wing-body aircraft concept optimized for low noise [10] [11]. The design included an embedded propulsion system to reduce noise and increase propulsive efficiency by ingesting a portion of the fuselage boundary layer [12] [13]. Similar designs have been analyzed by NASA for their potential for reduced environmental impact [14]. Most notably, one of these designs [15] has been selected as the platform for the detailed design of a propulsor to be used in a high speed fan rig test to assess fan stage performance with BLI inlet distortion.

The configuration of interest in this thesis is the MIT D8, which was developed as part of a NASA funded program to identify aircraft concepts and technologies for reduced environmental impact [16]. A schematic of the design is shown in Figure 2-1. Key design features include reduced cruise Mach number which allows reduction in wing sweep, weight, and drag, a "double-bubble" fuselage design which provides extra carry-over lift, and an empenage configuration featuring two vertical tails and flush-mounted engines that ingest a portion of the fuselage boundary layer. The reduced Mach number and fuselage-engine integration with short inlets leads to BLI inlet distortions with little or no streamwise vorticity, unlike previous designs with long S-duct inlets upstream of the fan [17]. In Chapters 5 and 6 we therefore consider the effects on the fan stage of vertically stratified stagnation pressure distributions far upstream.

2.1.2 Aircraft Performance Analysis with the Power Balance Method

In Chapter 3, the propulsion system requirements with BLI are determined using the Power Balance Method developed by Drela [2]. Because the propulsor pressure field will alter the surface forces on the airframe, and the ingestion of the airframe boundary layer changes the inlet conditions of the propulsor, airframe drag and engine thrust are not easily defined for

---

edges this fact, and his definitions for thrust and drag - while not representing specific forces that could be measured in a body-propulsor configuration - provide a consistent framework for evaluating BLI benefit.

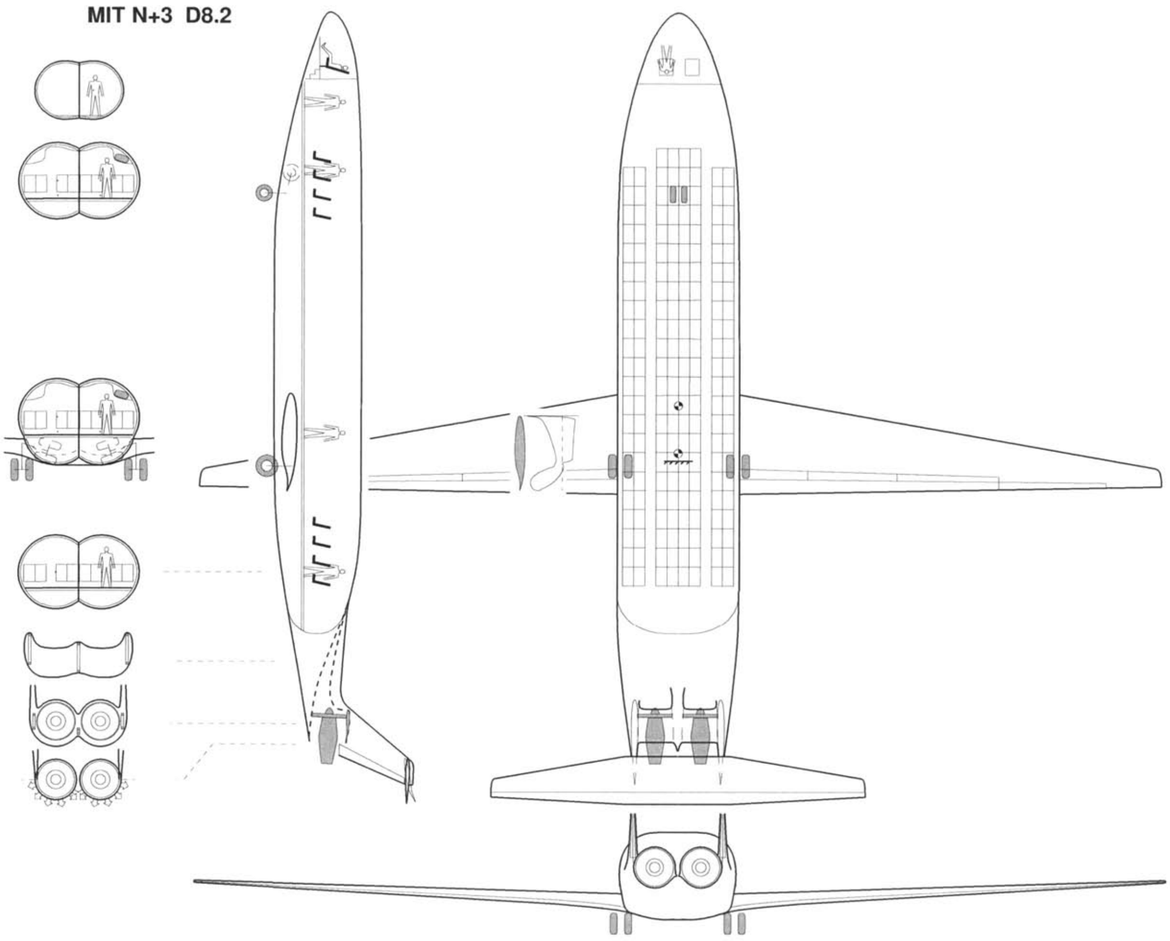

Figure 2-1: The MIT D8 aircraft configuration: a 180 passenger civil aircraft concept for reduced environmental impact.

BLI configurations. It is more useful, therefore, to work in terms of *power* than in terms of *forces*, and the power balance method considers the mechanical flow power quantities. For level unaccelerated flight, the power added to the propulsor mass flow must balance the viscous dissipation or lost power in the flow around the aircraft,

$$P_{K} = \Phi_{\mathrm{CV}}, \tag{2.1}$$

where P_K is the power added to the flow, defined as the rise in mechanical energy flux from the inlet to the exit of a propulsor,

$$P_{K} = \iint_{\mathrm{out-inl}} -\left[(p - p_\infty) + \frac{1}{2}\rho(V^2 - V_\infty^2)\right] \boldsymbol{V} \cdot \hat{n} d\mathcal{S}_{\mathrm{prop}}, \tag{2.2}$$

and Φ_{CV} is the viscous dissipation in the flow, integrated over a control volume extending far from the aircraft in all directions,

$$\Phi_{\text{CV}} = \iiint (\tau \cdot \nabla) \cdot \boldsymbol{V} d\mathcal{V}. \tag{2.3}$$

Typically, the volume integral in Equation (2.3) is not calculated directly. The dissipation is confined to viscous boundary layers, wakes, and the trailing vortex system downstream of an aircraft. These dissipation sources are illustrated schematically in Figure 2-2. For non-BLI configurations (denoted by primed $()'$ quantities), the dissipation sources of the isolated airframe can be characterized in terms of conventional drag metrics and the state of the boundary layer at various locations. The vortex dissipation, Φ'_{vortex}, is defined as the excess mechanical energy in the vortex system downstream of the aircraft, which is equal to the induced drag power,

$$\Phi'_{\text{vortex}} = V_\infty D'_i.$$

The surface dissipation, Φ'_{surf}, is the power lost in the boundary layer on solid surfaces, and is equal to the boundary layer kinetic energy defect at the trailing edge of the airframe, which is related to the boundary layer kinetic energy area Θ^*,

$$\Phi'_{\text{surf}} = \frac{1}{2}(\rho u_e^3 \Theta^*)_{\text{TE}} = \frac{1}{2} \iint (u_e^2 - u^2)\rho u \, d\mathcal{S}_{\text{TE}}. \tag{2.4}$$

The wake dissipation, Φ'_{wake}, is the excess mechanical energy of the wake in the reference frame of a stationary observer, and is related to the wake kinetic energy excess area Δ_K at the trailing edge of the airframe,

$$\Phi'_{\text{wake}} = \frac{1}{2}(\rho u_e^3 \Delta_K)_{\text{TE}} = \frac{1}{2} \iint (u_e - u)^2 \rho u \, d\mathcal{S}_{\text{TE}}. \tag{2.5}$$

The sum of the surface and wake dissipation is equal to the profile drag power, $V_\infty D'_p$, which is characterized by the momentum defect in the wake,

$$V_\infty D'_p = \Phi'_{\text{surf}} + \Phi'_{\text{wake}} = (\rho u_e^3 \Theta)_{\text{wake}} = u_e \iint (u_e - u)\rho u \, d\mathcal{S}_{\text{wake}}, \tag{2.6}$$

where the boundary layer momentum area Θ is evaluated at a location far downstream at

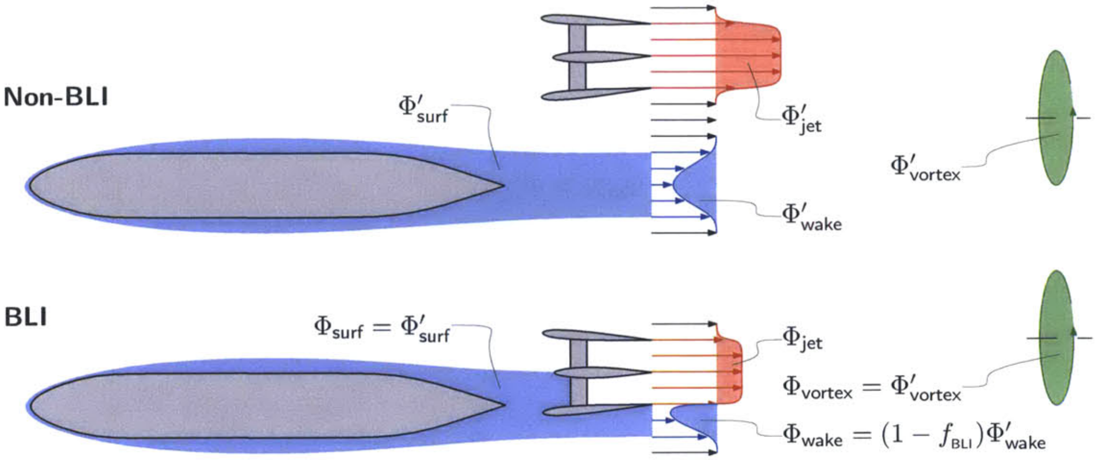

Figure 2-2: Sources of dissipation, Φ, can be estimated based on conventional drag and boundary layer quantities, and are insensitive to perturbation pressure field effects for integrated configurations.

free stream static pressure. The relative contributions of surface and wake dissipation to total profile drag depend on the state of the boundary layer at the trailing edge of the body. Combining Equations (2.4) and (2.6) yields the surface dissipation contribution in terms of the boundary layer kinetic energy shape factor $H^* = \Theta^*/\Theta$,

$$\Phi'_{\text{surf}} = V_\infty D' \frac{H^*_{\text{TE}}}{2}. \tag{2.7}$$

For attached turbulent flow, $H^* \simeq 1.75$ [2], and the surface and wake dissipation account for approximately 7/8 and 1/8 of the drag power, respectively.

The jet dissipation, Φ_{jet}, is the excess mechanical energy of the propulsor jet,

$$\Phi_{\text{jet}} = \frac{1}{2} \iint (V_\infty - V_{\text{jet}})^2 \rho V_{\text{jet}} \, d\mathcal{S}_{\text{out}}. \tag{2.8}$$

In Chapter 3, we show that the jet dissipation will depend on the propulsive power requirement of the configuration, the amount of boundary layer ingested, and the selection of the propulsor mass flow. 2-2.

With BLI, the dissipation is altered because of the re-energizing of the ingested wake, as in Figure 2-2. As suggested by Drela [2][3], and shown computationally for a range of body-propulsor configurations by Sato [18], a quantitatively useful approximation is that the vortex and surface dissipation are unaffected by the presence of the propulsor,[†]

$$\Phi_{\text{vortex}} = \Phi'_{\text{vortex}}, \tag{2.9}$$

$$\Phi_{\text{surf}} = \Phi'_{\text{surf}}. \tag{2.10}$$

The wake dissipation, however, is reduced by an amount equal to the downstream dissipation would occur in the fraction f_{BLI} of the boundary layer flow ingested by the propulsor,

$$\Phi_{\text{wake}} = (1 - f_{\text{BLI}})\Phi'_{\text{wake}}. \tag{2.11}$$

In Chapter 3, an analysis of Equations (2.1)-(2.11) is carried out to show the physical mechanisms of BLI benefit. Using this framework, it is easy to show that BLI reduces the required flow power P_K due to reduced wake dissipation (see Equation (2.11)) and jet dissipation, depending on the sizing of the propulsor.

2.2 Turbomachinery Distortion Response

The response of fans to steady inlet distortion has also received attention. Earlier work on compression system modelling identified distortion-component coupling effects in the case of two-dimensional circumferential distortions, with the main concern being the impact of distortion on stall margin. Although the application and objectives are different, many of the basic principles are applicable to our study of design point BLI fan efficiency. More recent analyses have been used for fan stage distortion response analysis. These methods, along with results from higher-fidelity assessments of fan stages with BLI-type inlet distortions, form a basis for the fan stage distortion analysis in this thesis.

2.2.1 Previous Modeling Approaches

Longley and Greitzer [19] provide an excellent review of considerations for propulsion system inlet distortion response, and we present two important concepts here. First, we consider *parallel compressor theory*, in which a non-uniform flow through a compressor is treated as two separate one-dimensional flows. The streams operate on different points on the com-

---

[†] This is not true for the force on the body, which can be altered due to the perturbation pressure field of a downstream propulsor.

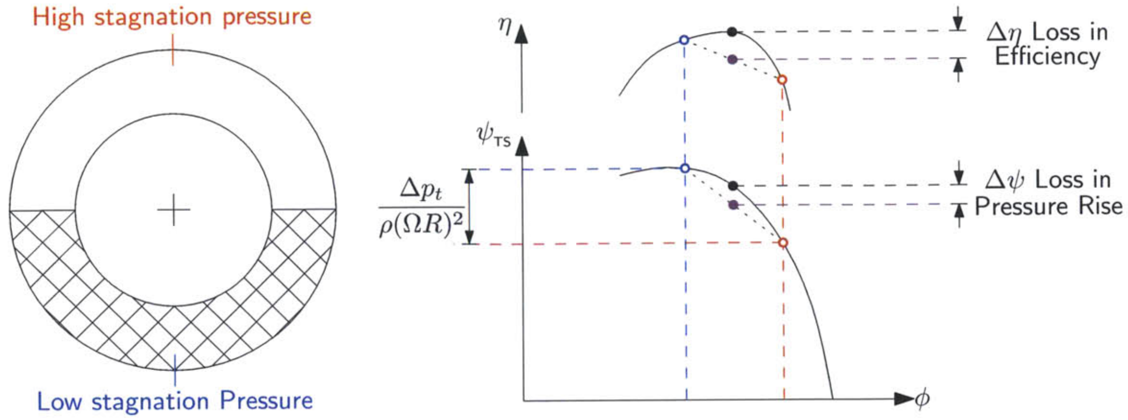

Figure 2-3: Parallel compressor model for circumferential distortion response (adapted from Longley and Greitzer [19]); average performance with inlet distortion is estimated assuming parallel streams operating on uniform flow characteristics.

pressor total-to-static pressure rise characteristic as shown in Figure 2-3. If the compressor exit static pressure is assumed constant, the magnitude of the upstream stagnation pressure distortion constrains the total-to-static pressure rise of each stream and thus the difference in flow coefficient and resulting axial velocity distortion. If both the pressure rise characteristic and efficiency characteristic are concave-down (with respect to flow coefficient), the average pressure rise and efficiency are reduced relative to the uniform flow performance.

The parallel compressor model highlights the importance of the slope of the pressure rise characteristic in determining the distortion response. A steeper (more negative) $\psi_{TS}(\phi)$ slope results in lower axial velocity distortion at the compressor, which may also decrease the efficiency reduction, depending on changes in changes in the efficiency characteristic. This suggests one means of improving performance of BLI fan performance, which we assess in Chapters 4 and 6.

A second important concept is the upstream flow redistribution due to interaction between the distortion and the compressor (or fan). For a two-dimensional flow (representative of high hub-to-tip ratio compressor geometries), the attenuation of axial velocity distortion predicted by parallel compressor theory results in the generation of non-axisymmetric circumferential velocities (swirl) at the compressor as illustrated in Figure 2-4. The non-uniformities in axial and circumferential velocity result in flow angle variations at the blade row inlet, creating an off-design incidence range the blades must tolerate. The affect of combined axial and circumferential velocity distortions on compressor performance have been

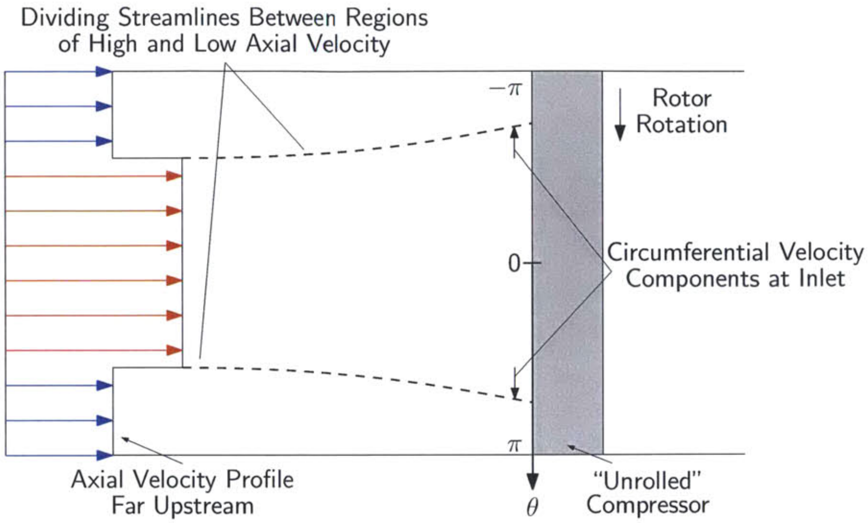

Figure 2-4: Axial velocity distortion attenuation leads to circumferential flow redistribution and inlet flow angle variation at compressor location (adapted from Longley and Greitzer [19]).

assessed using two-dimensional analyses [20]. In Chapter 4, we present such an analysis, based on the work of Greitzer and Griswold [21], with new models for discrete rotor and stator actuator disks and non-axisymmetric stator and flowpath geometries.

In Chapter 5, we develop a non-axisymmetric turbomachinery throughflow analysis for fan stage flows with inlet distortion at a computational cost much lower than those described above. The basic idea is to replace the turbomachinery blade rows with distributions of momentum and energy source terms in the calculation that generate a similar flow field to the actual flow [22] [23]. Similar methods have been used in turbomachinery research at the MIT Gas Turbine Lab to address multistage compressor stability [24], BLI propulsor aerodynamic [25] and acoustic [26] performance, and the design of ultra-short nacelles for low pressure ratio fans [27]. In these previous formulations, the form of the source term distributions is determined by extracting blade forces from single passages RANS calculations carried out over a range of operating conditions and developing a correlation to local flow conditions. In the current implementation, described in Chapter 5, the source terms are determined based on a blade passage description characterized by a specified blade camber surface geometry, eliminating the need for a priori calculations.

2.2.2 BLI Fan Distortion Response

Initial designs of BLI propulsion systems [28] and fan stages [29] did not account for fan efficiency did not asses the impact of BLI inlet distortion on fan efficiency. More recent computational and experimental research carried out on a low speed model of the NASA rotor 67 fan stage has led to useful information on fan response to circumferential inlet distortion [30][31]. A high speed fan stage is also being designed for rig testing with BLI inlet distortion [32], and computations show the fan efficiency decreases by less than 2% relative to uniform inlet conditions.

The recent work of Gunn and Hall [5] provides the most comprehensive treatment of the response of a contemporary fan stage to BLI inlet distortion, and the results of this study are used as a benchmark for assessing the effectiveness of the model presented in Chapter 5. The flow features of BLI fan stage distortion response are identified using unsteady full-wheel CFD in conjection with experiments on a low speed fan rig. The upstream redistribution is found to have significant radial components, creating co- and counter-swirl distortions at the fan face along the entire blade span. The distortions result in non-uniform work input affecting the flow into the stator. Fan efficiency was found to decrease by only 1-2% relative to the performance with uniform inlet conditions, with the increased losses concentrated in areas where the local diffusion factor is increased. Computations on a high-speed fan show that while the details of the flow may change, specifically the presence of shocks, the flow features that drive the change in efficiency with distortion are not qualitatively altered by the change in Mach number.

Chapter 3

BLI Configuration Performance Analysis

First steps in designing a podded (on wing or fuselage) aircraft propulsor include estimating the engine thrust requirements and selecting the physical size of the propulsor. For an aircraft with boundary layer ingestion (BLI), however, the definitions of engine thrust and airframe drag become ambiguous, as described in Chapter 1, and it is more useful to work in terms of *power* than in terms of *forces*. We thus define the propulsor requirements using the power balance methodology described in Chapter 2, which allows quantification of the BLI benefit based on sources and sinks of mechanical power in the propulsor and aircraft flow fields.

A further complication in the assessment and design of BLI propulsors is the effect of inlet distortion from the ingested boundary layer on propulsor performance. In this chapter, the impact of inlet distortion is considered on a one-dimensional basis, by examining the sensitivity of configuration performance to changes in fan efficiency. Mechanisms leading to increased propulsor losses due to distortion and strategies for distortion tolerant propulsor design are the focus of Chapters 4 through 6.

3.1 Mechanical Energy Analysis

We first examine the impact of BLI for a simple body-propulsor configuration with no vortex dissipation as in Figure 3-1. We proceed in a manner aligned with that of Smith [9], characterizing the BLI benefit in terms of propulsive efficiency and power savings, although

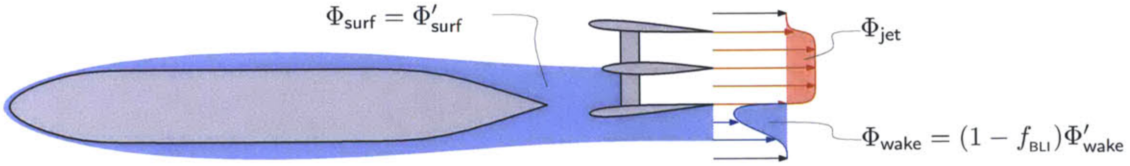

Figure 3-1: BLI body-propulsor configuration with dissipation sources used in lumped parameter mechanical energy analysis.

we make two changes in the analysis. One is that the propulsive power requirement is determined using the power balance method [2]. This results in a definition for propulsive efficiency, based on mechanical power added to the flow by the propulsor and viscous dissipation in the external flow, which is different from that of Smith. Second, we cast the analysis in terms of propulsor mass flow as an independent variable upon which the BLI power savings depends.

3.1.1 Propulsive Power Requirement

We adopt a lumped parameter approach, where the airframe performance is characterized in terms of the dissipation quantities defined in Section 2.1.2, and the propulsor performance is characterized by a mass flow, $\dot{m}$, and jet velocity, V_{jet}. Table 3.1 lists the definitions of the various power and dissipation terms considered throughout this section.

The *mechanical flow power* added to the flow by the propulsor, P_K, is equal to the increase in mechanical energy of the flow from propulsor inlet to exit,

$$P_K = \frac{1}{2}\dot{m}(V_{\text{jet}}^2 - V_\infty^2) + f_{\text{BLI}}\Phi'_{\text{surf}}. \tag{3.1}$$

Equation (3.1) states that P_K is equal to the increase in propulsor flow kinetic energy from free stream conditions to the jet velocity, plus the inlet mechanical energy defect, which is equal to the dissipation within the flow upstream of the propulsor, $f_{\text{BLI}}\Phi_{\text{surf}}$. The propulsor jet introduces excess kinetic energy at the propulsor outlet, which is equal to the total dissipation, Φ_{jet}, that will occur downstream of that location,

$$\Phi_{\text{jet}} = \frac{1}{2}\dot{m}(V_{\text{jet}} - V_\infty)^2. \tag{3.2}$$

Mechanical flow power	P_K	Equations (2.2) and (3.1)
Jet dissipation	Φ_{jet}	Equations (2.8) and (3.2)
Net propulsive power	$P_K - \Phi_{\text{jet}}$	$= P_K \eta_p$
Shaft power	P_{shaft}	$= P_K / \eta_f$
Vortex dissipation	Φ_{vortex}	$= V_\infty D'_i$
Surface dissipation	Φ_{surf}	$= \frac{1}{2}(\rho u_e^3 \Theta^*)_{\text{TE}}$
Wake dissipation	Φ'_{wake}	$= \frac{1}{2}(\rho u_e^3 \Delta_K)_{\text{TE}}$
	Φ_{wake}	$= (1 - f_{\text{BLI}})\Phi'_{\text{wake}}$
Profile drag power	$V_\infty D'_p$	$= \Phi'_{\text{surf}} + \Phi'_{\text{wake}}$
Drag power	$V_\infty D'$	$= \Phi'_{\text{surf}} + \Phi'_{\text{wake}} + \Phi'_{\text{vortex}}$

Table 3.1: Definition of power and dissipation terms used in lumped parameter mechanical energy analysis.

For zero net force on the configuration (no acceleration), the power added to the flow is equal to the total dissipation,

$$P_K - \Phi_{\text{jet}} = \Phi_{\text{surf}} + \Phi_{\text{wake}}. \tag{3.3}$$

Equations (3.1)-(3.3) can be combined using the definitions in Table 3.1 to express a power balance in terms of body drag and dissipation performance, fractional amount of BLI, propulsor mass flow, and jet velocity,

$$\dot{m} V_\infty (V_{\text{jet}} - V_\infty) + f_{\text{BLI}} \Phi'_{\text{surf}} = V_\infty D' - f_{\text{BLI}} \Phi'_{\text{wake}}. \tag{3.4}$$

Equation (3.4) shows the beneficial effects of BLI. The right-hand side is the total dissipation (lost mechanical power) associated with the body boundary layer and wake. The left-hand side of Equation (3.4) is here defined as the *net propulsive power*, equal to the flow power P_K minus the lost power in the jet downstream Φ_{jet}. For the former, with BLI, the lost power is reduced by an amount proportional to the boundary layer ingestion fraction. For the latter, ingestion of boundary layer fluid increases the net propulsive power for a given jet velocity and mass flow. For a non-BLI propulsor, $f_{\text{BLI}} = 0$, and Equation (3.4) reduces to the conventional force balance between thrust and drag.

For a conceptual description of the impact of BLI on configuration performance, it is useful to recast the power balance equation in terms of conventional thrust and drag metrics. To do this, equation (3.4) can be rearranged as an expression for the drag of the isolated body,

$$\dot{m}\left[V_{\text{jet}} - V_\infty\left(1 - \frac{f_{\text{BLI}}D'}{\dot{m}V_\infty}\right)\right] = D'. \tag{3.5}$$

With no BLI, the left-hand side of Equation (3.5) is equal to the net thrust, the difference between gross thrust, $\dot{m}V_{\text{jet}}$, and "ram drag," $\dot{m}V_\infty$. Boundary layer ingestion produces a reduction of airframe wake dissipation, and a decrease in propulsor inlet mechanical energy flux, which appears as an effective ram drag reduction.*

To quantify the BLI benefit, we consider the behavior of the mechanical flow power, P_K. Propulsor shaft power is related to P_K through the fan efficiency, so that P_K is the relevant power consumption metric for aerodynamic performance analysis in the absence of information about propulsor internal performance. For the case of the body-propulsor configuration with no vortex dissipation shown in Figure 3-1, Equations (3.1) and (3.4) can be combined to determine the flow power P_K as a function of propulsor mass flow $\dot{m}$ and BLI fraction f_{BLI} for assumed surface and wake dissipation contributions to isolated body drag power. This behavior is shown in Figure 3-2. The vertical axis is the flow power, P_K non-dimensionalized by the isolated body drag power, $V_\infty D'$, and the horizontal axis is the propulsor mass flow free stream momentum flux, $\dot{m}V_\infty$, non-dimensionalized by the drag, D'. Increasing the propulsor mass flow for a given D' results in a reduction in jet velocity and jet dissipation, and thus a reduction in P_K. Increasing f_{BLI} yields a reduction in P_K because the wake and jet dissipation are reduced. In the limit of $f_{\text{BLI}} = 1$, the propulsor ingests the entire wake and accelerates it to $V_{\text{jet}} = V_\infty$, eliminating the wake and jet dissipation. The flow power is equal to the surface dissipation, $P_K = \Phi_{\text{surf}}$. In this ideal case, the flow power is the smallest possible, and is independent of propulsor size (as long as the entire wake is ingested).

3.1.2 Propulsive Efficiency

We now relate the reduction in required power with BLI to the change in propulsive efficiency. Following Drela [2] and Sato [18], we define propulsive efficiency as the ratio of propulsive power delivered to the aircraft, or net propulsive power, $(P_K - \Phi_{\text{jet}})$, to mechan-

---

*It is worth noting that the effective ram drag reduction described in Equation (3.5) is not necessarily equal to the ingested momentum defect. The change in flow power requirement depends on the ingested *kinetic energy* defect, which is expressed here in terms of more familiar momentum quantities.

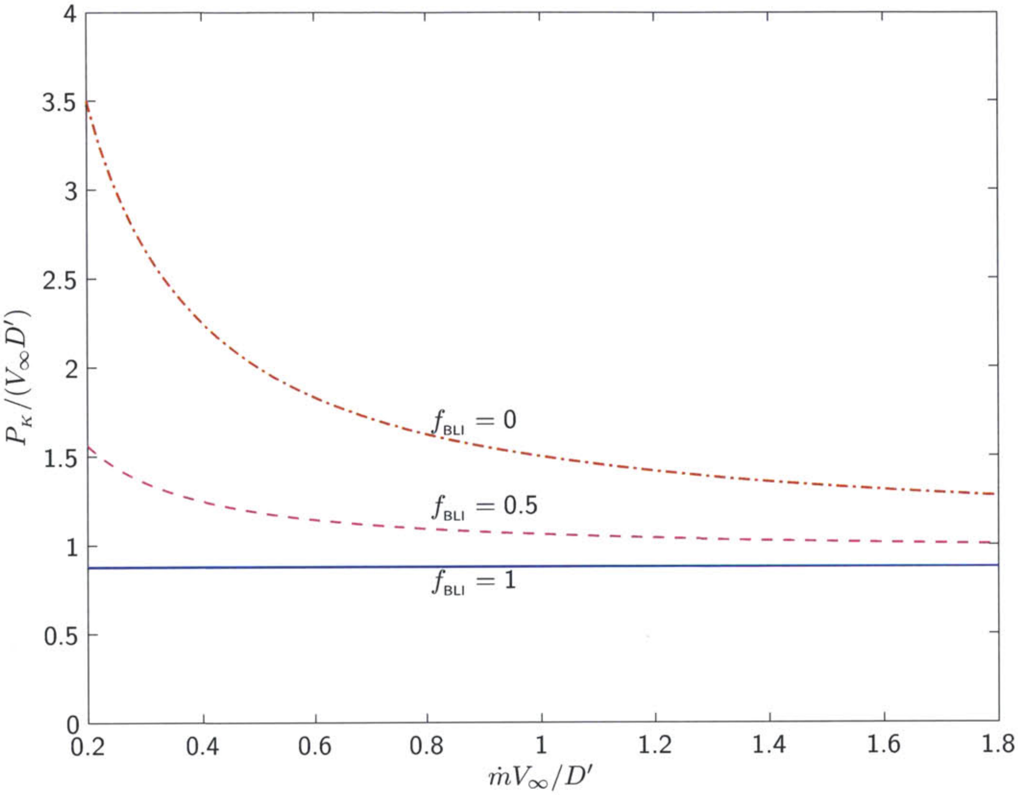

Figure 3-2: Non-dimensional propulsor flow power $P_K/(V_\infty D')$ versus non-dimensional propulsor mass flow $\dot{m}V_\infty/D'$ for different values of BLI fraction f_{BLI}; increasing BLI fraction at fixed propulsor mass flow decreases mechanical flow power.

ical power added to the propulsor mass flow, P_K,

$$\eta_p = \frac{P_K - \Phi_{\text{jet}}}{P_K}. \tag{3.6}$$

Equation (3.6) shows the propulsive efficiency as a measure of the jet dissipation for a given mechanical power delivered to the propulsor mass flow. Combining Equations (3.1), (3.2), and (3.6) yields an expression for the dependence of η_p on f_{BLI},

$$\eta_p = 1 - \left[\frac{V_{\text{jet}} + V_\infty}{V_{\text{jet}} - V_\infty} + \frac{f_{\text{BLI}}\Phi'_{\text{surf}}}{\frac{1}{2}\dot{m}(V_{\text{jet}} - V_\infty)^2}\right]^{-1}. \tag{3.7}$$

For a non-BLI propulsor, Equation (3.7) reduces to the Froude efficiency,

$$\eta'_p = \frac{2V_\infty}{V'_{\text{jet}} + V_\infty}. \tag{3.8}$$

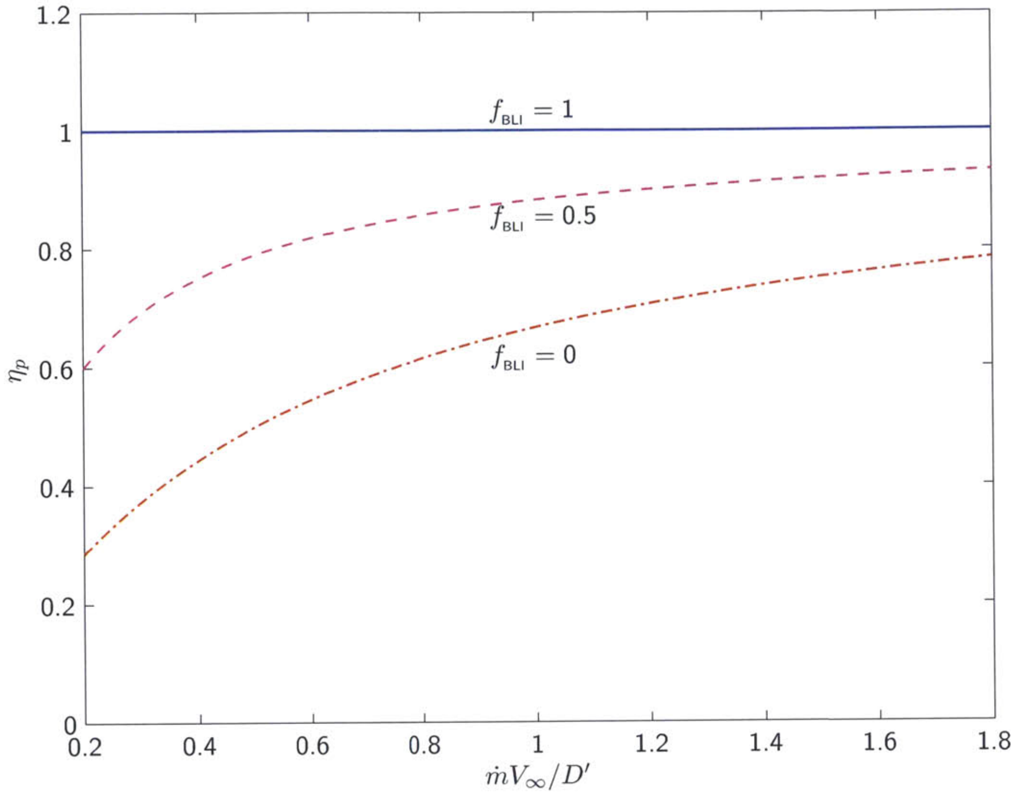

Figure 3-3: Propulsive efficiency η_p versus non-dimensional propulsor mass flow $\dot{m}V_\infty/D'$ for different values of BLI fraction f_{BLI}; increasing BLI fraction at fixed propulsor mass flow increases propulsive efficiency, approaching unity as the entire wake is ingested.

Equation (3.7) shows that increasing the BLI fraction for given $\dot{m}V_\infty/D'$ and V_{jet}/V_∞ increases the propulsive efficiency. BLI also results in a reduction in the required net propulsive power, the numerator of Equation (3.6).

Increases in propulsive efficiency can also be achieved by increasing the non-dimensional propulsor mass flow to reduce jet dissipation, as shown in Figure 3-3. The vertical axis is the propulsive efficiency, and the horizontal axis is the propulsor mass flow, non-dimensionalized as in Figure 3-2. For any amount of BLI, increasing the non-dimensional propulsor mass flow decreases V_{jet}/V_∞, reducing jet dissipation and increasing propulsive efficiency. Alternatively, increasing the BLI fraction at a given non-dimensional mass flow reduces the propulsor inlet mechanical energy flux, and thus decreases jet dissipation for a given P_K.

3.1.3 Power Saving Coefficient

With BLI, there is a reduction in wake and jet dissipation, the latter associated with an increase in propulsive efficiency, both of which contribute to decreased propulsor flow power, P_K. The power saving coefficient of Smith [9] can be defined as the normalized decrease in required power with BLI compared to a non-BLI propulsor,

$$\mathrm{PSC} = \frac{P'_K - P_K}{P'_K}. \tag{3.9}$$

Using the power balance equation yields an expression for PSC in terms of propulsive efficiency with and without BLI and the normalized dissipation of the isolated body,

$$\mathrm{PSC} = 1 - \frac{\eta'_p}{\eta_p}\left(1 - \frac{f_{\mathrm{BLI}}\Phi'_{\mathrm{wake}}}{V_\infty D'}\right). \tag{3.10}$$

Equation (3.10) shows the two physical mechanisms of BLI benefit. First, the wake dissipation and required net propulsive power are decreased by an amount equal to the wake dissipation of the ingested boundary layer, $f_{\mathrm{BLI}}\Phi'_{\mathrm{wake}}$. Second, the propulsive power can be developed at a higher propulsive efficiency with BLI, due to the reduction in propulsor inlet mechanical energy flux.

The relative importance of the two effects is illustrated in Figure 3-4. The vertical axis is the required power P_K non-dimensionalized as in Figure 3-2, and the horizontal axis is the propulsive efficiency. The wake dissipation reduction benefit is the vertical distance between curves for different values of f_{BLI}. Comparison of Figure 3-2, 3-3, and 3-4 shows the power saving at fixed propulsive efficiency (i.e. wake dissipation reduction) is small compared to the benefit due to increased propulsive efficiency at a given propulsor mass flow.

3.2 BLI Aircraft Configuration Performance

In this section, the BLI benefit analysis of Section 3.1 is applied to the D8 aircraft configuration. The ratio of ingested wake dissipation $f_{\mathrm{BLI}}\Phi'_{\mathrm{wake}}$ to total airframe drag power $V_\infty D'$ is small ($\sim 1\%$) due to the presence of vortex dissipation (induced drag), and because only a portion of the fuselage boundary layer is ingested. The dominant mechanism of BLI power saving is therefore increased propulsive efficiency.

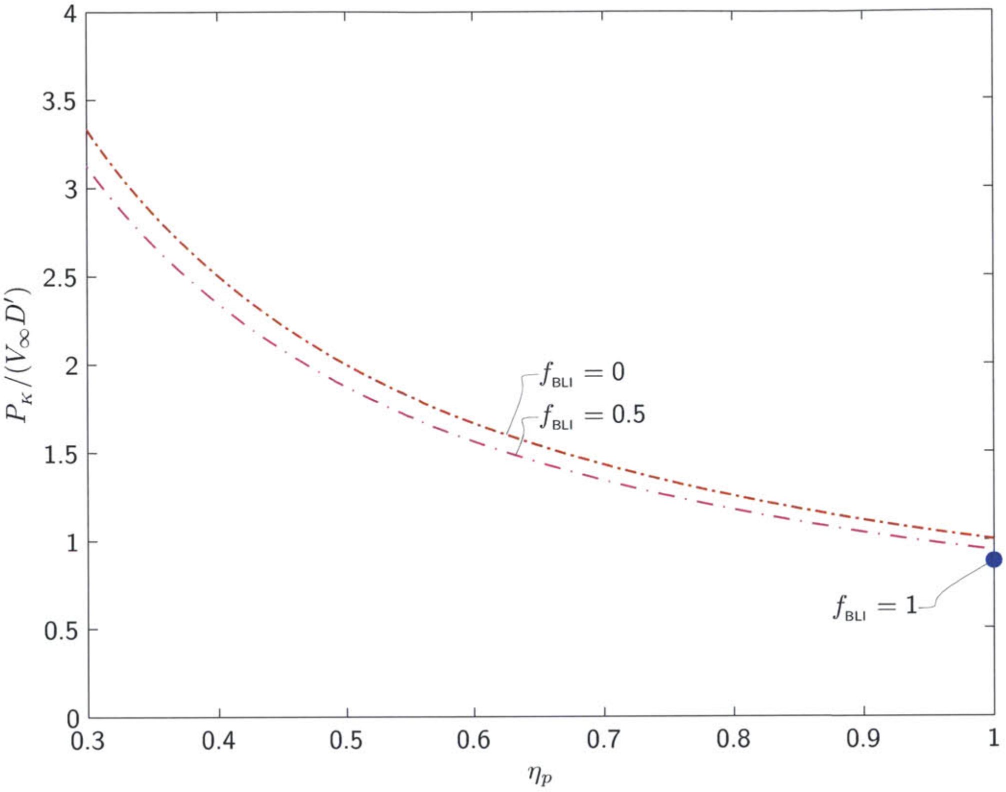

Figure 3-4: Non-dimensional propulsor input power $P_K/(V_\infty D')$ versus propulsive efficiency η_p for different values of BLI fraction f_{BLI}; increasing BLI fraction yields smaller flow power reduction at fixed propulsive efficiency than at fixed mass flow.

We examine not only the reduction in required flow power P_K with BLI, but also the impact on overall fuel burn. This is done using TASOPT configuration optimization tool, which calculates airframe and engine sizing for minimum fuel burn as a function of a range of input design parameters characterizing various configuration component technologies [3]. The optimization takes into account factors such as engine weight and nacelle drag, and thus captures the system-level impact of BLI on fuel burn, providing insight into relevant propulsor sizing for civil aircraft with BLI.

3.2.1 Propulsive Power Requirement

For an aircraft configuration with BLI, the airframe dissipation can be characterized in terms of conventional drag metrics, using the relations between momentum and drag quantities discussed above. We define a dissipation coefficient as

$$C_\Phi = \frac{\Phi}{\frac{1}{2}\rho V_\infty^3 S_{\text{ref}}}. \tag{3.11}$$

The airframe lift produces trailing vorticity that generates dissipation not considered in the previous section. This is directly related to the induced drag D_i,

$$C_{\Phi_{\text{vortex}}} = C'_{D_i}. \tag{3.12}$$

The viscous profile drag D_p can be decomposed into contributions from dissipation in the surface boundary layer and downstream wake as described in Chatper 2,

$$C'_{\Phi_{\text{surf}}} + C'_{\Phi_{\text{wake}}} = C'_{D_p}. \tag{3.13}$$

Combining Equations (3.12) and (3.13), the sum of the dissipation coefficients for an isolated can be related to the drag coefficient C'_D,

$$C'_{\Phi_{\text{vortex}}} + C'_{\Phi_{\text{surf}}} + C'_{\Phi_{\text{wake}}} = C'_{D_i} + C'_{D_p} = C'_D. \tag{3.14}$$

The required mechanical flow power P_K, can be estimated based on the isolated airframe performance and propulsive efficiency,

$$C_{P_K} = \frac{P_K}{\frac{1}{2}\rho V_\infty^3 S_{\text{ref}}} = \frac{1}{\eta_p}(C'_D - f_{\text{BLI}} C'_{\Phi_{\text{wake}}}). \tag{3.15}$$

The term in parentheses in Equation (3.15) is the total airframe dissipation, which is estimated based on the drag of the isolated airframe (without a propulsor), C'_D, and the dissipation of the ingested wake $f_{\text{BLI}} C'_{\Phi_{\text{wake}}}$. The impact of the downstream jet dissipation is included through the propulsive efficiency, η_p, which is increased by the reduction in propulsor inlet mechanical flux, $f_{\text{BLI}} \Phi'_{\text{surf}}$.

Figure 3-5 shows C_{P_K} for a range of D8 configurations having different design propulsive efficiency values. Each configuration has been optimized for minimum fuel burn at a specified design fan pressure ratio using TASOPT. For comparison, C_{P_K} calculated using Equation (3.15) and the D8.2 (optimized BLI configuration) airframe D' and $f_{\text{BLI}} \Phi'_{\text{wake}}$ values is also shown. Since the airframe is optimized in TASOPT, improvements in propulsive

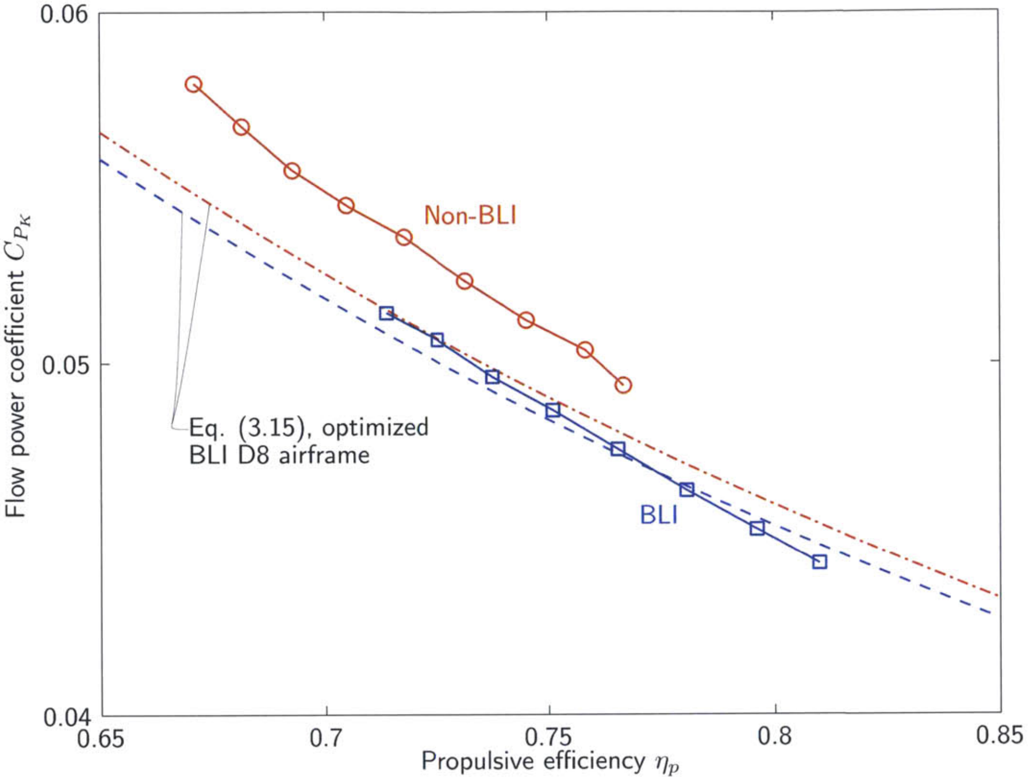

Figure 3-5: D8 flow power coefficient C_{P_K} versus propulsive efficiency η_p in BLI and non-BLI configurations; symbols show TASOPT-optimized configurations, and dashed curves are estimates based on the optimized BLI D8 airframe performance using the lumped parameter mechanical energy analysis.

efficiency result in reduction in fuel weight and airframe drag. For this reason the slope of C_{P_K} vs η_p is steeper for the TASOPT designs than for the curves based on fixed airframe performance. The effect of propulsion system efficiency is also evident in the difference between the BLI and non-BLI designs: not only does the non-BLI configuration have a higher wake dissipation, it also has increased overall airframe drag due to increased fuel weight.

3.2.2 Selection of Propulsive Efficiency

For a given thrust, propulsive efficiency increases with propulsor mass flow, but the latter can cost increased engine weight and external dissipation. The selection of propulsor mass flow and propulsive efficiency for minimum fuel burn thus requires an optimization to capture the tradeoffs between propulsive efficiency and engine size.

Figure 3-6a shows fuel burn as a function of propulsive efficiency for BLI and non-

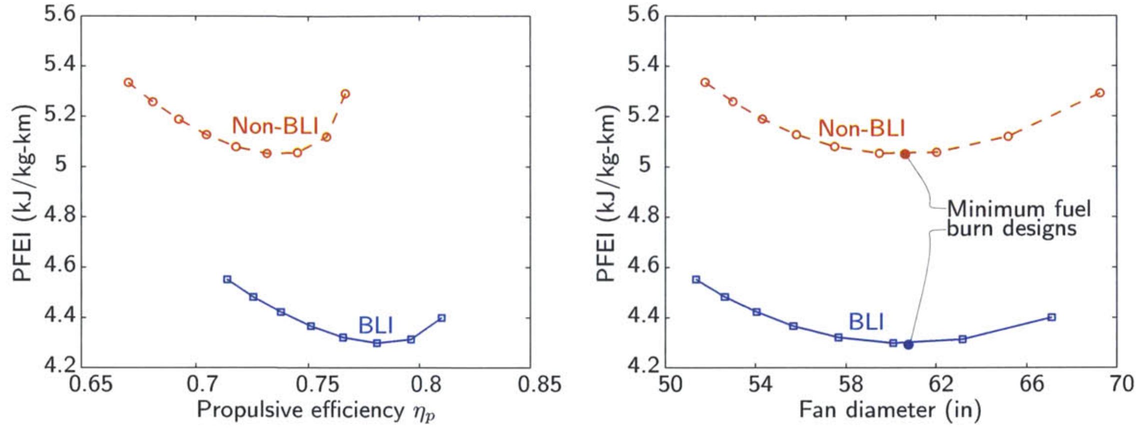

Figure 3-6: Payload Fuel Energy Intensity versus propulsive efficiency (left) and fan diameter (right) for TASOPT-optimized BLI and non-BLI D8 configurations; minimum fuel burn BLI design has higher propulsive efficiency than non-BLI design at approximately equal fan diameter.

BLI D8 configurations optimized with TASOPT. The vertical axis is Payload Fuel Energy Intensity (PFEI), defined as the fuel energy divided by the product of mission payload and range [33]. Unlike C_{P_K}, fuel burn does not decrease monotonically with increases in propulsive efficiency. The propulsive efficiency for minimum fuel burn is higher in the BLI configuration (78%) than in the non-BLI configuration (73%). To show the competing effects of increased propulsive efficiency and increased engine size, Figure 3-6b shows PFEI for the same configurations as a function of fan diameter. At the lower fan diameters, the fuel burn decreases occur becuase of increasing propulsive efficiency. At the higher fan diameters, the fuel burn increases occur because of increasing fan weight and external nacelle dissipation. The minimum fuel burn design for the D8 mission in both BLI and non-BLI configurations have approximately equal fan diameter (61 inches). Put another way, the BLI propulsive efficiency benefit occurs at approximately equal propulsor mass flows. In practice, therefore, the benefit of BLI is that it enables higher levels of propulsive efficiency without increases in propulsor size.

3.2.3 Scaling for Experimental Assessment of BLI Benefit

The power balance analysis provides a framework for the scaling and interpretation of measured performance for comparison of powered wind tunnel models. Experiments have been carried out on BLI and non-BLI configurations of a scale model D8 with propulsor simulators at low Mach numbers ($M \approx 0.1$) [34]. Measured quantities include the electrical power supplied to the propulsors (from which P_K can be estimated [35]) and the force on the model.

The purpose of the experiments is to measure the cruise BLI power saving between BLI and non-BLI D8 configurations. The selection of the nozzle area will determine the net force on the model for given propulsive power, and we impose the following constraints on the design propulsor operating point and nozzle area:

1. The flow power, P_K, is measured in each configuration at the condition of zero net streamwise force, X, on the model.
2. Nozzle areas are selected for specified η_p at the $X = 0$ condition *in each configuration.*

The first constraint represents a scaling of zero net streamwise force at cruise. The second aims to preserve the full-scale PSC by using representative propulsive efficiency values at model scale.

For an airframe with known aerodynamic performance, the configuration performance can be estimated using the lumped parameter analysis. The coefficient of net streamwise force on the model, C_X, can be estimated based on the difference between flow power and total aircraft dissipation (including jet dissipation). Combining Equations (3.1), (3.2), (3.11), (3.12), and (3.13), C_X can be expressed in terms of the airframe drag coefficient C'_D, ingested drag fraction $f_{\text{BLI}} C'_{D_p}$, non-dimensional jet velocity V_{jet}/V_∞, and normalized jet area $A_{\text{jet}}/\mathcal{S}_{\text{ref}}$,

$$C_X = \frac{\sum \Phi - P_K}{V_\infty} = C'_D - f_{\text{BLI}} C'_{D_p} - 2\frac{V_{\text{jet}}}{V_\infty}\left(\frac{V_{\text{jet}}}{V_\infty} - 1\right)\frac{A_{\text{jet}}}{\mathcal{S}_{\text{ref}}}. \tag{3.16}$$

Equation (3.7) can also be rearranged to express the propulsive efficiency η_p in terms of the ingested wake dissipation $f_{\text{BLI}} C'_{\Phi_{\text{wake}}}$ and the non-dimensional jet velocity and area, V_{jet}/V_∞ and $A_{\text{jet}}/\mathcal{S}_{\text{ref}}$,

$$\eta_p = 1 - \left[\frac{\frac{V_{\text{jet}}}{V_\infty} + 1}{\frac{V_{\text{jet}}}{V_\infty} - 1} + \frac{f_{\text{BLI}} C'_{\Phi_{\text{wake}}}}{\frac{V_{\text{jet}}}{V_\infty}\left(\frac{V_{\text{jet}}}{V_\infty} - 1\right)^2 \frac{A_{\text{jet}}}{\mathcal{S}_{\text{ref}}}}\right]^{-1}. \tag{3.17}$$

Equations (3.16) and (3.17) give two equations for V_{jet}/V_∞, $A_{\text{jet}}/\mathcal{S}_{\text{ref}}$, C_X, and η_p. The nozzle area can thus be selected to provide a specified propulsive efficiency, η_p at $C_X = 0$. Conversely, for given unpowered airframe performance, the performance of the powered

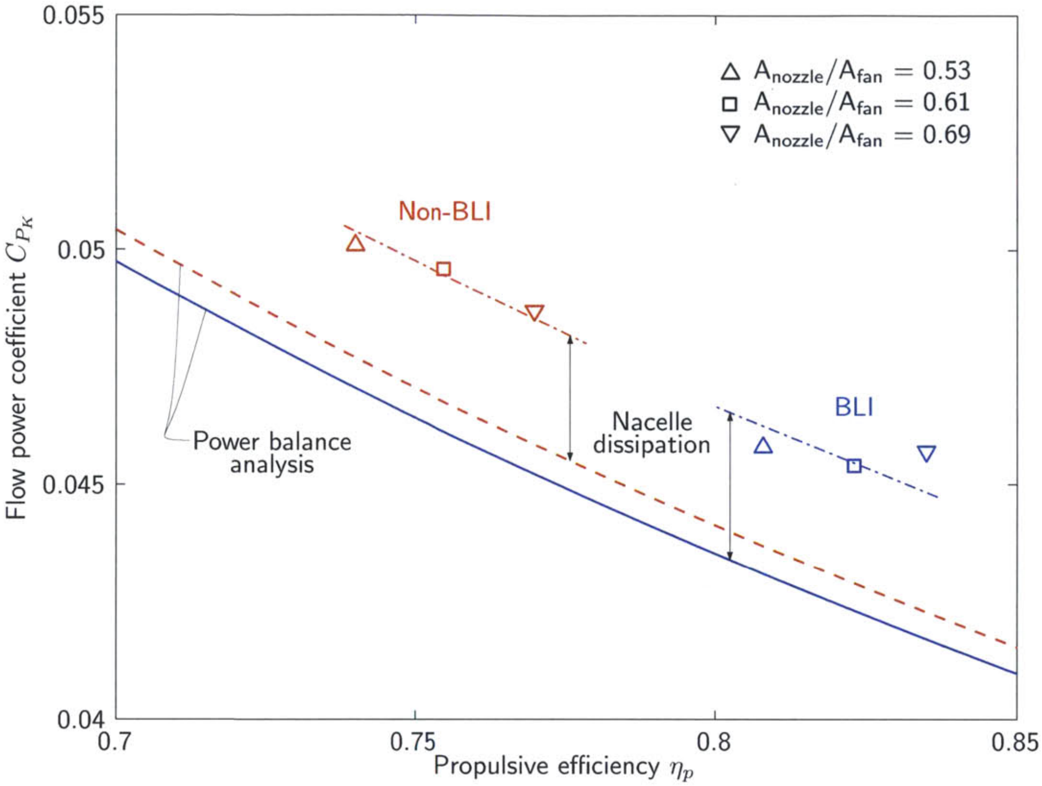

Figure 3-7: D8 wind tunnel model flow power coefficient C_{P_K} vs propulsive efficiency η_p; experimental measurements (symbols) [34] differ from lumped parameter mechanical energy analysis (solid and dashed curves) by approximately constant offset attrubted to propulsion system dissipation.

models, C_X vs C_{P_K}, can be estimated for a design BLI fraction and nozzle area.

Figure 3-7 shows the powered model, C_{P_K}, as a function of propulsive efficiency, η_p, at $C_X = 0$, for BLI and non-BLI configurations. The curves solid and dashed curves show estimated performance based on Equations (3.16) and (3.17). The airframe C'_D is based on measurements with the unpowered model [34]. The ingested surface and wake dissipation was estimated from CFD calculations for this configuration [36]. The symbols show experimentally measured C_{P_K} and η_p at $C_X = 0$ in the non-BLI configuration (podded propulsors) and in the integrated BLI configuration. Both configurations were tested with three nozzle plugs yielding nozzle exit areas that span a range of propulsive efficiencies representative of full-scale values.

There are differences between the measurements and estimates, and these are assumed to be due to the dissipation associated with the propulsion system. An example is nacelle drag, which is not considered in the analysis. This difference, denoted as $\Delta C_{\Phi_{\text{prop}}}$ and $\Delta C'_{\Phi_{\text{prop}}}$ in the BLI and non-BLI configurations, respectively, yields an approximately constant offset in C_{P_K} (~ 0.003) relative to the estimate based on the unpowered airframe performance. For the largest nozzle area in the BLI configuration, C_{P_K} is larger than for a configuration with lower propulsive efficiency, indicating perhaps an increase in external flow dissipation in this geometry and emphasizing the importance of integrated aerodynamic design for these propulsion systems. The other designs behave in accord with the lumped parameter analysis, with reductions in C_{P_K} due to a small ($\sim$ 1% or less) wake dissipation reduction and the major reduction associated with increased propulsive efficiency.

Equation (3.10) can also be modified to provide an estimate of BLI power savings based on the unpowered airframe performance, the propulsive efficiency, and the additional dissipation $\Delta C_{\Phi_{\text{prop}}}$ of each propulsor,

$$\text{PSC} = \frac{C'_{P_K} - C_{P_K}}{C'_{P_K}} = 1 - \frac{\eta'_p}{\eta_p}\left(\frac{C'_D - f_{\text{BLI}} C'_{\Phi_{\text{wake}}} + \Delta C_{\Phi_{\text{prop}}}}{C'_D + \Delta C'_{\Phi_{\text{prop}}}}\right). \tag{3.18}$$

The term in parentheses in Equation (3.18) is close to unity, because $f_{\text{BLI}} C'_{\Phi_{\text{wake}}}$ and the difference between $\Delta C_{\Phi_{\text{prop}}}$ and $\Delta C'_{\Phi_{\text{prop}}}$ are both small (less than 2%) compared to C'_D. The dominant effect of BLI benefit is thus again shown to be the increase in propulsive efficiency.

3.3 BLI Propulsor Performance

The above analysis describes BLI benefit as a reduced propulsive power requirement based on the external aerodynamic performance of a BLI airframe. This section deals with the performance of the propulsor internal flow, specifically (i) the implications of BLI on fan pressure rise, and (ii) the impact of fan efficiency on engine sizing and fuel burn.

3.3.1 Fan Pressure Rise

An important performance metric for propulsors is the stagnation pressure rise. In the incompressible limit, the stagnation pressure rise from propulsor inlet to exit is related to

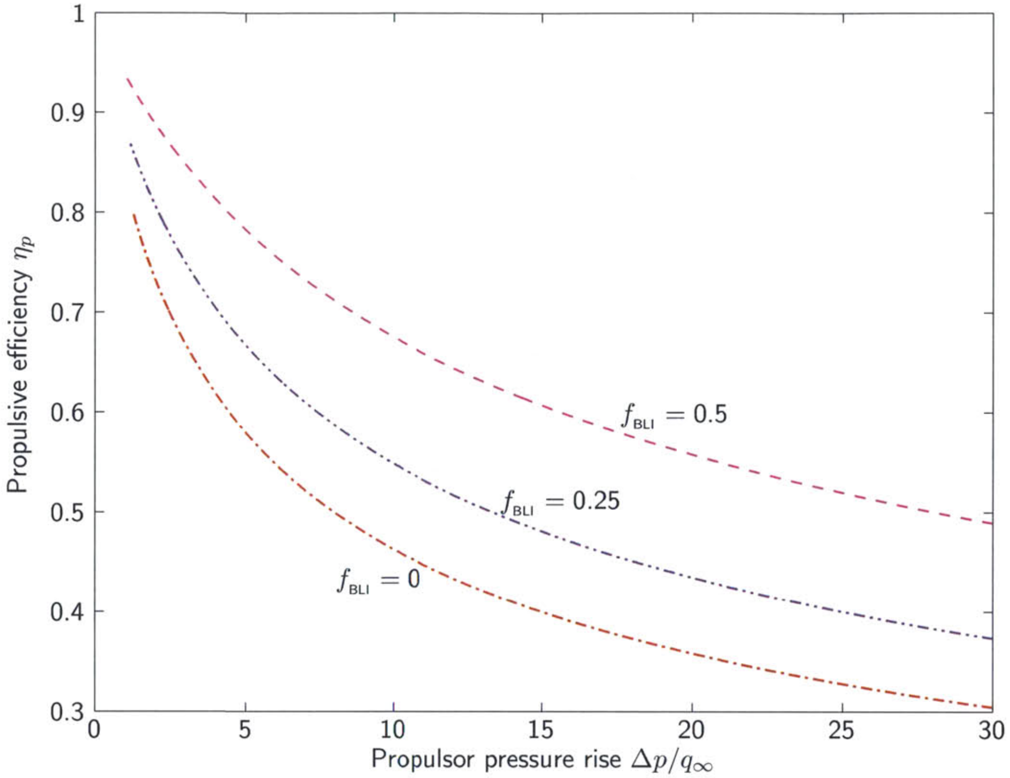

Figure 3-8: Propulsive efficiency versus propulsor stagnation pressure rise coefficient $\Delta p_t/q_\infty$ for body-propulsor configurations with different values of BLI fraction f_{BLI}; increasing BLI fraction increases propulsive efficiency for given propulsor stagnation pressure rise due to reduced inlet mechanical energy flux and jet velocity.

the mechanical power added per unit mass flow,

$$\Delta p_t = \frac{P_K}{\dot{m}/\rho}. \tag{3.19}$$

Figure 3-8 shows propulsive efficiency as a function of propulsor pressure rise normalized by free stream dynamic pressure, $\Delta p_t/q_\infty$, for the body-propulsor configuration examined in Section 3.1 (Figure 3-1). The different curves represent different BLI fractions. Increasing BLI reduces the propulsor inlet stagnation pressure. For a given propulsor pressure rise, therefore, the jet velocity decreases, and the propulsive efficiency increases. If the BLI benefit is realized at *fixed propulsor mass flow*, Equation (3.19) implies that the propulsor pressure rise is lower in the BLI configuration, leading to an increase in propulsive efficiency.

Fan Pressure Ratio

For compressible fan flow, the propulsor stagnation pressure rise is expressed as the fan stagnation pressure ratio, FPR, which can be characterized in terms of the ingested dissipation,

$$\mathrm{FPR} = \frac{p_{t,\mathrm{out}}}{p_{t,\mathrm{inl}}} = 1 + \frac{\Delta p_t}{p_{t\infty} - \frac{f_{\mathrm{BLI}} \Phi_{\mathrm{surf}}}{\dot{m}/\rho}}. \tag{3.20}$$

For a BLI propulsor, two competing effects modify FPR. The increase in propulsive efficiency enables lower stagnation pressure rise for given airframe drag. However, the reduced fan inlet stagnation pressure, reflected in the denominator of Equation (3.20), increases FPR for a given $\Delta p_t / q_\infty$. Figure 3-9 shows propulsive efficiency versus FPR for the D8 aircraft with BLI and non-BLI configurations. Each point has been optimized for minimum fuel burn for a specified FPR. BLI results in increased propulsive efficiency, and the minimum fuel burn design with BLI has a lower FPR than the minimum fuel burn design without BLI. The reduction in pressure rise at fixed mass flow due to a reduced flow power requirement (i.e., the change in the numerator of Equation (3.20)) is therefore the dominant effect of BLI on the selection of FPR for the D8 configuration.

Fan Stage Characteristic

The propulsor sizing just described determines the requirements on the turbomachinery. We can characerize the fan pressure rise in terms of turbomachinery parameters: stage flow coefficient, ϕ, and stagnation pressure rise coefficient, ψ_{TT},

$$\phi = \frac{V_x}{U}, \tag{3.21}$$

$$\psi_{\mathrm{TT}} = \frac{\Delta p_t}{\rho U^2}, \tag{3.22}$$

In Equations (3.21) and (3.22), V_x is the axial velocity entering the stage, and U is the fan tip velocity. Given design values of ϕ and ψ_{TT} and fan hub-to-tip radius ratio, we can define fan stage mean-line velocity triangles and a stage pressure rise characteristic $\psi_{\mathrm{TT}}(\phi)$.

Equations (3.21) and (3.22) can be combined to relate ϕ and ψ_{TT} to airframe (V_∞) and turbomachinery (V_x) quantities.

$$\frac{\Delta p_t}{q_\infty} = \frac{\psi_{\mathrm{TT}}}{\phi^2} \left(\frac{V_x}{V_\infty} \right)^2 \tag{3.23}$$

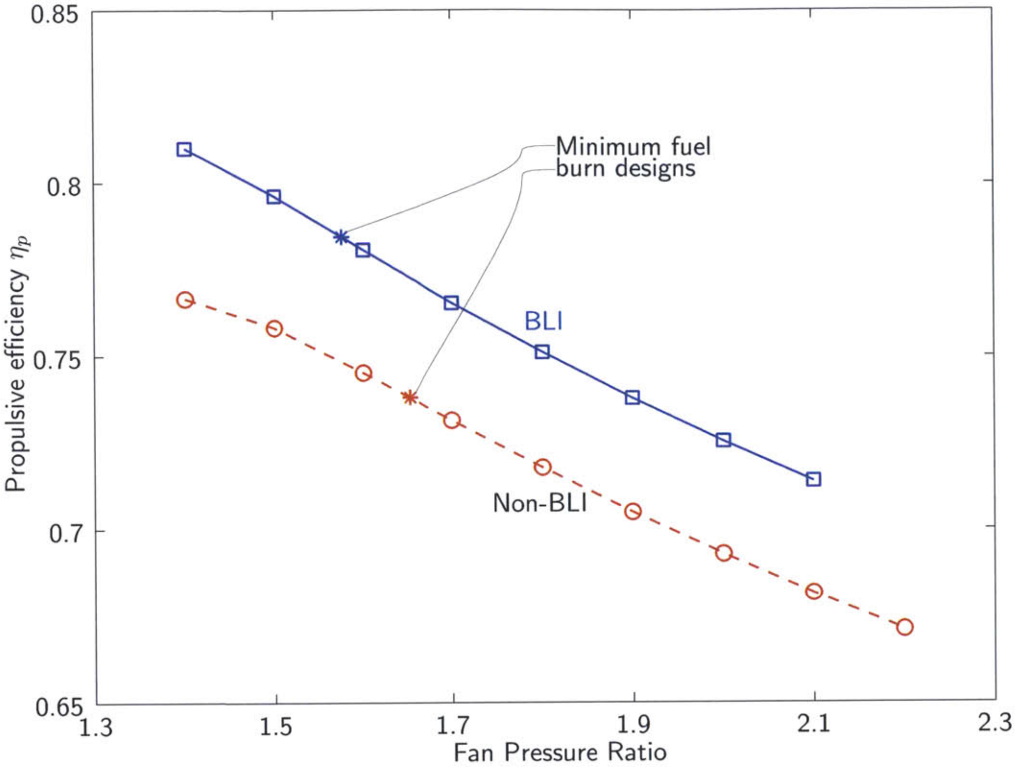

Figure 3-9: Propulsive efficiency versus fan pressure ratio for TASOPT-optimized D8 BLI and non-BLI configurations; minimum fuel burn BLI design has higher propulsive efficiency and lower FPR than non-BLI design.

The axial fan face velocity V_x is set by the fan face Mach number, and Equation (3.23) can be regarded as a constraint on $\psi_{\mathrm{TT}}/\phi^2$. If the BLI benefit is realized at a fixed mass flow, the reduction in propulsor pressure rise results in a reduction of $\psi_{\mathrm{TT}}/\phi^2$. For fixed fan face and tip Mach numbers, ϕ is constant, and BLI will thus result in a reduction in ψ_{TT}. The parallel compressor arguments presented in Chapter 2 demontrate the importance of characteristic slope, and in Chapters 4 and 6, we consider changes in fan stage design point at fixed $\psi_{\mathrm{TT}}/\phi^2$, representing a fixed propulsive power requirement.

3.3.2 Impact of Fan Efficiency on BLI Fuel Burn Benefit

A final consideration in the one-dimensional sizing of the propulsion system is the impact of BLI on turbomachinery performance, and thus fuel consumption. Loss mechanisms specific to BLI inlet distortions, and potential strategies for their mitigation, are addressed in Chapters 4 through 6. From parallel compressor considerations (Chapter 2), however,

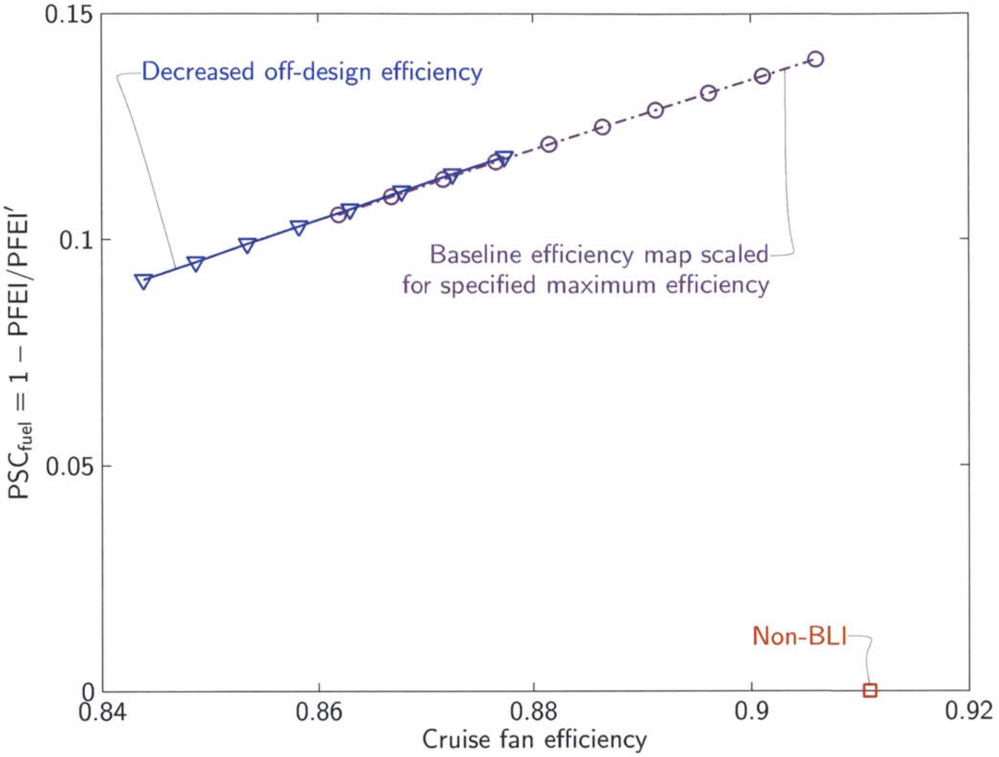

Figure 3-10: Fuel power saving versus cruise fan efficiency for TASOPT-optimized configurations with different assumptions about fan efficiency with BLI; fuel burn increases 0.8% per 1% decrease in cruise fan efficiency.

a conservative esimate is to assume that BLI distortion results in decreased fan efficiency. Peak fan efficiency has been found to decrease by 1-2% for contemporary high bypass turbofans [5] [32]. Decreases in fan efficiency directly affect the BLI benefit because increased shaft power is required to produce a given P_K.

The inlet distortion fuel burn penalty with BLI has been estimated by defining TASOPT-optimized configurations as a function of fan efficiency. The fan maps used in this assessment are based on the performance of the E^3 fan stage, scaled for a given design mass flow, pressure rise, and peak polytropic efficiency as described in the TASOPT documentation [3].

Figure 3-10 shows BLI fuel savings relative to an optimized non-BLI configuration as a function of cruise fan efficiency. The vertical axis is the fuel power savings, equal to the difference in mission fuel burn (or PFEI) between BLI and non-BLI designs normalized by the non-BLI fuel burn. The two lines represent different assumptions about the behavior of off-design fan efficiency: (1)...(2)...Each point represents an optimized configuration for

Case	$(\eta_f)_{\text{max}}$	d_{fan} (in)	$(\eta_f)_{\text{cruise}}$	PFEI (KJ/kg-km)	$(\text{PSC})_{\text{fuel}}$
Podded	0.93	58.5	0.911	5.0775	–
A	0.93	58.6	0.911	4.3484	14.4%
B	0.915	58.6	0.896	4.4047	13.3%
C	0.915	58.5	0.877	4.4771	11.8%

Table 3.2: Fan design parameters and resulting configuration performance for various assumptions about fan efficiency behavior

specified peak fan efficiency and off-design efficiency map. The relation between mission fuel burn and fan efficiency at cruise is not sensitive to fan efficiency at other points in the mission. The mission fuel burn increases by approximately 0.8% for each point decrease in cruise fan efficiency.

Table 3.2 lists fan design and performance parameters for three different points in Figure 3-10. Case A represents a case in which the fan has no increased losses with BLI relative to the podded configuration, resulting in a fuel savings of 14.4%. Case B assumes a decrease in peak fan efficiency from 93% to 91.5%, giving a fuel savings of 13.3%. Case C also has a peak efficiency of 91.5%, but assumes increased losses away from peak efficiency, giving a fuel savings of 11.8%.

To give insight into the behavior of fan size and fuel burn with changes in fan performance, we consider the fan performance over the mission flight envelope for different fan efficiencies, as in Figure 3-11, which shows the fan efficiency maps for Cases A and C. Contours of constant efficiency are shown, with fan pressure ratio on the vertical axis and corrected fan mass flow on the horizontal axis. Comparison of the two graphs illustrates the differences in peak efficiency and off-design losses. The fan operating points for takeoff, climb, cruise, and descent are also shown. The only appreciable difference between the two cases is the reduced mass flow and pressure ratio at top of climb for Case C. This is due to the mission envelope optimization in TASOPT, leading to reduced climb angle at top of climb, rather than a larger fan, to minimize total mission fuel burn. Fan size is not sensitive to the efficiency at top of climb, as evidenced by the constant fan diameter over the range of cases in Table 3.2, and the fuel burn is set by the cruise fan efficiency, as in Figure 3-10.

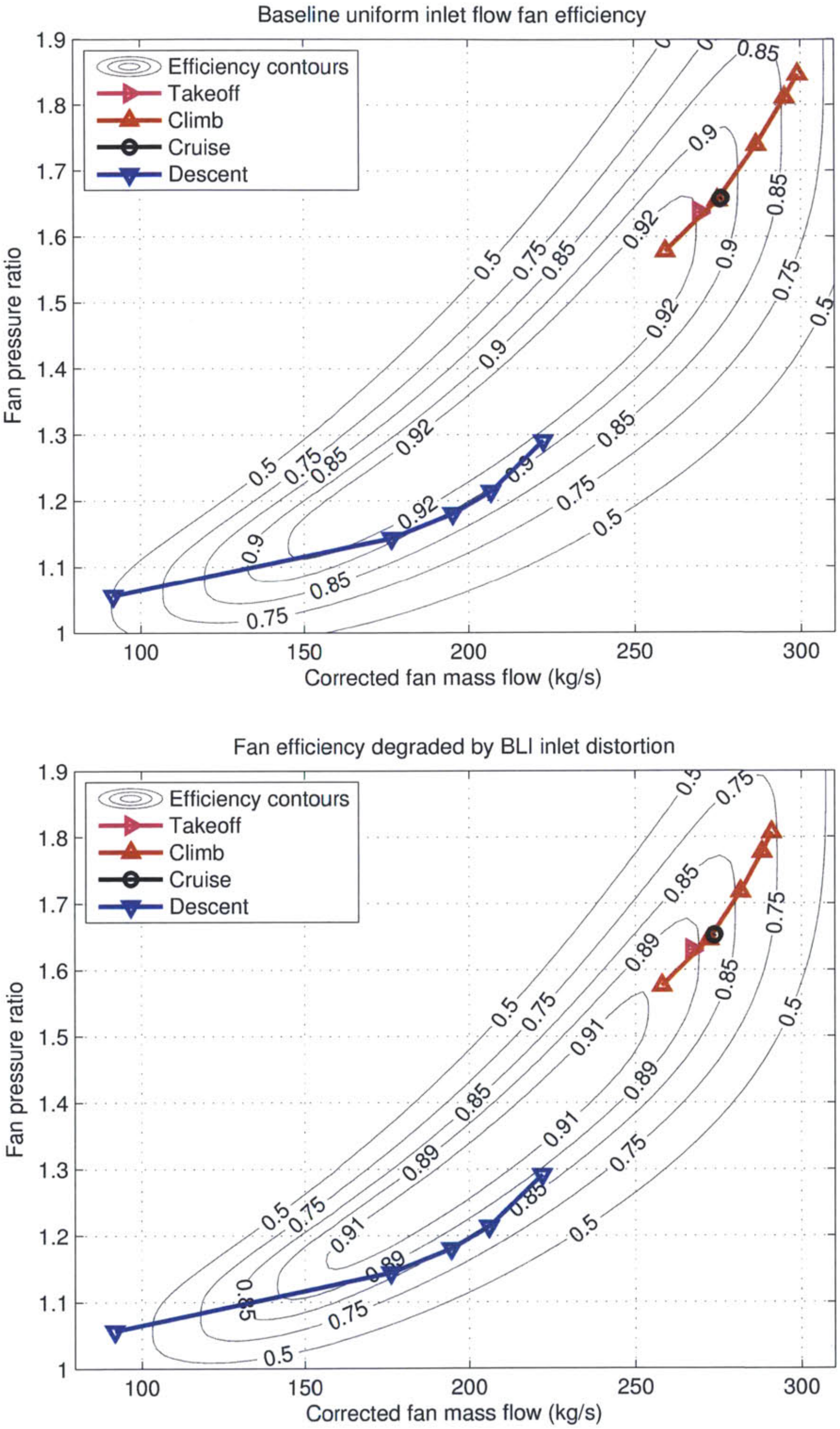

Figure 3-11: Fan maps for case A (top) and C (bottom); contours of fan efficiency versus corrected mass flow and fan pressure ratio; climb angle at top of climb decreases to accommodate decreases in off-design fan efficiency without adversely affecting mission fuel burn.

3.4 Summary

Using a power balance methodology, aircraft BLI benefit has been quantified in terms of the performance of the vehicle to be propelled and the sizing of the propulsor. Analysis of the power saving coefficient shows the benefit results from two physical mechanisms. The first is the reduction in wake dissipation of the ingested boundary layer. The second is the increase in propulsive efficiency for a given propulsive power, enabled by reduced mechanical energy flux at the propulsor inlet. The latter is the dominant contribution to fuel savings.

For a given aircraft, the magnitude of the BLI benefit depends on propulsor size. Optimizations of BLI and non-BLI configurations for similar missions carried out here yield a physical fan size that is almost unchanged, and the benefit of BLI is to enable higher propulsive efficiency without increased propulsor size.

The design of BLI and non-BLI propulsors for powered wind tunnel models have been informed by the analysis of BLI benefit and optimized configuration propulsion system sizing. Experiments to determine the mechanical flow power required at a simulated cruise condition (zero net streamwise force) with nozzle areas that produced a range of representative propulsive efficiencies in both BLI and non-BLI configurations have been carried out. The experimental results for changes in propulsive efficiency and BLI are consistent with the analysis, confirming the propulsive efficiency benefit of BLI and the utility of the power balance method.

The analysis shows substantial fuel burn benefit even with potential fan efficiency deficits due to BLI. Further, the optimal propulsor sizing is not sensitive to fan efficiency, so the aerodynamic benefits described can be treated independently of the internal propulsor performance.

Chapter 4

Two-Dimensional Circumferential Distortion Analysis

In this chapter, we consider the behavior of quasi-two-dimensional flow through a fan stage section with inlet circumferential stagnation pressure distortion. The assumption made is small amplitude circumferential perturbations in the geometry and flow quantities so that a linearized treatment can be used, and the turbomachinery rows are represented by actuator disks. The analysis allows us to assess the impact of inlet distortion on fan stage performance as a function of the design parameters of the blading and the installation. Determination of the sensitivity of the fan distortion response in turn gives insight into strategies to mitigate the effect of BLI on fan efficiency.

4.1 Flow Description

We consider an annular domain with constant mean radius, as in Figure 4-1a. If the annulus height is small compared to the mean radius, radial accelerations can be ignored, and a radially-averaged two-dimensional analysis can be used to described the fluid motion in the "unrolled" flowpath geometry in Figure 4-1b. The resulting two-dimensional computational domain is shown in Figure 4-1c. The turbomachinery blading is modeled using actuator disks that produce discontinuities in circumferential velocity and stagnation pressure at a given location as a function of the local flow. This type of analysis has been used effectively to describe the distortion response of compressors with high hub-to-tip ratio [21].

The linearized description of the two-dimensional flow field has perturbations in velocity

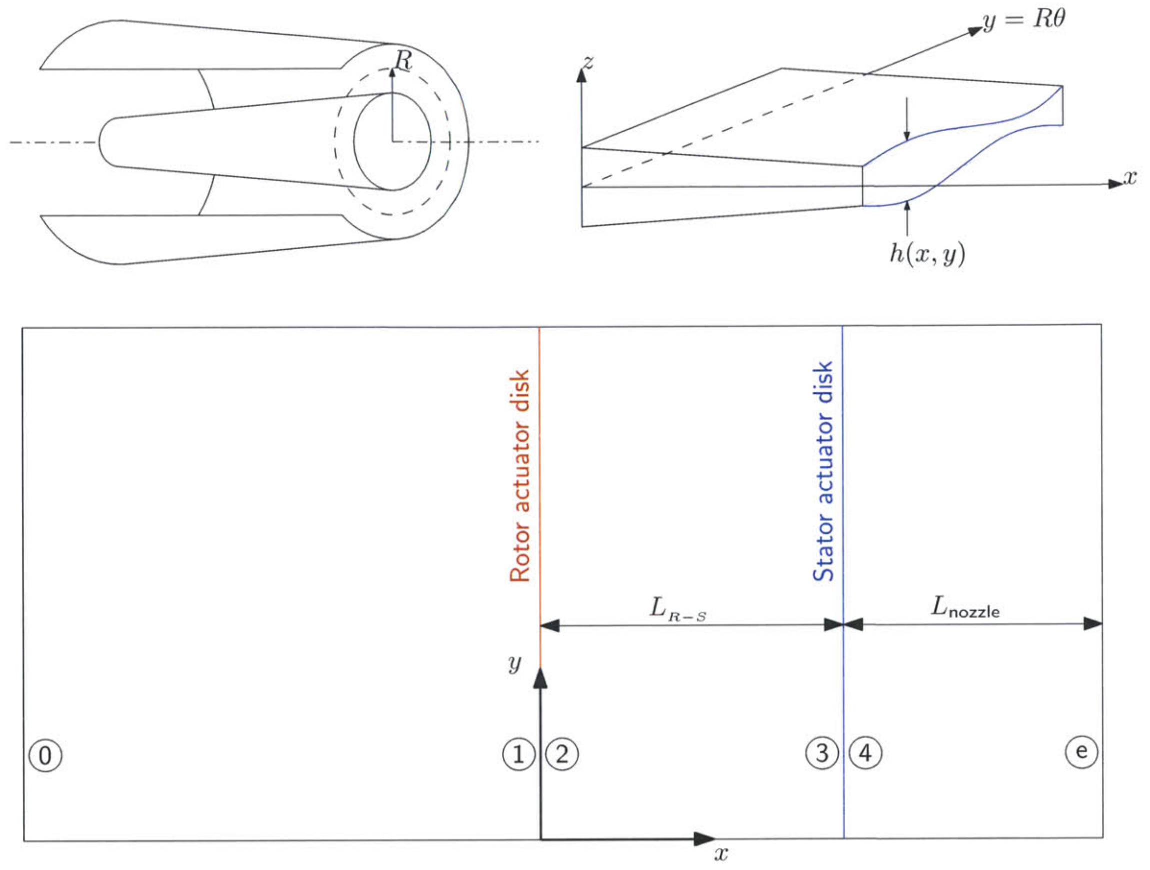

Figure 4-1: Model flow geometry: annular flow path (top left), "unrolled" geometry (top right) with axial and circumferential variations in passage height, and two-dimensional computational domain with rotor and stator actuator disks (bottom).

and stagnation pressure, represented with primes, about an axisymmetric mean flow,

$$u(x, y) = U(x) + u'(x, y), \tag{4.1}$$

$$v(x, y) = V(x) + v'(x, y), \tag{4.2}$$

$$p_t(x, y) = P_t(x) + p_t'(x, y), \tag{4.3}$$

where $u', v' \ll U$ and $p_t' \ll \rho U^2$. The flowpath geometry (annulus height) is also expressed in terms of an axisymmetric mean and a small non-axisymmetric perturbation,

$$h(x, y) = H(x) + h'(x, y), \tag{4.4}$$

where $h' \ll H$.

The flow outside the actuator disks is taken as incompressible and inviscid. The equations of motion, derived in Appendix A, can be expressed separately for the mean flow and perturbation quantities. The equations for the mean flow are:

$$\frac{d}{dx}(UH) = 0, \tag{4.5}$$

$$\frac{d}{dx}(RV) = 0, \tag{4.6}$$

$$\frac{dP_t}{dx} = 0. \tag{4.7}$$

The equations for the perturbation flow are:

$$\frac{\partial u'}{\partial x} = -u'\frac{1}{H}\frac{dH}{dx} - \frac{\partial v'}{\partial y} - \left(\frac{U}{H}\frac{\partial h'}{\partial x} + \frac{V}{H}\frac{\partial h'}{\partial y} + \frac{h'}{H}\frac{dU}{dx}\right), \tag{4.8}$$

$$\frac{\partial v'}{\partial x} = \frac{\partial u'}{\partial y} - \frac{1}{\rho U}\frac{\partial p_t'}{\partial y}, \tag{4.9}$$

$$\frac{\partial p_t'}{\partial x} = -\frac{V}{U}\frac{\partial p_t'}{\partial y}. \tag{4.10}$$

Equation (4.8) is equivalent to the continuity equation. Equations (4.9) and (4.10) are equivalent to the momentum equations, expressed in terms of stagnation pressure rather than static pressure to simplify the calculation procedure. The flow is circumferentially periodic, and we represent perturbation quantities and their derivatives with respect to y with a complex Fourier coefficient. Equations (4.8)-(4.10) thus yield a system of one-dimensional ordinary differential equations which can be solved numerically. These are given in Appendix A.

The rotor and stator actuator disks represent the effect of the turbomachinery by producing a change in relative flow angle at constant axial velocity (i.e., constant mass flow across the disk). The rotor exit flow angle is determined from the stage stagnation ethalpy rise coefficient, ψ, and flow coefficient ϕ,

$$\tan\beta_2 = \frac{v_2 - \Omega R}{u_2} = \frac{1-\psi}{\phi}. \tag{4.11}$$

The rotor stagnation pressure rise is determined as a function of the change in circumferential velocity using the Euler turbine equation and neglecting rotor losses. The stator actuator disk turns the flow to a specified stage exit flow angle at constant axial velocity and stagnation pressure.

Solution of Equations (4.8)-(4.10) requires three boundary conditions. At the inlet, far upstream of the rotor, a stagnation pressure perturbation is specified, with zero circumferential velocity,

$$p'_{t,\mathrm{inl}} = \delta p_{t,\mathrm{inl}} e^{i\theta}, \tag{4.12}$$

$$v'_{\mathrm{inl}} = 0. \tag{4.13}$$

At the nozzle exit, We assume uniform static pressure. Equation (4.9) can be expressed in terms of static pressure so the exit boundary conditions can be expressed in terms of circumferential velocity:

$$-\frac{1}{\rho U_{\mathrm{out}}} \frac{\partial p'_{\mathrm{out}}}{\partial y} = \frac{\partial v'_{\mathrm{out}}}{\partial x} = 0. \tag{4.14}$$

The numerical flow field solution is described in Appendix A. Equations (4.8)-(4.10) are integrated numerically from the domain inlet to exit given the inlet conditions (4.12), (4.13), as a function of inlet axial velocity perturbation u'_{inl}. This yields a flow field solution with a residual $\mathcal{R}$ for the exit boundary condition (4.14),

$$\mathcal{R}(u'_{\mathrm{inl}}) = \frac{\partial v'_{\mathrm{out}}}{\partial x}. \tag{4.15}$$

Equation (4.15) is solved numerically for $\mathcal{R} = 0$, yielding the inlet velocity u'_{inl} and a resulting flow field that satisfies Equation (4.14).

4.2 Circumferential Distortion Response

Computations of the distortion flow field as a function of design point stangation enthalpy rise coefficient and flow coefficient, axial spacing between the rotor, stator, and nozzle exit, and flowpath geometry have been carried out. In this section, we examine the flow field for the simplified case with constant annulus height, h, and no axial space between the rotor and stator actuator disks, $L_{\text{R-S}} = 0$, which can be solved analytically. The resulting flow field exhibits upstream redistribution and distortion transfer behavior that are qualitatively similar for other two- and three-dimensional geometries.

4.2.1 Flow Field Behavior

Figure 4-2 shows circumferential distributions of perturbation stagnation pressure, static pressure, axial velocity, and tangential velocity, at locations far upstream, and at the rotor and stator actuator disk inlets. The stagnation pressure perturbation is convected unchanged along axial streamlines upstream of the rotor. Interaction between the inlet distortion and fan creates a static pressure perturbation upstream of the rotor that attenuates the axial velocity perturbation, and that results in upstream flow redistribution ang generation of a circumferential velocity perturbation entering the rotor. The rotor actuator disk reacts to the inlet velocities to produce larger turning and pressure rise in the low stagnation pressure region, consistent with compressor pressure rise characteristics, reducing the magnitude of the stagnation pressure distortion downstream of the rotor.

Downstream of the rotor, the non-dimensional stagnation pressure and axial velocity distributions are equal, to satisfy the stator exit condition of constant static pressure. The tangential velocity perturbation is in phase with the axial velocity pertubation, satisfying the rotor actuator disk exit angle, β_2. For the design point considered here, this results in an amplification of the tangential velocity perturbation across the rotor.

4.2.2 Blade Row Performance

The analysis provides flow field quantities at the rotor and stator actuator disk locations that we can use to estimate the impact of distortion on propulsor performance. The velocity components immediately upstream of each actuator disk yield the perturbations in the blade relative inlet angles as a function of the stage design,

$$\beta_1 = \overline{\beta_1}^{\theta} + \beta_1' = \tan^{-1}\left(\frac{v_1 - \Omega R}{u_1}\right) \tag{4.16}$$

$$\alpha_3 = \overline{\alpha_3}^{\theta} + \alpha_3' = \tan^{-1}\left(\frac{v_3}{u_3}\right) \tag{4.17}$$

In a real flow through turbomachinery blading, losses (which are not included in this analysis) increase with perturbations in inlet flow angle because parts of the blade row are operating at off-design conditions (i.e. away from minimum-loss incidence).

Figure 4-3 shows the rotor and stator inlet angle perturbations for the flow field of Figure 4-2. The vertical axes are the rotor and stator inlet angle perturbations normalized

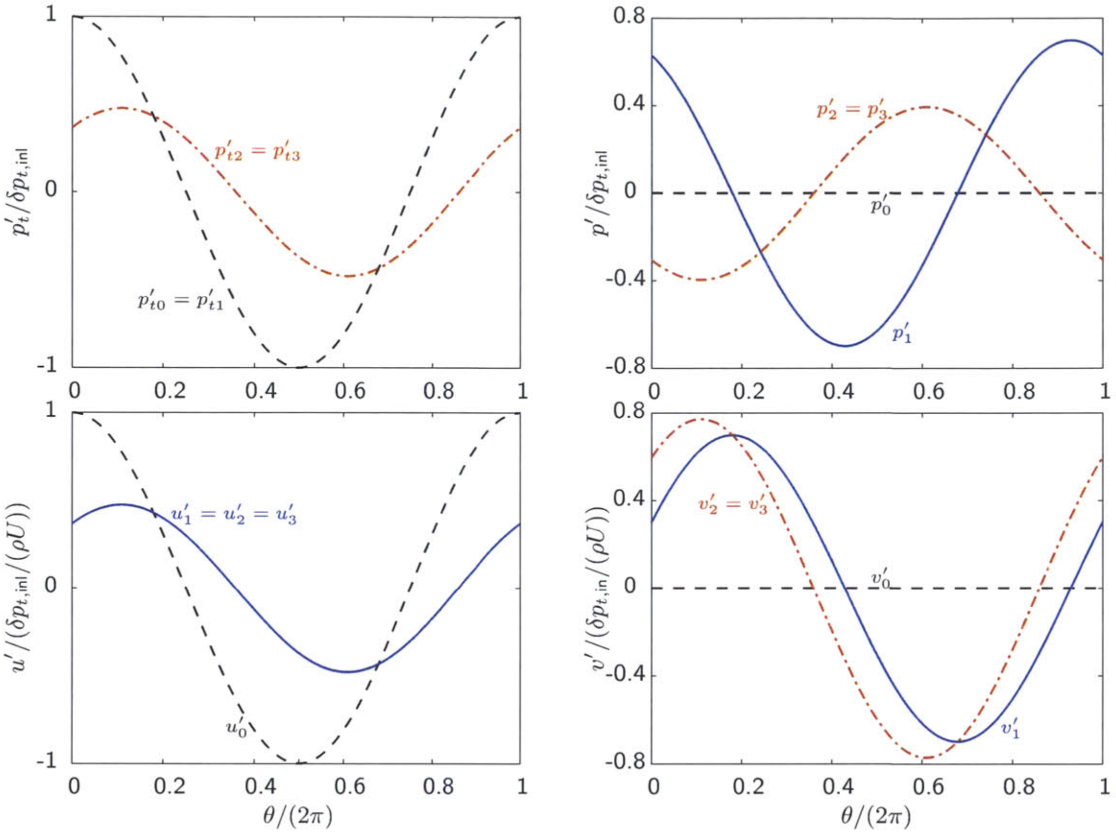

Figure 4-2: Circumferential distributions of perturbation stagnation pressure (top left), static pressure (top right), axial velocity (bottom left), and circumferential velocity (bottom right), stagnation pressure, and static pressure, normalized by the inlet stagnation pressure distortion magnitude; the analysis captures upstream axial velocity distortion attenuation, swirl generation, and rotor distortion transfer.

by the magnitude of the inlet stagnation pressure distortion,

$$\beta_1' = \frac{\phi^2}{1+\phi^2}\left(-\frac{1}{\phi}\frac{u_1'}{U_1} + \frac{v_1'}{U_1}\right), \tag{4.18}$$

$$\alpha_3' = \frac{\phi^2}{\phi^2 + \left(\frac{H_3}{H_1}\right)^2 \psi^2}\frac{H_3}{H_1}\left(-\frac{H_3}{H_1}\frac{\psi}{\phi}\frac{u_3'}{U_1} - \frac{v_3'}{U_1}\right). \tag{4.19}$$

For the case considered here, the rotor incidence perturbation is approximately in phase with the rotor axial velocity distortion, and the stator incidence distortion is approximately three times as large as in the rotor.

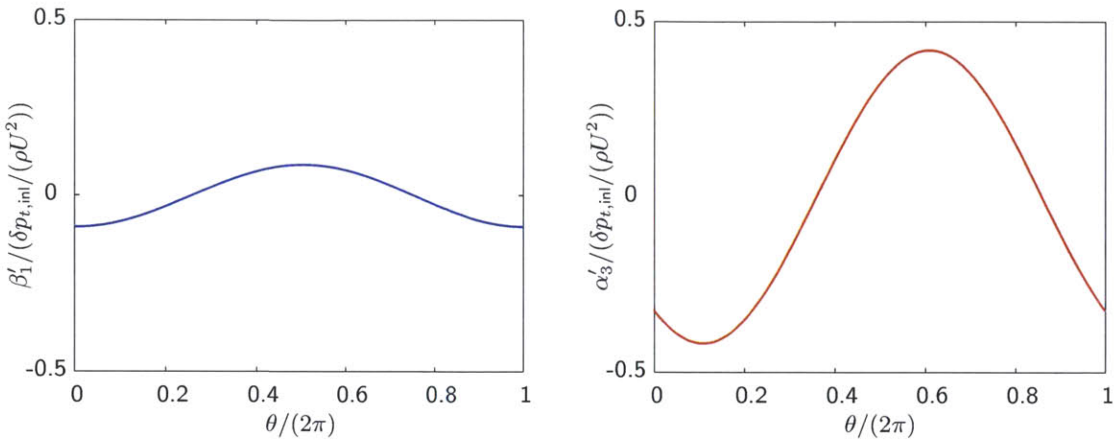

Figure 4-3: Circumferential distributions of inlet flow angle perturbations for rotor (left) and stator (right)

4.3 Sensitivity of Performance to Design Parameters

In this section, we assess stage performance for a range of different propulsor design parameters: stage stagnation enthalpy rise and flow coefficients, axial spacing between rotor and stator, and flowpath geometry.

4.3.1 Design Point Loading and Flow Coefficient

The design point flow coefficient ϕ and stagnation enthalpy rise coefficient ψ determine the stage velocity triangles and stagnation enthalpy rise characteristic $\psi(\phi)$. Figure 4-4 shows five (ϕ, ψ) design points and the resulting ideal stagnation enthalpy rise characteristics. The design points represent a baseline similar to the tip section of the fan considered in the next chapter ($\phi = 0.47$, $\psi = 0.24$) and changes of ±20% in stagnation enthalpy rise at fixed ϕ and fixed ψ/ϕ^2. The former represents changes in the local blade geometry at fixed wheel speed, and the latter represents changes in both wheel speed and blade geometry at a fixed thrust. The enthalpy rise characteristics (dashed lines), show how changes in the design point velocity triangles change the characteristic slope, with steeper slopes for lower values of ϕ and ψ.

Figure 4-5 shows rotor and stator incidence distortions for zero axial rotor-stator spacing ($L_{\text{R-S}} = 0$) and constant annulus height h. The vertical axis is the stagnation enthalpy rise coefficient ψ and the horizontal axis is the flow coefficient ϕ. Contours of constant $\delta\beta_1/(\delta p_{t,\text{inl}}/(\rho U^2))$ and $\delta\alpha_3/(\delta p_{t,\text{inl}}/(\rho U^2))$ are shown. The design points of Figure 4-4 are

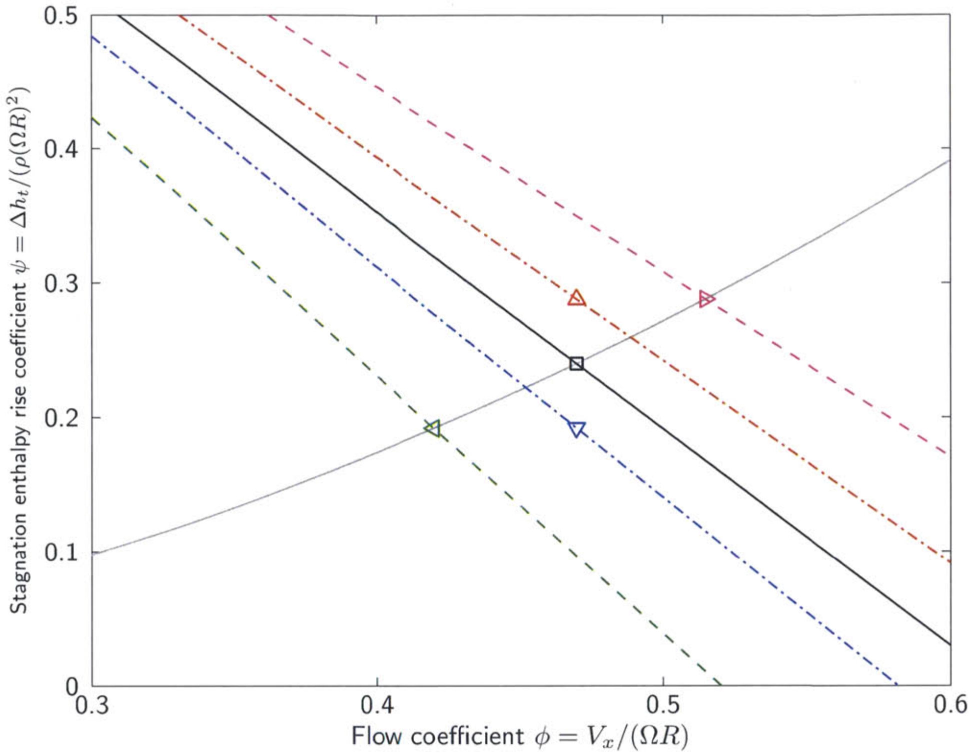

Figure 4-4: Two-dimensional stage (ϕ, ψ) design points (symbols), stagnation enthalpy rise characteristics (diagonal lines), and constant ψ/ϕ^2 propulsive power requirement (gray parabola).

also shown. The rotor inlet angle perturbation decreases for steeper characteristic slopes, indicating the axial velocity attenuation has a larger impact than the upstream swirl. The stator inlet angle perturbation can be an order of magnitude larger than the rotor, depending on the stage design point. Perturbations in swirl velocity have a larger impact on flow angle distortions for lower stage stagnation enthalpy rise, where the mean stator inlet flow angle is lower, and the stator incidence distortion increases with decreases in stage loading within the range of representative designs.

4.3.2 Distortion-Component Interactions with Axisymmetric Installation

Rotor-Stator Interaction

Figure 4-6 shows the blade row performance in the same representation as Figure 4-5, but with increased rotor-stator axial space, $L_{\text{R-S}} = 2\pi R$. The behavior in rotor incidence distortion is qualitatively similar to the $L_{\text{R-S}} = 0$ case, with increases of 35-70% as the

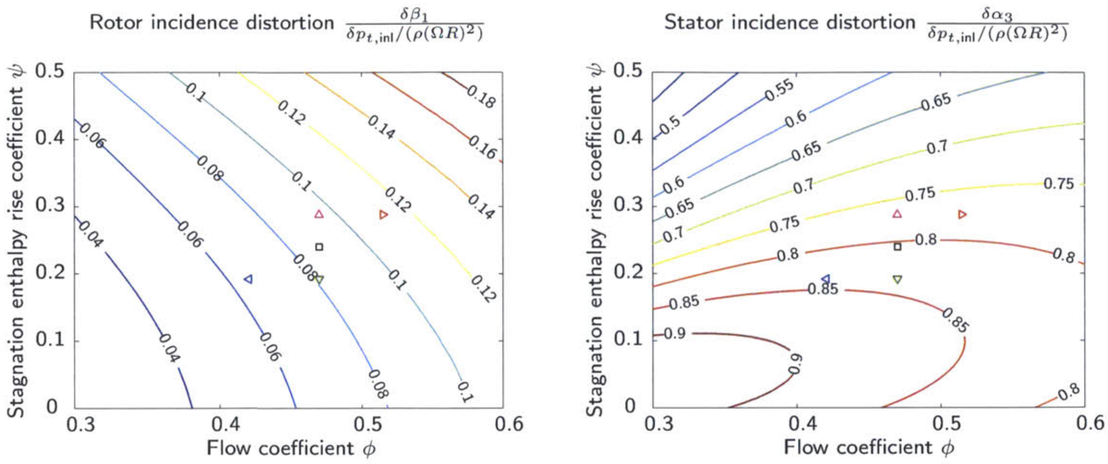

Figure 4-5: Rotor (left) and stator (right) incidence distortion versus stage flow coefficient ϕ and enthalpy rise coefficient ψ for $L_{\text{R-S}} = 0$ and constant flow path area

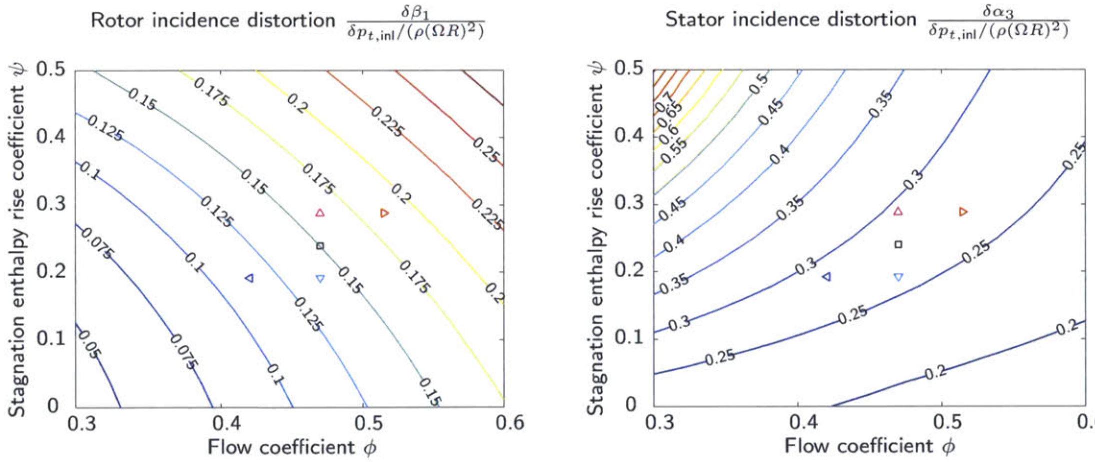

Figure 4-6: Rotor (left) and stator (right) incidence distortion versus stage flow coefficient ϕ and enthalpy rise coefficient ψ for $L_{\text{R-S}} = 2R$ and constant flow path area

spacing is increased. Increasing the axial spacing reduces the stator incidence distortion by up to 95% relative to the close-spaced case at lower loadings.

Figure 4-7 shows the variation in incidence distortion as a function of rotor-stator spacing for the five representative design points in Figures 4-5 and 4-6. For $L_{\text{R-S}} < 2R$, the distortions in both blade rows change monotonically with $L_{\text{R-S}}$. Minimum rotor incidence distortion occurs at $L_{\text{R-S}} = 0$ and stator incidence distortion decreases with increasing rotor-stator axial distance. The incidence distortion behavior with respect to axial spacing is not sensitive to the stage design point velocity triangles, and the variations are strongest in the stator. For $L_{\text{R-S}} \approx 3R$, the stator is sufficiently far downstream that the two blade rows do

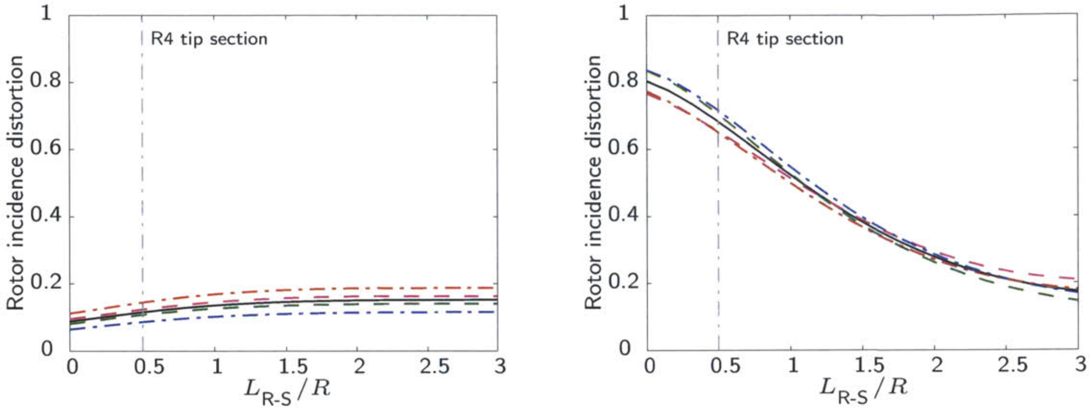

Figure 4-7: Rotor (left) and stator (right) incidence distortion versus axial rotor-stator spacing for representative (ϕ, ψ) design points

not interact, so increasing the spacing further does not affect conditions at either.

Axisymmetric Flowpath Area Variations

The sensitivity analysis has been carried out so far at *fixed flow path area.* Figure 4-8 shows blade row incidence distortion for a stage with a downstream nozzle, as a function of nozzle area ratio and nozzle length. The incidence distortion in both blade rows decreases for increasing $|dh/dx|$ whether from increased nozzle area ratio or decreased nozzle length. This is in qualitative agreement with parallel compressor theory, which predicts that a favorable static pressure perturbation at the stator exit moves the operating points of the two parallel streams closer together on the compressor characteristic, reducing the stage velocity distortion. As the nozzle length is increased, the interaction between the nozzle and the stator becomes weaker, and the velocity distortions increase.

4.3.3 Non-Axisymmetric Geometry and Flowpath Effects

Circumferential variations in geometry can potentially be used to generate perturbations in the static pressure field to reduce the blade row inlet flow angle distortions. Here we consider two strategies: non-axisymmetric stator exit flow angle and non-axisymmetric flowpath geometry.

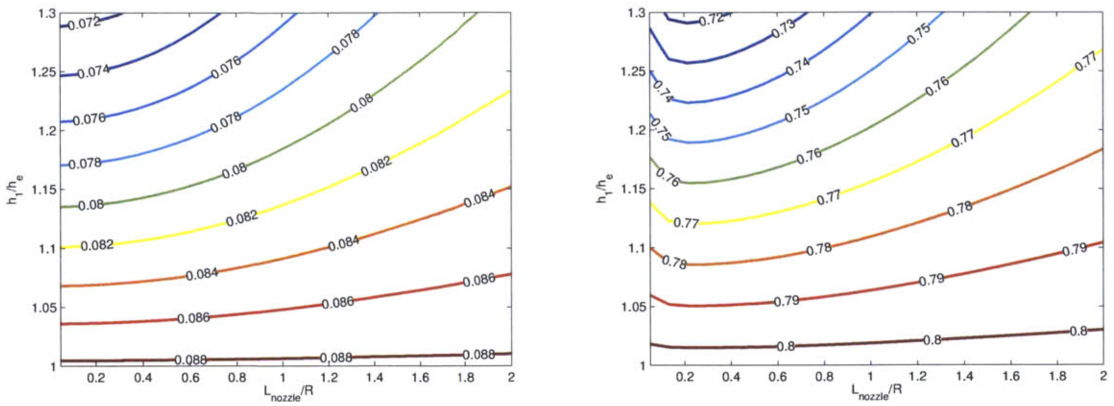

Figure 4-8: Rotor (left) and stator (right) incidence distortion versus downstream nozzle area ratio and axial length; $\phi = 0.47$, $\psi = 0.24$, $L_{\text{R-S}} = 0$

Non-axisymmetric Stator Exit Flow Angle

Figure 4-9 shows blade row incidence distortion for the baseline stage design ($\phi = 0.47$, $\psi = 0.24$, $L_{\text{R-S}} = 0$, $h =$ constant) with circumferential perturbations in the stator exit angle distribution, about a mean exit angle of zero,

$$\alpha_4' = \delta\alpha_4 e^{i(\theta - \theta_{\alpha_4})}. \tag{4.20}$$

The horizontal axis is the magnitude of the exit angle perturbation normalized by the upstream stagnation pressure perturbation magnitude, $\delta\alpha_4/(\delta p_{t,\text{inl}}/(\rho U^2))$. The vertical axis is the difference in phase θ_{α_4} between the perturbations in stator exit angle and the far upstream inlet stagnation pressure. The contours of inlet flow angle perturbations show non-axisymmetric stator angle variations, magnitude and phase, that minimize incidence distortion for each blade row. For the design point considered, the stator distortion is minimized for a stator angle perturbation approximately 180° out of phase with the inlet stagnation pressure distortion. The rotor distortion is minimized for a stator angle perturbation approximately 270° out of phase with the upstream stagnation pressure distortion and twice the angle perturbation magnitude relative to the design for minimum stator incicence. Each design effectively eliminates incidence distortion for either the rotor or stator.

For constant annulus height downstream of the stator, an exit angle perturbation yields

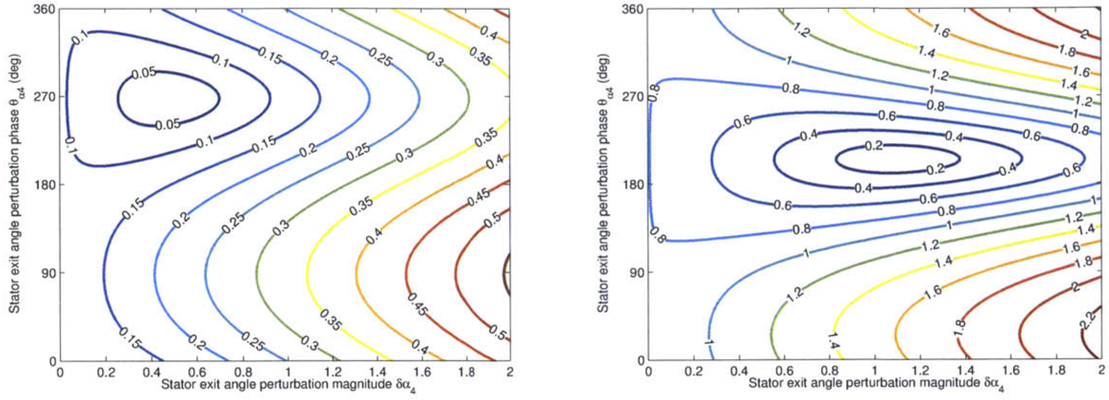

Figure 4-9: Rotor (left) and stator (right) incidence distortion versus stator exit angle perturbation phase relative to the inlet stagnation pressure perturbation, and stator exit angle perturbation phase; $h =$ constant, $\phi = 0.47$, $\psi = 0.24$, $L_{\text{R-S}} = 0$

a static pressure perturbation with 90° difference in phase,

$$\frac{\delta p_4}{\rho U^2} e^{i\theta_p} = \delta\alpha_4 e^{i\left(\theta_{\alpha_4} + \frac{\pi}{2}\right)}. \tag{4.21}$$

The non-axisymmetric stator geometry with θ_{α_4} thus provides a back pressure perturbation in phase with the upstream stagnation pressure perturbation and minimizes non-uniformity in the rotor.

Non-axisymmetric Flowpath Geometry

A non-axisymmetric pressure field can also be generated with a circumferentially non-uniform downstream annulus height. Figure 4-10 shows rotor and stator incidence distortion for the baseline mean stage geometry with linearly increasing annulus height perturbation for a distance $x_e - x_4 = R/2$ downstream of the stator,

$$h'(x, y) = \delta h \frac{x - x_4}{x_e - x_4} e^{i(\theta - \theta_h)}. \tag{4.22}$$

The horizontal axis in Figure 4-10 is the nozzle exit height perturbation $\delta h / H_1$, and the vertical axis is the phase θ_h relative to the upstream stagnation pressure distortion. Because the perturbation pressure field is strongest farther downstream, the non-axisymmetric nozzle gives a smaller reduction in blade row incidence distortion than that due to the stator exit flow angle. Although the behavior as δh increases suggests solutions that provide minimum

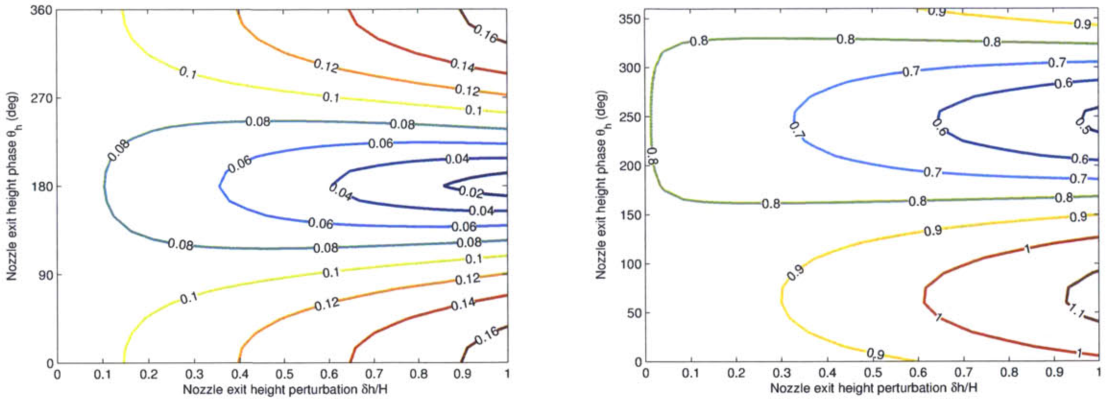

Figure 4-10: Rotor (a) and stator (b) incidence distortion versus nozzle exit height perturbation phase and magnitude

distortion in each blade row, similar to the behavior with stator exit angle perturbations, these geometries violate the assumption of small perturbations ($h \ll H$) and may not even be realizable ($h < H$).

4.3.4 Discussion

The numerical results show changes in blade row incidence distortion, which we consider as a surrogate for blade row losses, for changes in different fan stage geometries. Based on the incidence distortion sensitivities, we can identify propulsor design attributes that have the potential to mitigate the effect of BLI on fan stage efficiency.

The rotor performance is found to be qualitatively described by parallel compressor theory, with steeper stage characteristic slopes producing stronger distortion attenuation, more uniform flow, at the rotor inlet. The stator inlet angle perturbations depend strongly on the axial spacing between the rotor and the stator. The estimated flow angle distortions may be as high as 25° in the stator and 6° in the rotor with BLI for a representative fan stage tip section.

Performance of both blade rows improves with increasing streamtube contraction rate. For a given propulsor design, however, the nozzle area ratio is constrained by the propulsive power and propulsive efficiency of the configuration, and short axial length is desirable to reduce external nacelle drag, leaving little flexibility to alter the overall area contraction ratio. We will see that for three-dimensional flows, variations in the radial loading distribution will lead to variations in local streamtube area contraction. This introduces another potential tradeoff in the design, with an increase in local design point loading leading to a favorable increase in the local streamtube contraction, at the cost of less favorable characteristic slope.

We have illustrated the effects of *non-axisymmetric* design with two examples showing performance with non-axisymmetric stator exit angle distributions and non-axisymmetric nozzle flowpath geometries. Non-axisymmetric stators could be used to generate a stator exit static pressure distribution that results in favorable flow conditions at the rotor or stator inlet; circumferential variations in stator geometry are already in use to deal with different types of circumferential distortions. One can envision a stator geometry that produces a favorable reduction in rotor inlet angle perturbations via non-axisymmetric exit angle distribution, and a leading edge metal angle distribution designed to accept the expected perturbation in stator inlet flow angle.

Perturbation pressure fields were obtained with a non-axisymmetric flow path geometry downstream of the stator. To achieve similar reductions in rotor and stator incidence as with stator angle variations, however, perturbations in annulus geometry approaching the average annulus height are required. Perturbations in stator exit angle are thus more effective than the nonaxisymmetric flowpath geometry considered at producing static pressure perturbations at the blade rows, due to the axial distance between the stator and the maximum annulus height perturbation. This difficulty is increased for three-dimensional flow in low hub-to-tip ratio fan stages, where perturbations in end wall geometry have less effect on the flow away from the wall.

The results of the analysis show the important distortion-component mechanisms for two-dimensional circumferential distortion response and the impact of changes in stage design parameters on flow non-uniformity. In Chapter 5, we will see the same qualitative mechanisms are present, but we will also see that a three-dimensional analysis is required to capture their quantitative effect on conditions at the blade rows. In Chapter 6, we investigate the impact of stage design point, radial loading distribution, rotor-stator spacing, and non-axisymmetric stator geometry on three-dimensional fan stage performance with inlet distortion.

4.4 Summary

A two-dimensional linearized analysis has been developed to analyze the sensitivity of propulsor circumferential distortion response to fan stage turbomachinery design and installation. The analysis includes three-dimensional variations in flow path geometry and represents the turbomachinery with rotor and stator actuator disks. The analysis shows features of the upstream redistribution of the flow, including axial velocity attenuation and swirl generation, distortion transfer across the rotor based on the actuator disk pressure rise characteristic and local flow conditions, and distortion attenuation due with a downstream nozzle. Perturbations in relative inlet flow angle at the rotor and stator locations are determined and used as a surrogate for potentially increased blade losses with distortion.

The results of the analysis show the sensitivity of rotor and stator incidence distortion to changes in propulsor design parameters (design point velocity triangles, axial spacing between the rotor and stator, and annular flow path geometry) and to nonaxisymmetric installation features (stator exit flow angle and annulus height). Design attributes that provide favorable velocity distributions with inlet distortion have been identified. The effectiveness of these design attributes for three-dimensional, low hub-to-tip ratio fan stage geometries is assessed in Chapter 6.

Chapter 5

Three-Dimensional Fan Stage Distortion Response Analysis

This chapter describes a three-dimensional analysis of turbomachinery blade row response to inlet distortion. The blading is approximated as momentum and energy source distributions that represent the bladed flow field in a pitchwise-averaged sense. This approximation, namely the assumption that the distortion length scale is large compared to the blade pitch, allows full-wheel flow field calculations at greatly reduced computational cost compared to unsteady calculations that resolve the unsteady flow through individual blade passages.

The source term distributions are defined based on a specified blade camber surface geometry. The combination of reduced computational cost with parametrically defined blading geometry makes the model appropriate for determining the sensitivity of fan distortion response to stage design, where many different geometries are considered. Comparison of the results with higher fidelity computations shows the flow description is appropriate for the problem of interest.

5.1 Turbomachinery Source Term Model

The basic concept that underpins the analysis is illustrated schematically in Figure 5-1. The blading geometry is replaced with an axisymmetric volume covering the meridional extent of the blade. Within this volume, momentum and energy source term distributions generate flow turning, pressure rise, and temperature rise representative of that produced by the actual geometry. The absence of blades allows for a coarser computational mesh

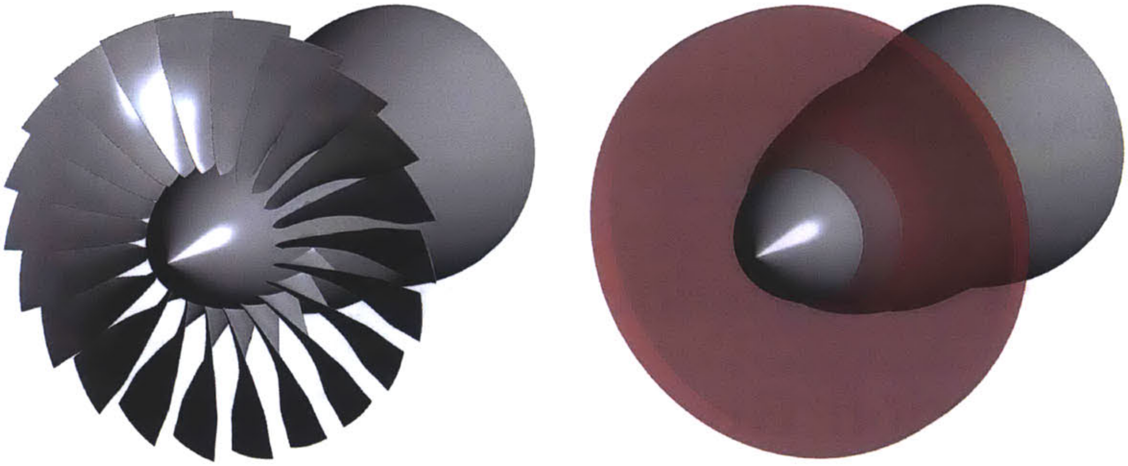

Figure 5-1: Three-dimensional blading geometry represented as a continuous distribution of momentum and energy source terms within the blade row swept volume

than required to resolve the blading geometry. Unsteady effects are ignored, based on the low reduced frequency of the BLI distortions considered.

5.1.1 Approximate Flow Description

The effect of the blading is captured in a pitchwise-averaged sense, as illustrated for a two-dimensional cascade flow in Figure 5-2. Details of the blade-to-blade flow, such as blade surface pressure coefficient distribution, are not captured. For *uniform* inlet flow conditions, the source distribution generates an axisymmetric flow field equivalent to the circumferential average of the actual flow. In this context, the momentum source distribution can be seen as the local blade force distributed uniformly across the width of a blade passage. Similarly, the energy source distribution represents blade work, which is related to the circumferential blade force in rotating blade rows.

For *non-axisymmetric flows*, as encountered with BLI, the source term distributions are circumferentially non-uniform and act on the incoming flow to generate a non-axisymmetric flow downstream of a given blade row. As described in the next section, the momentum and energy source terms are determined as a function of local flow conditions, neglecting gradients in the circumferential direction, i.e., we assume the flow is *locally axisymmetric*. This assumption is appropriate if the characteristic length scale of the circumferential dis-

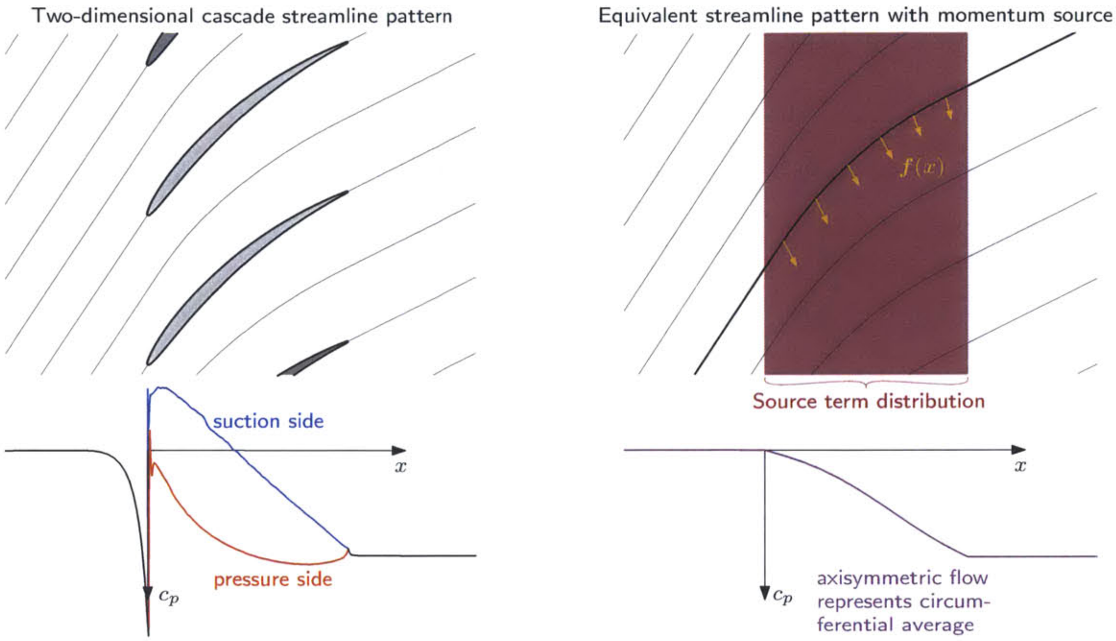

Figure 5-2: Comparison of two-dimensional cascade flow to equivalent model flow with source term distribution

tortion is much larger than the blade pitch, as is the case for ideal BLI inlet distortions with little streamwise vorticity. For example, the fan geometry considered in this chapter has 22 blades, yielding a ratio of pitch to distortion length scale (i.e., wheel circumference) of appoximately 0.05 for a once-per-revolution distortion at the fan tip section.

A related consequence of the long circumferential distortion length scale is that unsteadiness in the blade-relative frame can be neglected. The importance of unsteady effects is implied by the reduced frequency β, which relates the time scales of the flow unsteadiness and the passage throughflow. For the first harmonic of a once-per-revolution fan inlet distortion, β can be expressed in terms of flow coefficient ϕ and rotor geometry,

$$\beta = \frac{c_x/V_x}{2\pi/\Omega} \approx \frac{(\cos\xi)(1 - r_i/r_o)}{2\pi\phi AR}, \tag{5.1}$$

where ξ is the blade stagger, r_i/r_o is the blade hub-to-tip ratio, and AR is the blade aspect ratio. For the fan stage geometries examined in this thesis, $\beta < 0.1$. Comarison of solutions from a momentum and energy source distribution analysis and from full-wheel unsteady calculations has shown the distortion response to be well represented by a quasi-steady flow description [27].

5.1.2 Governing Equations

For steady, inviscid flow, the local momentum and energy source terms are represented in the equations of motion as a body force per unit mass $\boldsymbol{f}$ and an energy addition rate per unit mass $\dot{e}$,

$$\nabla \cdot (\rho \boldsymbol{V}) = 0, \tag{5.2}$$

$$\boldsymbol{V} \cdot \nabla \boldsymbol{V} + \frac{1}{\rho} \nabla p = \boldsymbol{f}, \tag{5.3}$$

$$\boldsymbol{V} \cdot \nabla h_t = \boldsymbol{V} \cdot \boldsymbol{f} + \dot{e}. \tag{5.4}$$

Equations (5.3) and (5.4) show that source terms contribute to local gradients in velocity, pressure, and stagnation enthalpy. Equations (5.2) and (5.3) are sufficient to fully describe an incompressible flow field, but we consider the general compressible case including Equation (5.4) to examine the relationship between the source terms and the thermodynamic quantities of stagnation enthalpy and entropy, which correspond to work done and losses within the flow, respectively.

Equations (5.3) and (5.4) can be combined with the differential form of the Gibbs equation,

$$T \nabla s = \nabla h - \frac{1}{\rho} \nabla p, \tag{5.5}$$

to show the relationship between the energy source, $\dot{e}$, and the local entropy gradient,

$$\dot{e} = T \boldsymbol{V} \cdot \nabla s. \tag{5.6}$$

Equation (5.6) is a general statement for flow described by Equations (5.2)-(5.4), and $\dot{e}$ can be considered as an entropy source associated with irreversible losses in adiabatic flow.

Stagnation enthalpy gradients are generated by the action of the blade force in rotating blade rows. The rothalpy, $I_t = h_t - (\Omega r)V_\theta$, is constant along a streamline (i.e., $\boldsymbol{V} \cdot \nabla I_t = 0$), so the stagnation enthalpy change is related to the change in circumferential velocity,

$$\boldsymbol{V} \cdot \nabla h_t = \Omega \boldsymbol{V} \cdot \nabla (r V_\theta). \tag{5.7}$$

For quasi-axisymmetric flow, changes in circulation rV_θ along a streamline can only be produced by a circumferential body force. The stagnation enthapy gradient is thus a function of the circumferential component f_θ of the momentum source term,

$$\boldsymbol{V} \cdot \nabla h_t = \boldsymbol{f} \cdot (\Omega r)\hat{\theta} = f_\theta(\Omega r). \tag{5.8}$$

Equation (5.8) can be thought of as the differential form of the Euler turbine equation for the model flow. The relationship between stagnation enthalpy and the momentum source is consistent with the view of $\boldsymbol{f}$ as a pitchwise distribution of the local blade force in that the work done by the blade, and the resulting increase in stagnation enthalpy, is equal to the dot product of the blade force and the blade velocity.

Equations (5.4), (5.6), and (5.8) can be combined to given an expression relating the relative velocity $\boldsymbol{W} = \boldsymbol{V} - (\Omega r)\hat{\theta}$, the momentum source $\boldsymbol{f}$, and the entropy source $\dot{e}$,

$$-\boldsymbol{W} \cdot \boldsymbol{f} = -W f_\ell = \dot{e} = T\boldsymbol{V} \cdot \nabla s. \tag{5.9}$$

Equations (5.8) and (5.9) show that it is useful to characterize the momentum source in terms of components parallel and normal to the relative flow direction. Entropy generation due to viscous losses is represented with a parallel force f_ℓ, acting opposite the direction of the flow, and an energy source $\dot{e}$, according to Equation (5.9). The component f_ℓ is normal to the relative flow direction and generates reversible flow turning.

5.2 Blade Camber Surface Loading Model

In the present formulation, the source term distribution is represented as a function of a specified three-dimensional blade camber surface geometry and the local flow conditions within the blade row. Decomposition of the momentum source distribution into flow-normal and flow-parallel components allows definition of separate blade loading and blade loss models. We have not included losses in the current description because the distortion interactions of interest occur near design are not strongly affected by blade row losses. Insteady, we use computed blade loading parameters (e.g., diffusion factor) as surrogates to provide estimates of efficiency variations resulting from distortion. The source representation, therefore, consists of a flow-normal momentum source distribution representing the local pressure difference across the blade.

The geometry of the blade camber surface, relative flow velocity, and momentum source

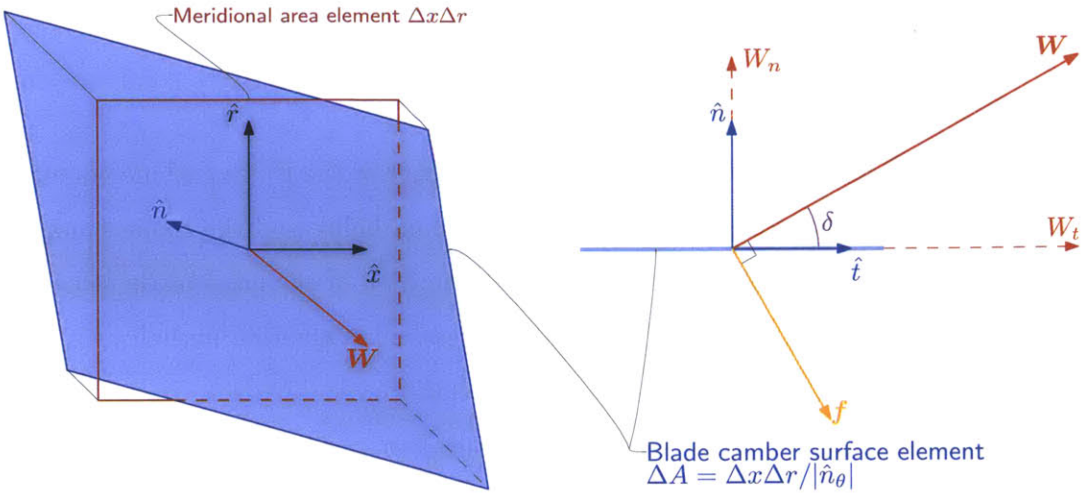

Figure 5-3: Geometric description of local blade camber surface, relative velocity, and resulting flow-normal momentum source; the blade camber surface normal $\hat{n}$, the relative velocity $\boldsymbol{W}$, and the momentum source $\boldsymbol{f}$ all lie on the common two-dimensional plane shown on the right

is shown in Figure 5-3. The camber surface geometry is characterized by a normal vector $\hat{n}(x, r)$. The velocity in the blade-relative frame $\boldsymbol{W}$ is decomposed into components normal and tangent to the blade surface, W_n and W_t, respectively. The momentum source $\boldsymbol{f}$ is constructed such that it acts to reduce the local deviation angle, δ, between the velocity vector and the camber surface. The momentum source acts normal to the flow in the $\hat{n}$-$\hat{t}$ plane, where $\hat{t}$ is the unit vector in the direction of the blade-tangent velocity W_t.

The magnitude of $\boldsymbol{f}$ is determined by equating the local momentum source to a blade loading force per unit mass, which scales with local deviation angle, dynamic pressure, and blade surface area, distributed over the local blade pitch s,*

$$|\boldsymbol{f}| = 2\pi \delta W^2 \frac{1}{s} \frac{1}{|\hat{n}_\theta|}. \tag{5.10}$$

The constant 2π in Equation (5.10) ensures the correct $c_\ell = 2\pi\delta$ behavior in the limiting case of a two-dimensional, isolated ($s/c \rightarrow \infty$), flat plate airfoil. In the other limit, as $s/c \rightarrow 0$, the flow is everywhere tangent ($\delta = 0$) to the blade camber surface.

The local momentum source vector is described by the expression for loading in Equation (5.10), the geometric orientation of the blade surface, the relative velocity, and the flow-

---

*This formulation is similar to the swirl evolution implemented in MTFLOW [37].

normal momentum source in Figure 5-3. The energy source $\dot{e}$ is zero in the present analysis, so there is no entropy generation within the blade rows. In the numerical solution, $\boldsymbol{f}$ is determined as a function of the local flow conditions, and both the flow field and the source distribution are calculated iteratively as the simulation converges to a solution that satisfies the equations of motion including the momentum source distribution.

5.3 Assessment of the Source Distribution Representation

In this section, we demonstrate the capabilities of the source distribution representation for several turbomachinery test flows. For axisymmetric flow, we show there is good agreement with higher-fidelity solutions for cascade and fan geometries. For nonaxisymmetric flow the three-dimensional flow redistribution observed in full-wheel unsteady distortion response calculations is shown to be captured [5].

5.3.1 Two-Dimensional Cascades with Uniform Inlet Conditions

For a two-dimensional cascade with uniform inlet conditions, the equations of motion for the equivalent source distribution flow with reduces to a system of one-dimensional ordinary differential equations. These can be numerically integrated for a given geometry to yield the axial distribution of pitchwise-average flow through the stage. The accuracy of the source distribution analysis is assessed by comparing the results with two-dimensional flow using the MISES cascade solver [38].

Figure 5-4 shows calculated blade loadings, in terms of static pressure rise normalized by inlet dynamic pressure $\Delta p/q$, over a range of incidence angles for geometries representing various fan stage sections.[†] The curves show the results of the source term analysis, and the symbols show the results from MISES solutions. There is good agreement between the source term model analysis and the MISES computations. The discrepancies between the two methods are largest for the rotor hub geometry, where solidity is largest and the source term analysis underestimates the deviation, leading to increased $\Delta p/q$. More importantly, however, the model captures the correct behavior in blade loading with changes in incidence angle for representative fan stage camberline geometries.

[†] The cascade geometries were designed in MISES to produce stagnation enthalpy rise and flow coefficients representative of rotor and stator sections for a fan similar to the R4 fan considered in the next section.

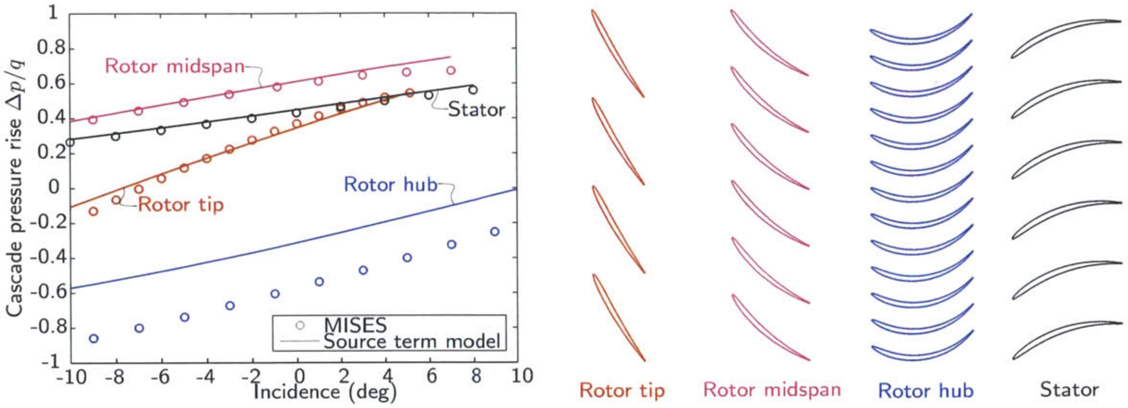

Figure 5-4: Calculated cascade static pressure rise vs incidence for geometries representative of fan stage rotor and stator blade sections, MISES versus source term analysis

5.3.2 NASA R4 Fan Stage

To assesssf the source term analysis in three-dimensional flow, we examine the NASA R4 fan stage. This fan was chosen because its design pressure ratio (1.47) and hub-to-tip ratio (0.3) are representative of contemporary fan stages, and its performance is available in the open literature [39]. The performance has also been successfully analyzed using a source distribution representation similar to that considered here [26]. Comparison of the axisymmetric form of the analysis with single passage RANS calculations provides an assessment of the analysis for radially varying geometries. Examination of the behavior with inlet distortion gives evidence that the analysis captures the relevant flow redistribution and distortion transfer.

Figure 5-5 shows the meridional flowpath geometry used of the R4. The stagnation pressure distribution is specified at an inlet boundary one fan diameter upstream of the stage. A constant radius slip-wall casing is used between the inlet location and the fan casing inlet location. Within the swept volume of the rotor and stator, there area source distributions based on the blade camber surface. Rotor and stator inlet and exit planes for flow field and blade row performance assessment are defined at axial locations one quarter rotor chord from the leading and trailing edges of both blade rows.

Fan Rotor Throughflow with Uniform Inlet Conditions

Results are shown for uniform inlet flow and a rotor-only geometry at 50% design speed, where the flow is subsonic. The flow with source distributions was calculated on a 1.3

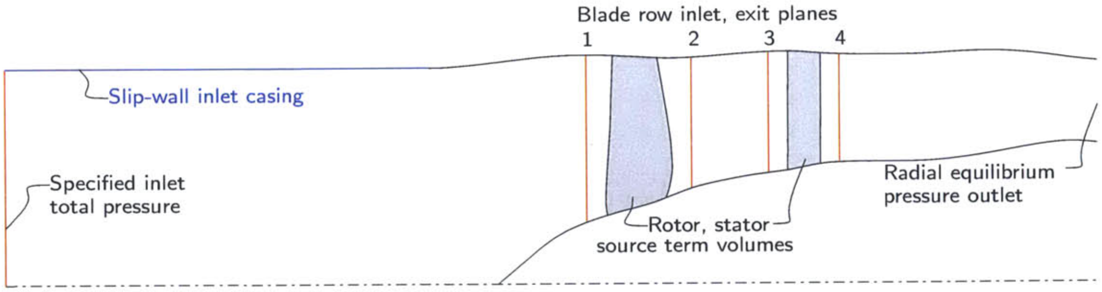

Figure 5-5: NASA R4 fan stage meridional flow path geometry and boundary conditions

million node three-dimensional axisymmetric grid with a circumferential extent of 90°, and the single passage flow was calculated on a two million node grid. Both flows were computed using the ANSYS CFX steady RANS solver with shear stress transport turbulence model with extended wall functions and $y+ < 10$.[‡]

Figure 5-6 shows calculated fan stage stagnation enthalpy rise coefficient versus flow coefficient for the single passage and source distribution solutions. The source term analysis overpredicts the stagnation pressure rise because no losses are included, but the behavior in flow turning and enthalpy rise is well captured. The enthalpy rise coefficient given by the analysis matches the blade passage calculations within 2% over the operating range of the fan for which the performance has been measured experimentally [39].

Radial distributions of pitchwise-averaged axial velocity and stagnation enthalpy rise are shown in Figure 5-7. The overall shape of the design point radial loading distribution matches the RANS-computed enthalpy rise within 10% over most of the blade span. Near the end walls, the model cannot capture the quantitative effect of tip clearance and pitchwise variations in the endwall boundary layer on the pitchwise average stagnation enthalpy rise and flow coefficients, but these discrepancies do not have a large impact on the overall performance.

Three-Dimensional Fan Stage Distortion Response

The distortion response was assessed for a vertically stratified inlet stagnation pressure distribution representing an upstream fuselage boundary layer, as shown in Figure 5-8. The

---

[‡] The source term description was derived for inviscid flow. Implementing the flow model in a viscous solver will also produce changes in enthalpy and entropy in the main flow, but the endwall boundary layers are resolved by the equations of motion.

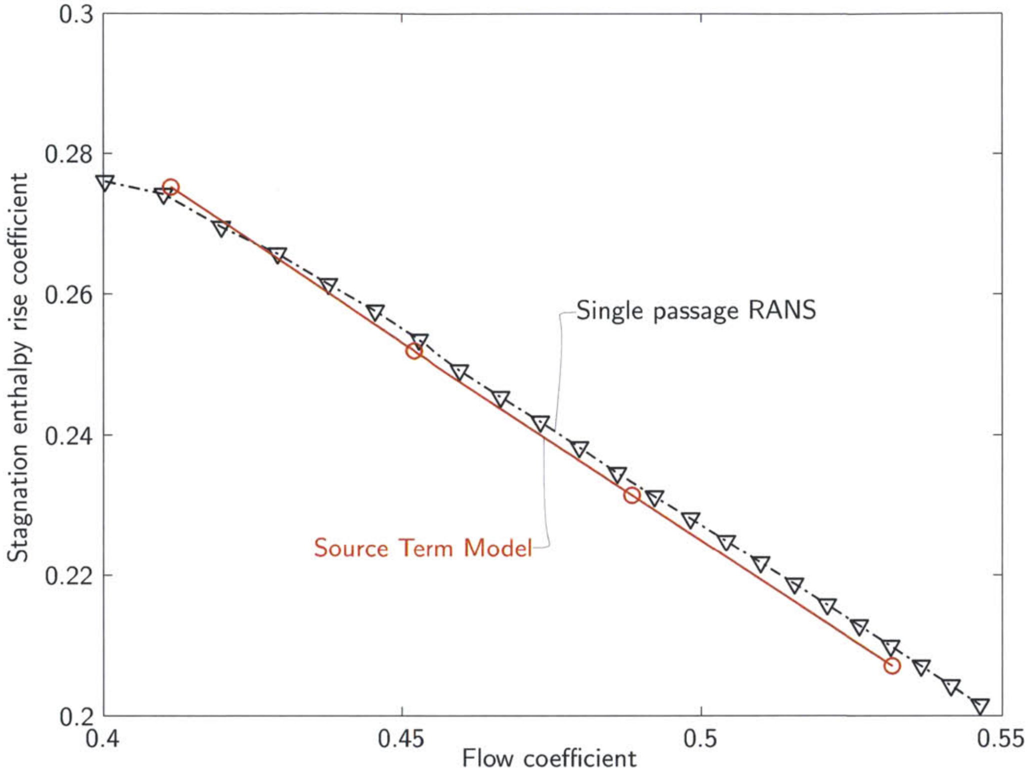

Figure 5-6: NASA R4 rotor stagnation enthalpy rise characteristic; RANS computations vs axisymmetric source term model with uniform inlet conditions

domain inlet stagnation pressure is calculated from a cubic-spline velocity distribution with non-zero wall velocity to provide a realistic boundary layer shape factor. The plot on the left of Figure 5-8 shows contours of non-dimensional stagnation pressure imposed at the domain inlet (station 0 in Figure 5-5). The plot on the right shows a comparison of the vertical stagnation pressure with a computed BLI inlet profile. The vertical axis is height above the bottom of the fan, and the horizontal axis is non-dimensional stagnation pressure.

Figures 5-9 through 5-18 show various flow quantities at different axial stations as contours on axial planes (oriented with $\theta = 0$ at the top of the wheel, θ increasing counter-clockwise, and clockwise rotor rotation) and as circumferential distributions near the blade hub, midspan, and tip sections. The former is useful for qualitative assessment of the flow behavior, and the latter allows quantitative assessment of various flow metrics.

Figure 5-9 shows the non-dimensional stagnation pressure distribution at the rotor inlet.

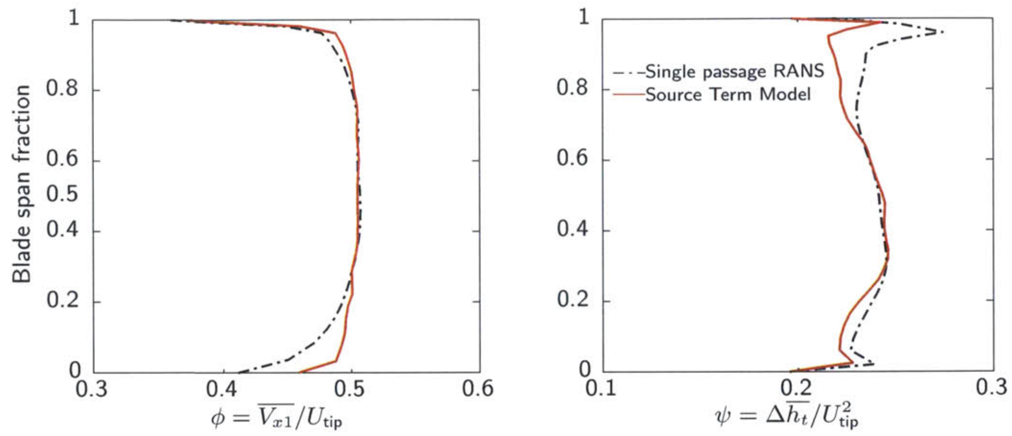

Figure 5-7: NASA R4 rotor radial stagnation enthalpy rise distribution; RANS computations vs axisymmetric source term model

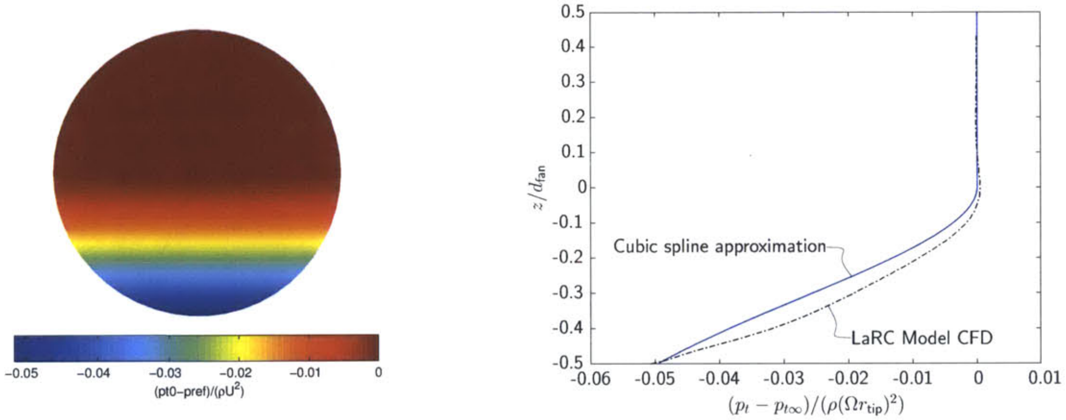

Figure 5-8: BLI inlet stagnation pressure distribution

The inlet distortion convects along streamlines from inlet to the fan face. Upstream interaction of the non-uniform flow with the fan stage produces a top-to-bottom flow redistribution. The rotor-relative flow angle distortion is shown in Figure 5-10. The top-to-bottom velocity at the rotor inlet yields regions of co-swirl and reduced incidence on the right-hand side ($\theta > 180°$) of the fan, and counter-swirl and increased incidence on the left-hand side ($\theta < 180°$). The effect is strongest near the hub, where the blade speed is lowest and the swirl velocities are large due to the blockage of the spinner. Near the bottom of the wheel ($\theta = 180°$), there is increased incidence due to reduced axial velocity in the low stagnation pressure region. The incidence angle distortion is largest near the hub, where the stagnation pressure distortion is smallest. This is due to the upstream flow redistribution, because the velocity distortion at all spanwise locations are affected by the stagnation pressure distor-

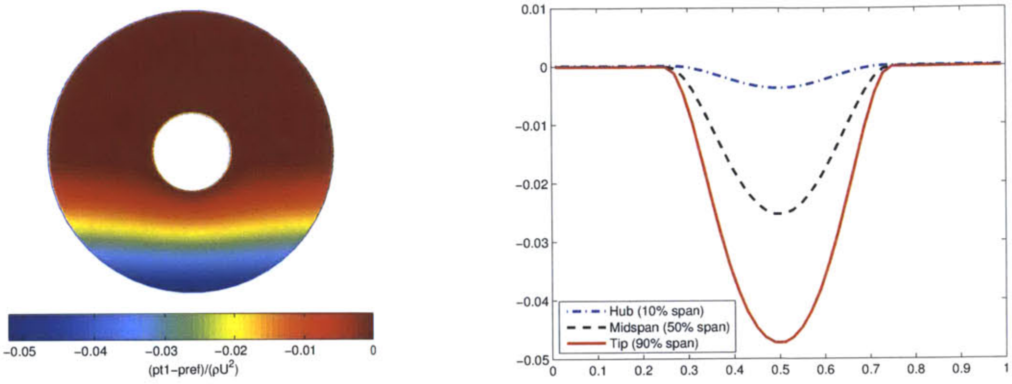

Figure 5-9: Rotor inlet non-dimensional stagnation pressure $(p_{t1} - p_{t\infty})/(\rho(\Omega r_{\text{tip}})^2)$

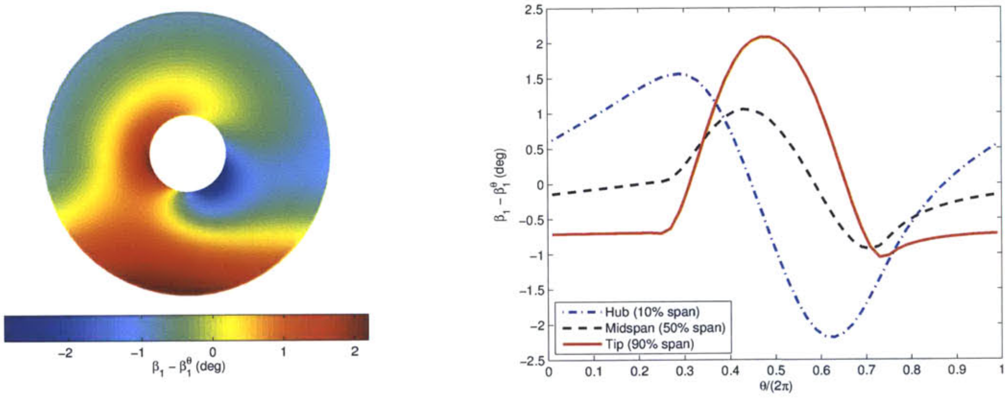

Figure 5-10: Rotor incidence angle distortion $\beta_1 - \overline{\beta}_1^{\theta}$

tion near the tip. The two-dimensional analysis in Chapter 4 cannot capture this type of upstream flow redistribution.

Figure 5-11 shows the stagnation enthalpy rise coefficient across the rotor. At $\theta = 0$, the upstream stagnation pressure is uniform, the upstream redistribution produces no circumferential velocities, and the enthalpy rise distribution is similar to that for uniform flow in Figure 5-7 (this is also seen in the differences in the circumferential averages shown as dotted lines in the right-hand plot of Figure 5-11). The circumferential variations in enthalpy rise correspond to the changes in incidence: increased incidence leads to increased stagnation enthalpy rise, relative to the circumferential average, and decreased incidence leads to decreased stagnation enthalpy rise. This behavior is qualitatively similar to the behavior of the rotor actuator disk in Chapter 4. The local flow turning and stagnation enthalpy rise are set by the inlet relative flow angle, β_1, and the exit flow angle, β_2, which

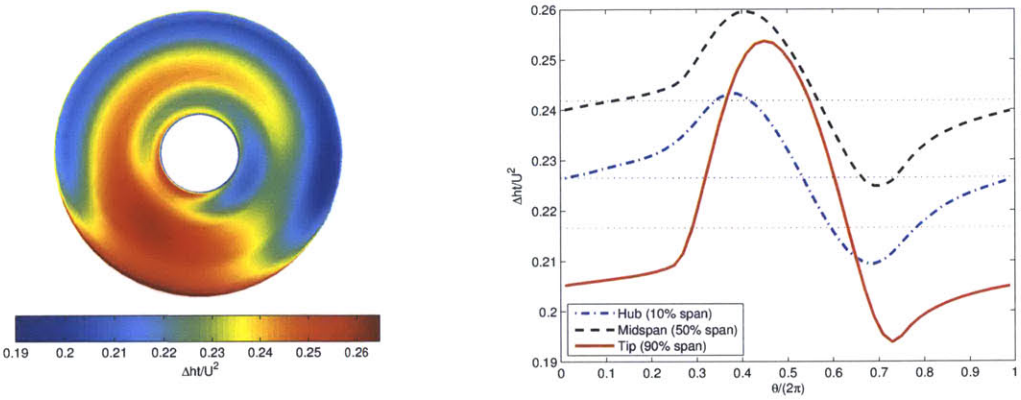

Figure 5-11: Rotor stagnation enthalpy rise coefficient $\psi = \Delta h_t / (\Omega r_{\text{tip}})^2$

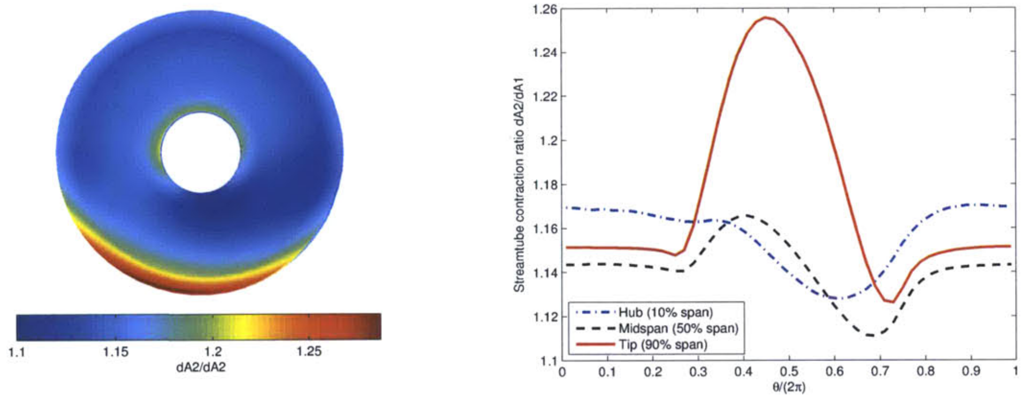

Figure 5-12: Rotor streamtube area contraction ratio $(\rho_2 u_2)/(\rho_1 u_1)$

is constrainted by the blade geometry.

The non-uniform work input results in non-uniformities in streamtube contraction. Figure 5-12 shows local streamtube contraction through the rotor, $\delta A_1/\delta A_2 = (\rho_2 u_2)/(\rho_1 u_1)$. The contraction ratio distributions are qualitatvely similar to the local work input, and the magnitude of the circumferential non-uniformities are largest where the stagnation pressure distortion is largest.

The combination of flow turning and streamtube contraction yields non-uniform relative velocity decelerations across the blade, which we use as a surrogate for blade performance in the absence of losses in the throughflow analysis. Figure 5-13 shows circumferential distortions in the relative rotor velocity ratio W_1/W_2. As with incidence angle, the velocity ratio distortion is largest near the hub. At midspan, there are two peaks in the velocity ratio circumferential distribution, one due to increased incidence and turning in the counter-swirl

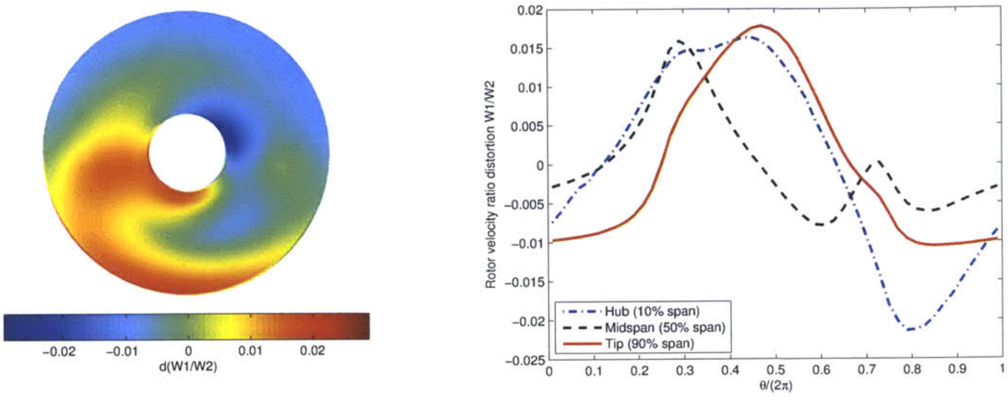

Figure 5-13: Rotor velocity ratio distortion $W_1/W_2 - \overline{(W_1/W_2)}^\theta$

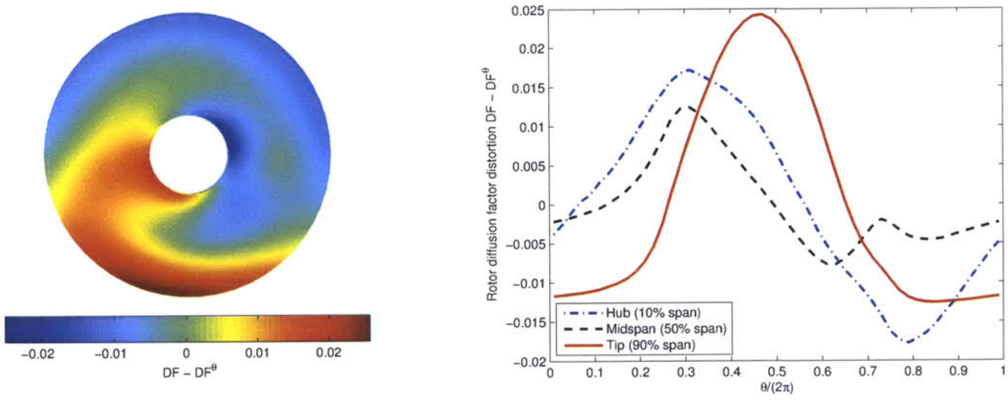

Figure 5-14: Rotor diffusion factor distortion $\mathrm{DF} - \overline{\mathrm{DF}}^\theta$

region, and one due to decreased streamtube area contraction in the co-swirl region. Figure 5-14 shows circumferential distortions in rotor diffusion factor,

$$\mathrm{DF} = 1 - \frac{W_{\mathrm{out}}}{W_{\mathrm{inl}}} + \frac{\Delta V_\theta}{2\sigma W_{\mathrm{inl}}}. \tag{5.11}$$

The solidity $\sigma = c/s$ is approximated using the local blade pitch, $s = 2\pi r/B$, and the midspan chord (the only chord value provided in the literature [39]). Both the velocity ratio and diffusion factor provide a measure of flow deceleration; the former represents the pitchwise-average, and the latter estimates deceleration in the blade boundary layers based on approximations about the streamwise blade loading distribution. Previous full-wheel unsteady calculations have shown that changes in diffusion factor are a good predictor of changes in local efficiency relative to the performance with uniform inlet conditions [5].

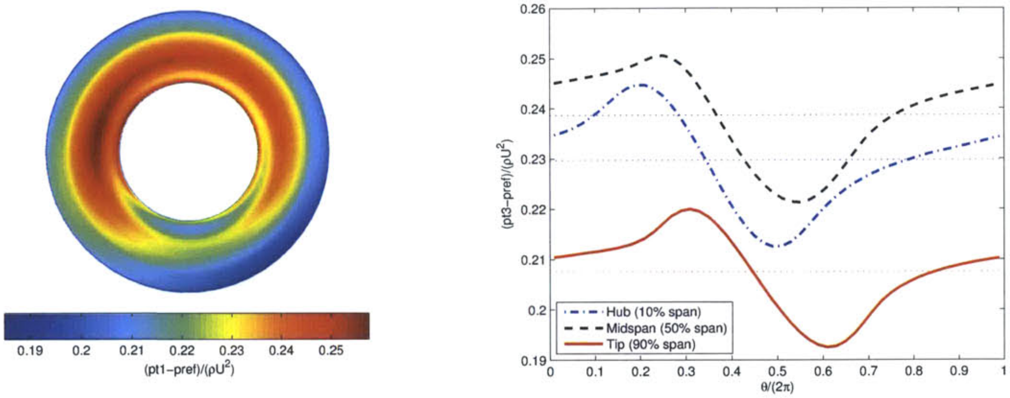

Figure 5-15: Stator inlet non-dimensional stagnation pressure $(p_{t3} - p_{t\infty})/(\rho(\Omega r_{\text{tip}})^2)$

Comparison of Figures 5-13 and 5-14 shows both metrics exhibit qualitatively similar circumferential distributions, and thus either may be used as a surrogate for blade section performance in evaluating the effect of changes in fan stage design on distortion response.

Figure 5-15 shows the non-dimensional stagnation pressure distribution at the stator inlet. The stator inlet stagnation pressure is set by the rotor inlet stagnation pressure distribution upstream of the rotor and the non-uniform work input by the rotor. The distribution in Figure 5-15 is thus arrived at by adding the values in Figure 5-9 and 5-11. Near the tip, the work input is highest where the stagnation pressure is lowest, in agreement with parallel compressor theory, and results in a reduction in the magnitude of the circumferential stagnation pressure non-uniformity from $0.05\rho(\Omega r_{\text{tip}})$ upstream of the rotor to $0.03\rho(\Omega r_{\text{tip}})$ upstream of the stator. At other spanwise locations, however, the non-uniformities in stagnation enthalpy do not necessarily result in a reduction in stagnation pressure distortion. At midspan, the magnitude of the circumferential stagnation pressure uniformity is approximately $0.25\rho(\Omega r_{\text{tip}})^2$ both upstream and downstream of the rotor, and near the hub, it increases from less than $0.005\rho(\Omega r_{\text{tip}})^2$ to approximately $0.025\rho(\Omega r_{\text{tip}})^2$. These non-uniformities do not necessarily have an adverse effect on the fan stage efficiencies, but they will result in a decrease in propulsive efficiency for a given propulsive power.

Figure 5-16 shows stator incidence distortion. As described in Chapter 4 for a close-spaced stator, non-uniformities in absolute tangential velocity and swirl angle will exhibit the same behavior as the axial velocity. This behavior is apparent in Figure 5-16, where the stator incidence is highest near the bottom of the wheel, where the axial velocity is lowest, highest near the top of the wheel, where the axial velocity is highest, and increases

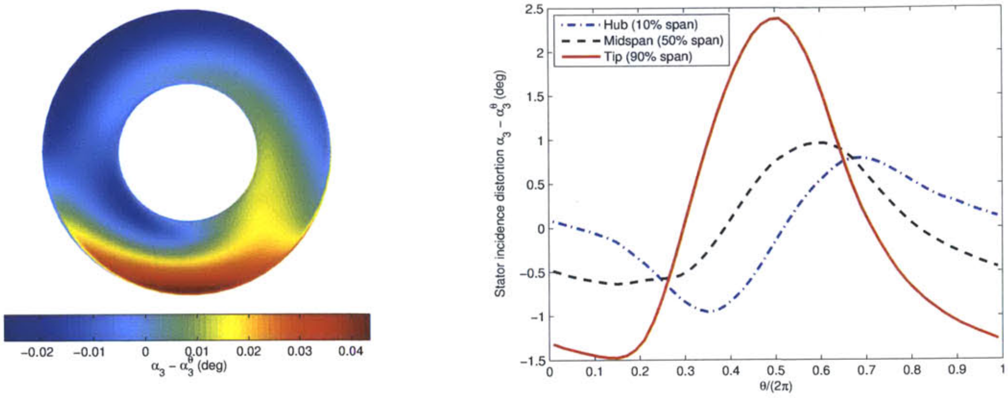

Figure 5-16: Stator incidence angle distortion $\alpha_3 - \overline{\alpha_3}^{\theta}$

in regions of increased rotor streamtube area contraction (Figure 5-12).

As in the rotor, we consider circumferential distortions in velocity deceleration across the stator as a surrogate for local blade row performance. Figures 5-17 and 5-18 show circumferential distortions in stator velocity ratio, V_3/V_4, diffusion factor, respectively. Again the two metrics exhibit qualitatively similar behavior at a given spanwise location, making either an appropriate surrogate for blade section performance.

5.4 Summary

An analysis has been developed to calculate non-axisymmetric turbomachinery throughflow using distributed momentum and energy sources. The analysis applies to circumferential length-scale distortions large compared to blade pitch, such as those seen with BLI, in which the flow can be assumed locally quasi-axisymmetric and quasi-steady. The solutions represent the relevant long length-scale features in a pitchwise-averaged sense. This approximation means solutions can be obtained at much lower cost than typical distortion response calculations using the full blading geometry due to reduced grid size (the full-wheel simulated with a grid similar in size to a single blade passage grid) and the use of steady rather than unsteady solution techniques. Further, the current method requires no a priori blade passage flow solutions.

The source term distributions are determined as a function of local flow conditions for a specified blade camber surface geometry, which turns the blade-relative flow towards the blade-tangent direction. Because blade losses do not have a significant impact on the

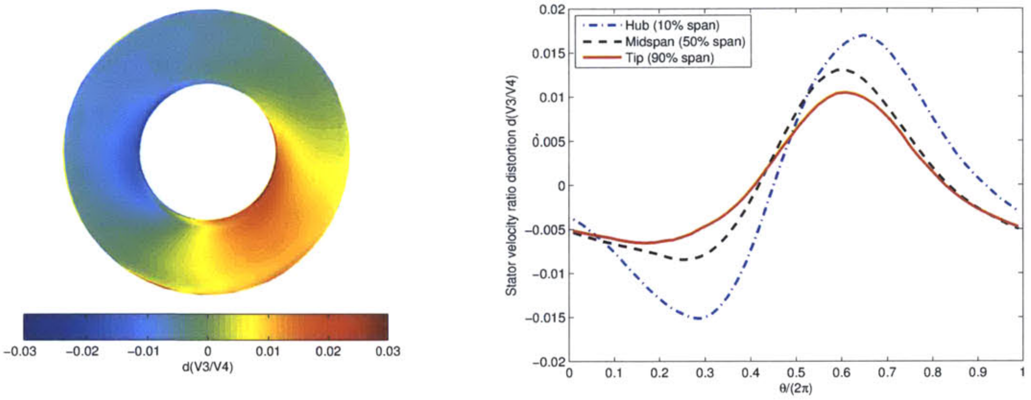

Figure 5-17: Stator velocity ratio distortion $V_3/V_4 - \overline{(V_3/V_4)}^\theta$

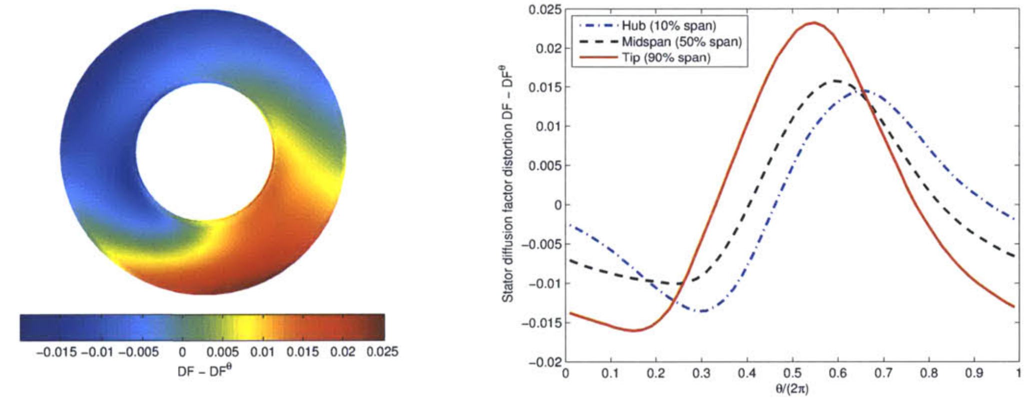

Figure 5-18: Stator diffusion factor distortion $\mathrm{DF} - \overline{\mathrm{DF}}^\theta$

distortion response features of interest, an inviscid description is used.

Comparison with bladed passage calculations for two-dimensional cascades shows that changes in flow turning and pressure rise with blade row inlet angle are well described for geometries representative of fan stage blading. Comparison with single passage RANS calculations for a three-dimensional fan rotor with uniform inlet conditions shows the approximate analysis is able to capture the stagnation enthalpy rise characteristic and radial loading distribution.

Application to a fan stage with BLI inlet distortion illustrates the analysis capture distortion flow mechanisms observed by previous authors [5]. Fan-distortion interaction leads to a top-to-bottom redistribution of the flow upstream of the fan, which generates tangential velocity non-uniformities at all spanwise locations, an effect that is not predicted by the circumferential distortion analysis in Chapter 4. Downstream of the rotor inlet, however, the rotor work input and stator inlet agree qualitatively with two-dimensional analysis. Examination of circumferential non-uniformities in relative velocity ratio and diffusion factor both show behavior in agreement with previous work, and both are thus deemed appropriate surrogates for local blade row performance in assessment of the effect of changes in fan stage design on distortion response.

Chapter 6

Distortion Tolerant Propulsor Design Attributes

In this chapter, we use the analysis described in Chapter 5 to deteremine non-axisymmetric flow fields for a number of fan stage geometries, identifing design attributes to mitigate the effect of BLI inlet distortion on fan efficiency. The impacts of: (i) stage design point, (ii) radial loading distribution, (iii) rotor-stator axial spacing, and (iv) non-axisymmetric stator exit angle distributions are examined. For axisymmetric stage design, the results illustrate the tradeoffs in performance between the rotor and stator or between different spanwise sections of a given blade row. For non-axisymmetric designs, it is found that a circumferentially varying stator geometry can be used to reduce the rotor velocity distortions and potentially mitigate both rotor and stator losses.

6.1 Parametric Geometry Description

Calculations have been carried out for the axisymmetric geometry in Figure 6-1. The meridional flowpath upstream of the rotor is the same as the R4 fan. Downstream of the rotor inlet, the casing radius is constant, and the hub radius yields a constant area contraction rate, dA/dx, through the stage and downstream nozzle.

Momentum and energy source distributions are applied in annular volumes of constant axial extent, at the rotor and stator locations, with a specified blade camber surface geometry. The focus here is on rotor loading and stator exit swirl distributions that the geometry produces. Solidity is thus not considered as a design variable, and the blade and vane counts

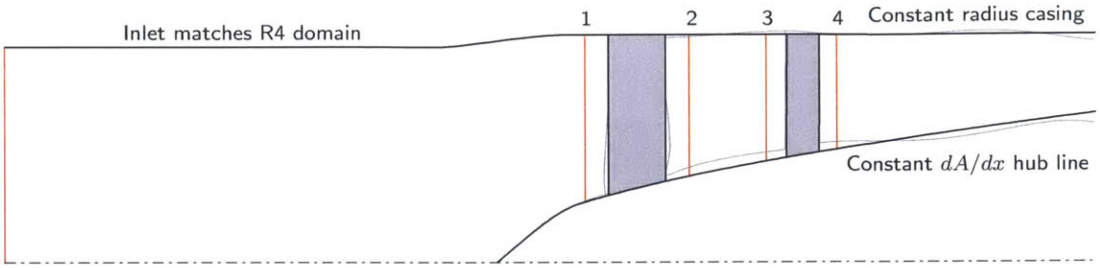

Figure 6-1: Fan stage meridional geometry for inlet distortion response parametric design study calculations

are set at those of the R4 fan stage (22 and 54, respectively). For each design, the rotor blade camber surface geometry is parametrically defined as a function of the specified radial distribution of leading edge and trailing edge metal angles. The stator loading is set by the overall *turning*, and thus for convenience, the stator vanes are simulated as flat plates (zero camber) at either zero stagger or with a specified non-axisymmetric stagger distribution.

The relevant distortion flow mechanisms identified in Chapters 4 and 5 are effectively inviscid, and the flow is thus taken to be inviscid.* Solutions were computed on an axisymmetric full-annulus grid of approximately one million cells using the inlet stagnation pressure distribution described in Section 5.3.2.

6.2 Fan Stage Design Assessment

Following the conceptual approach of Chapter 4, we consider the effect of variations in turbomachinery design point velocity triangles, axial spacing between the rotor and stator, and non-axisymmetric stator geometries. The performance metric is circumferential non-uniformity in the relative velocity ratios across the rotor and stator, W_1/W_2 and V_3/V_4, respectively. This captures the effect of changes in both incidence and local streamtube contraction on local streamtube deceleration, and is used as an indicator of changes in efficiency. Diffusion factor captures the same effects, and has been shown to correlate well with changes in local efficiency [5], but it depends on local blade section solidity, which is not part of the parametric description considered here. It can be noted, however, that

---

*The analysis is implemented computationally using ANSYS CFX, which only has the capability to solve the Navier-Stokes equations. Inviscid flow is approximated by solving for laminar flow with free-slip end walls.

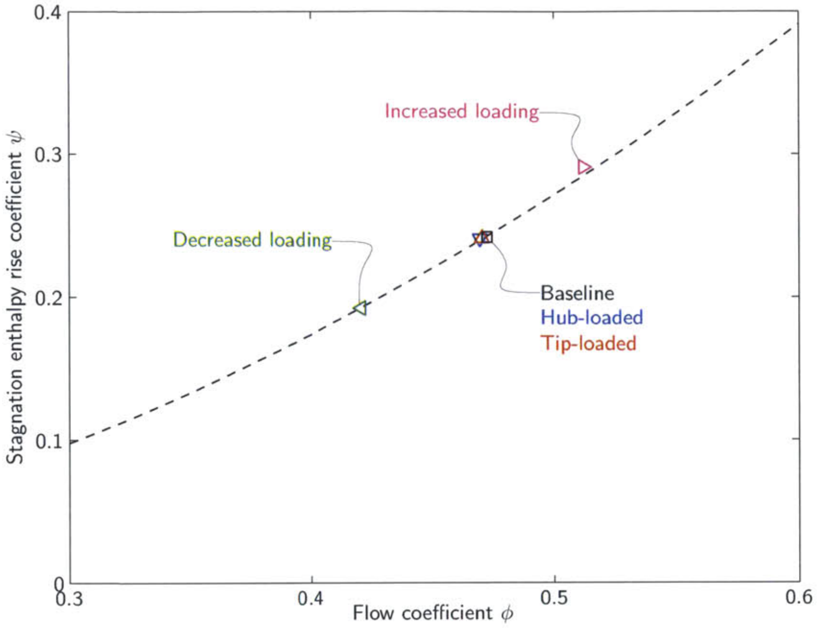

Figure 6-2: Design point enthalpy rise and flow coefficient; all point have the same design point ψ/ϕ^2 (thrust requirement), three designs have different radial loading distributions at constant overall ϕ and ψ.

Chapter 5 showed the behavior of velocity ratio and diffusion factor non-uniformities are similar, and the results would not be expected to change between these two metrics.

The distortion flow behavior, e.g., circumferential distributions of perturbations velocities and flow angles, is qualitatively similar for the range of cases examine. We thus consider the *magnitude* of velocity ratio distortion as our performance metric,

$$\delta\left(\frac{W_{\text{inl}}}{W_{\text{out}}}\right) = \max\left(\frac{W_{\text{inl}}}{W_{\text{out}}}\right) - \min\left(\frac{W_{\text{inl}}}{W_{\text{out}}}\right). \tag{6.1}$$

In the analysis of axisymmetric stage geometries, we examine rotor and stator $\delta(W_{\text{inl}}/W_{\text{out}})$ at radial locations near the hub (10% span), midspan (50% span) and tip (90% span).

6.2.1 Stage Design Point and Radial Loading Distribution

Five different rotor geometries are examined to assess the impact of design point velocity triangles. Figure 6-2 shows the design point stagnation enthalpy rise coefficient versus flow coefficient, and Figure 6-3 shows radial stagnation enthalpy rise distribution for all five geometries. The rotor camber surface geometries were generated by fixing the leading

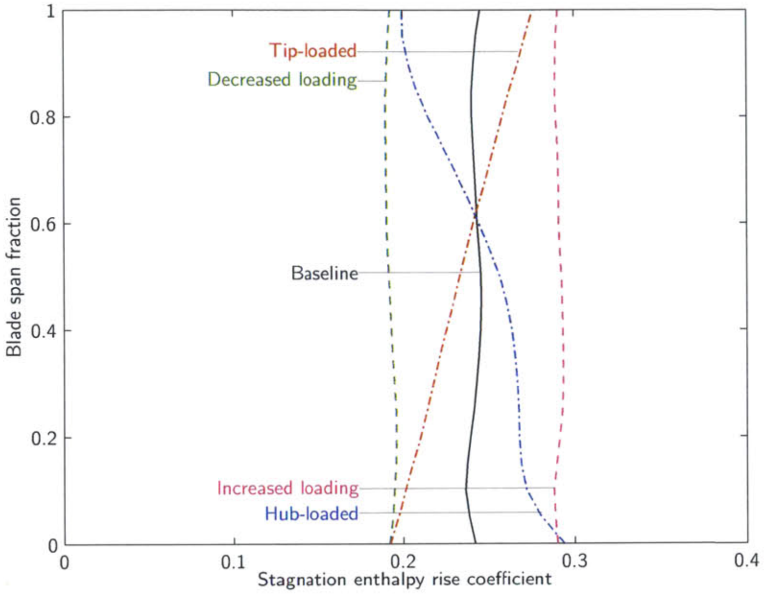

Figure 6-3: Design point radial stagnation enthalpy rise distributions; the geometries with different overall design point (ϕ, ψ) have approximately uniform loading distributions.

edge metal angle distribution based on the design point flow coefficient and varying the trailing edge metal angle distribution iteratively until the desired stagnation enthalpy rise distribution was achieved. The baseline geometry has the same design point as the R4 fan with an approximately uniform radial distribution in stagnation enthalpy rise. Two geometries have the same ψ/ϕ^2 (representing a fixed propulsive power requirement) with $\pm 20\%$ change in stagnation enthalpy rise relative to the baseline case, and two designs have radially non-uniform stagnation enthalpy rise distributions at the baseline stage (ϕ, ψ) design point.

Figure 6-4 shows the magnitude of distortions in swirl angle in the absolute frame at the rotor inlet, $\delta\alpha_1$. The results show the behavior of the upstream redistribution with changes in the stage design point is qualitatively similar to observations from two-dimensional analysis. As the loading is increased, the slope of the pressure rise characteristic decreases, leading to reduced axial velocity attenuation, swirl generation, and flow angle distortions. This effect is not sensitive to the variations in radial loading distributions examined here; the changes in flow angle distortion for local changes in stagnation enthalpy rise at fixed (ϕ, ψ) are small ($< 0.5^\circ$) compared to similar changes along the entire span ($\sim 2^\circ$).

Figure 6-5 shows the behavior of rotor and stator velocity ratio distortions for changes in the stage design point with uniform loading distribution. The tip section behavior

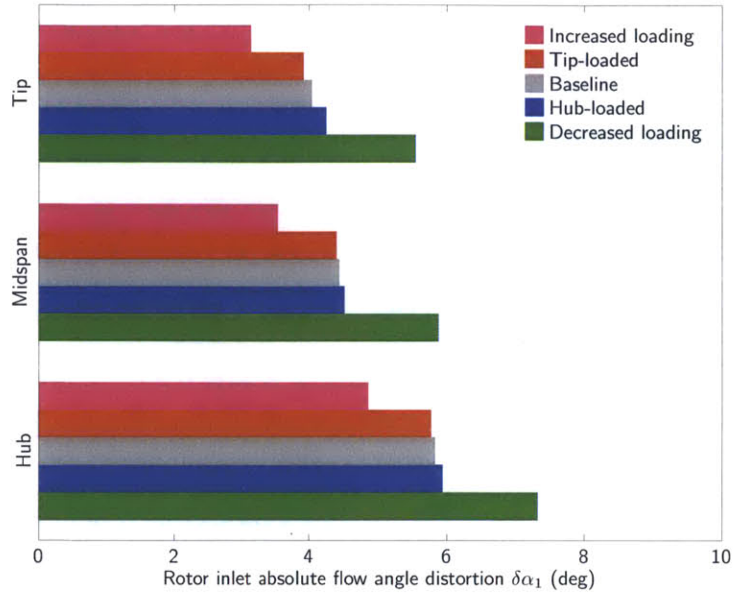

Figure 6-4: Changes in rotor inlet absolute swirl angle with changes in stage design point and radial loading distribution; increases in overall stagnation enthalpy rise lead to decreased characteristic slope, weaker upstream redistribution, and reduced incoming swirl.

is similar to the two-dimensional description in Chapter 4, with increasing distortion for increasing loading at fixed ψ/ϕ^2. Near the hub and midspan, however, the velocity ratio distortions are dominated by co- and counter-swirl distortions, which decrease for increasing loading. This effect is strongest near midspan due to the combination of swirl and axial velocity distortions, which increases the peak-to-peak velocity ratio distortion by a factor of two between the high and low loading designs. The stator behavior is consistent with the two-dimensional analysis, with decreasing stator distortion for increased loading at all radial locations.

Figure 6-6 shows the behavior of rotor and stator velocity ratio distortions for changes in the radial distribution of stagnation enthalpy rise coefficient. For fixed overall stage ϕ and ψ, the upstream flow is unchanged with changes in the radial loading distribution, as shown in Figure 6-4. Changes in the local stagnation loading distribution thus result in changes in the flow turning and rotor relative exit angle for fixed rotor inlet conditions, and the behavior of velocity ratio distortion can be explained in terms of changes in the local velocity triangles. As loading is increased, the rotor flow turning and velocity ratio distortion increase, and the stator velocity ratio distortion decreases, consistent with two-dimensional analysis.

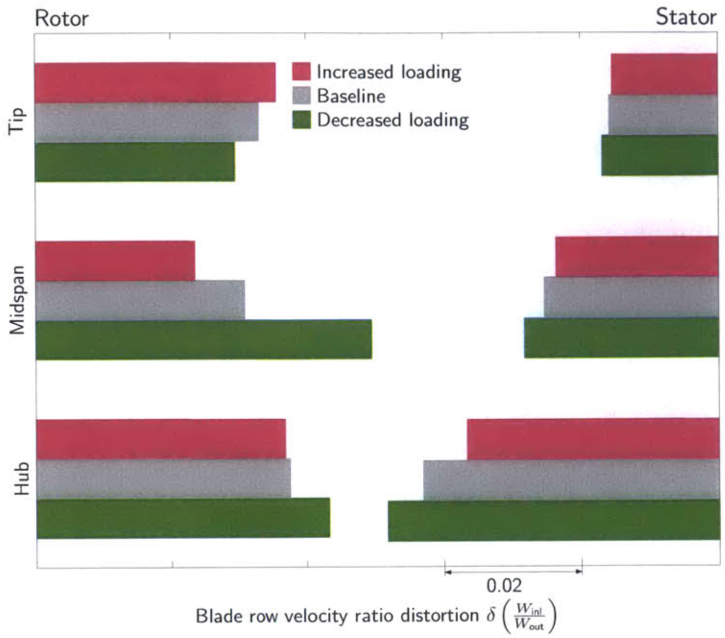

Figure 6-5: Changes in rotor and stator velocity ratio distortion with changes in stage design point; rotor hub and midspan distortions dominated by incoming swirl distortion, which increases with decrease loading; rotor tip section and stator sections behave in accord with two-dimensional analysis.

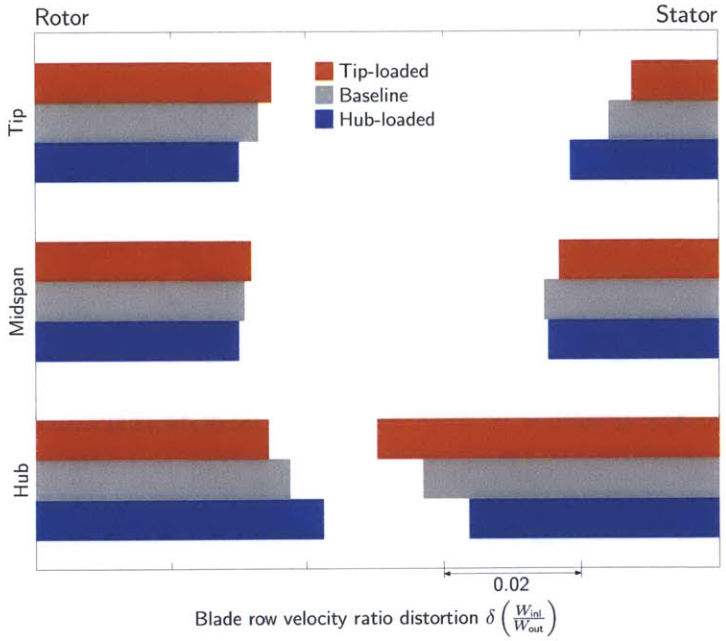

Figure 6-6: Changes in rotor and stator velocity ratio distortion with changes in radial loading distribution; behavior is similar to two-dimensional analysis because the upstream redistribution is insensitive to changes in the radial loading distribution at fixed ϕ and ψ.

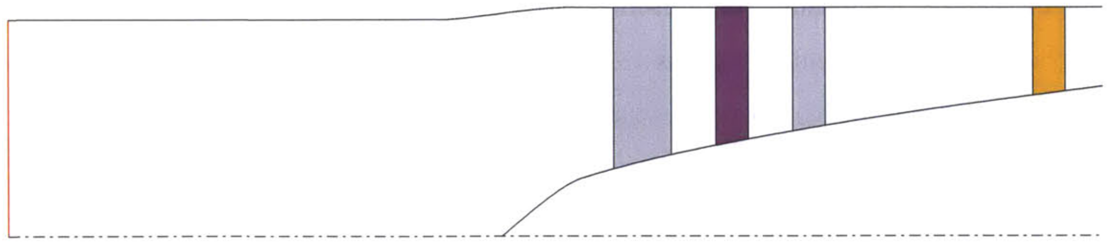

Figure 6-7: Fan stage meridional geometry with closely spaced, baseline, and far downstream stator locations

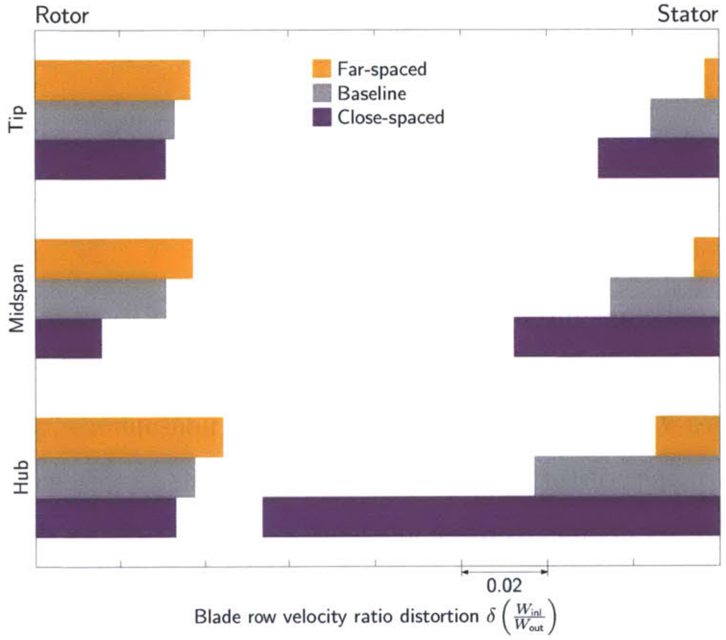

Figure 6-8: Changes in rotor and stator velocity ratio distortion with changes in rotor-stator axial spacing; behavior is similar to two-dimensional analysis.

6.2.2 Rotor-Stator Interaction

The effect of rotor-stator spacing was assessed for the baseline stage geometry ($\phi = 0.47$, $\psi = 0.24$, uniform radial distribution of stagnation enthalpy rise) for the three stator locations illustrated in Figure 6-7. The rotor-stator spacings are equal to 0.08, 0.25, and 0.76 fan diameters, all within the range of spacings considered in Chapter 4 ($L_{\text{R-S}} < 3$).

Figure 6-8 shows the magnitude of the velocity ratio non-uniformity with inlet distortion at rotor and stator hub, midspan, and tip sections, for the three stator locations. The results are consistent with observations from the two-dimensional analysis, with increased rotor-stator spacing decreasing the non-uniformity in the stator by as much as an order of magnitude and increasing the non-uniformity in the rotor by a factor of two. In this case, the stator performance benefits from the increased area contraction with increased rotor-stator spacing, which attenuates the axial velocity distortion upstream of the stator.

6.2.3 Non-Axisymmetric Stator Geometry

In this section, we examine the impact of non-axisymmetric stator design (downstream flow angle non-uniformity) on rotor performance. We consider circumferentially varying stator stagger angles ξ,

$$\xi = \cos^{-1}\hat{n}_\theta = -\sin^{-1}\hat{n}_x = \delta\alpha_4\cos(\theta - \theta_{\alpha_4}). \tag{6.2}$$

The assumption is that the detailed stator camber surface geometry does not influence the conditions at the rotor for a given downstream flow angle.

Figure 6-9 shows the magnitude of rotor incidence and velocity ratio non-uniformity for the baseline axisymmetric design and for non-axisymmetric stator geometries with different stagger phase angles θ_{α_4}. The results are for a stagger non-uniformity $\delta\alpha_4 = 10°$, which minimized rotor incidence distortion for a two-dimensional flow representing the tip section geometry. There are reductions in rotor incidence non-uniformity in the tip and midspan sections for $\theta_{\alpha_4} = 270°$ and the hub section for $\theta_{\alpha_4} = 180°$. For all the non-axisymmetric stator geometries, however, the rotor velocity ratio non-uniformity is amplified relative to the behavior with axisymmetric geometry.

Figure 6-10 shows circumferential distributions of rotor velocity ratio non-uniformity for different stator geometries. The tip velocity distortion for $\delta\alpha_4 = 10°$ and $\theta_{\alpha_4} = 270°$ is out of phase with that for the axisymmetric geometry, indicating the downstream static pressure perturbation is the dominant effect driving non-uniformities at the rotor. For $\delta\alpha_4 = 3°$ at the same stagger phase angle (and a smaller static pressure perturbation), there are more favorable conditions at the rotor, with a 39% reduction in velocity ratio non-uniformity. A similar result is obtained at the hub section; for a stator stagger phase angle $\theta_{\alpha_4} = 180°$ at $\delta\alpha_4 = 10°$, there is a 282% increase in velocity ratio distortion, but the same phase angle $\delta\alpha_4 = 1.5°$ results in a 48% decrease in velocity ratio distortion relative to the axisymmetric geometry.

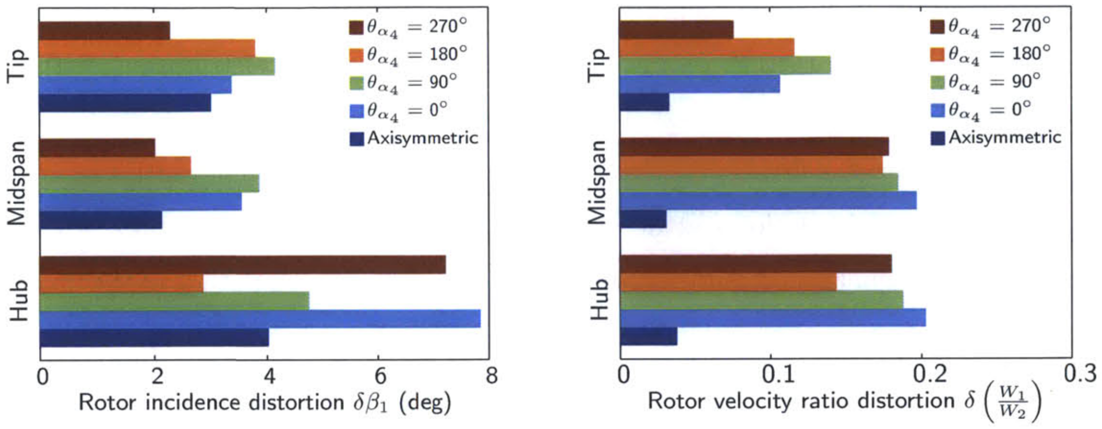

Figure 6-9: Comparison of rotor incidence (left) and velocity ratio (right) distortions for non-axisymmetric stator geometries; stator exit perturbation angle $\delta\alpha_4 = 10°$ can reduce incidence distortion depending on phase, but amplifies velocity ratio distortion in all cases.

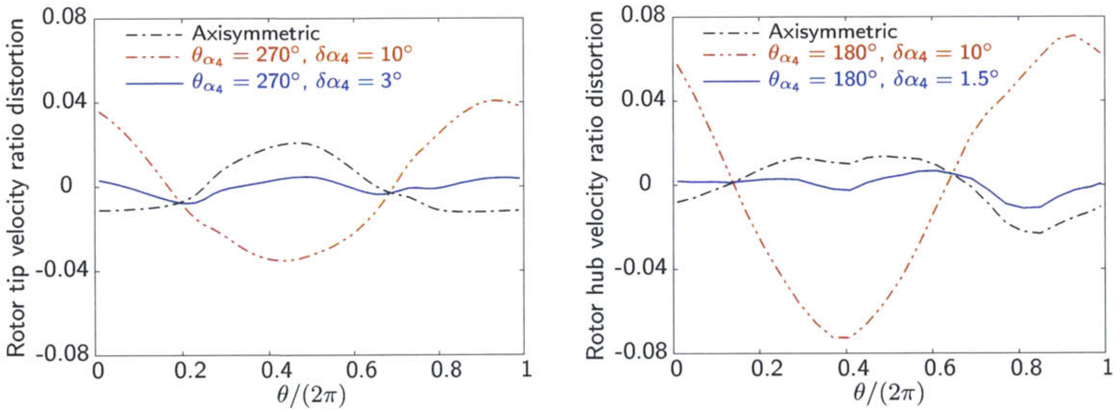

Figure 6-10: Rotor tip (left) and hub (right) velocity ratio distortions for various non-axisymmetric stator geometries; distortion reduction is achieved by scaling stator exit angle based on axisymmetric and non-axisymmetric results assuming linear relation between velocity ratio and exit flow angle variations.

6.3 Discussion

The discussion in Section 6.2 shows how the distortion response in a low hub-to-tip ratio fan stage differs from the two-dimensional results presented in Chapter 4. Specifically, the upstream redistribution results in (three-dimensional) effects which are not captured by the two-dimensional analysis. Downstream of the rotor, however, the flow field is consistent with the two-dimensional analysis. In particular, we see that asymmetry in the stator geometry can have a large effect on stage distortion response.

The rotor performance is mainly determined by the upstream flow redistribution. For a vertically stratified inlet stagnation pressure distribution representative of BLI considered here, distortion-fan interaction results in a top-to-bottom flow redistribution, with both circumferential and radial velocities. The latter are not captured by the two-dimensional analysis in Chapter 4. Further, they result in circumferential non-uniformities in velocity (which impact local blade loss) at all spanwise locations, even near the hub, where the circumferential stagnation pressure non-uniformity is small. The magnitude of the upstream *axial velocity distortion attenuation* and *swirl generation* depend on the stage enthalpy rise and flow coefficient as described by the two-dimensional analysis, and does not change significantly with the changes in the radial loading distribution examined here.

The rotor distortion transfer, rotor-stator interaction, and stator performance are all consistent with the two-dimensional analysis. For given rotor inlet conditions (again, set by the overall stage ϕ and ψ), local increases in rotor enthalpy rise would be expected to result in decreased rotor efficiency because the rotor velocity ratio increases with the flow turning for a given incidence distortion. Conversely, the expected stator efficiency should increase with increases in stagnation enthalpy rise, which result in larger average swirl angles and thus less sensitivity to velocity perturbations. Increasing the axial rotor-stator spacing reduces the rotor back pressure perturbation, which decreases rotor efficiency. It also enables flow redistribution upstream of the stator that decreases the flow angle non-uniformity. The downstream static pressure distribution can be manipulated by changing the stator geometry to produce a non-uniform flow angle distribution. This can affect velocity distortions in both the rotor and stator in a favorable or unfavorable way, depending on both the phase and magnitude of the downstream flow angle distribution.

We can summarize the results of the distortion analysis as follows. Increasing the stagnation enthalpy rise coefficient at fixed ψ/ϕ^2 (i.e., for a fixed propulsive power) reduces the rotor tip section performance, as given by the two-dimensional analysis, but the reduction in co- and counter-swirl creates a reduced velocity ratio distortion near the hub and midspan. These both have an effect on blade row efficiency, and the quantitative changes need to be examined on a case-by-case basis. Changes in the radial stagnation enthalpy rise distribution result in reduced rotor distortion in sections with reduced stagnation enthalpy rise at the cost of increased distortion in sections where the stagnation enthalpy rise is larger. The local stator losses will be reduced for reduced loading, introducing a trade between rotor and stator performance at a given spanwise section. Finally, increasing rotor-stator spacing reduces stator velocity non-uniformities at the cost of increased rotor incidence distortion. The effect is stronger in the stator, and thus there is a potential for a net gain in stage efficiency.

Non-axisymmetric stator geometry can be used to create a stage exit pressure perturbation that produces decreased velocity non-uniformity for a given upstream stagnation pressure non-uniformity. Stator geometries, designed assuming a linear dependence of velocity ratio non-uniformity on stator exit flow angle perturbation, produced 40-50% reduction in rotor velocity ratio distortion at various spanwise locations. Only circumferential variations in stator exit flow angle were considered, but a more detailed design with optimized circumferential and radial distribution of exit flow angle may be able to achieve greater decreases in velocity non-uniformity. Further, the stator inlet metal angle distributions could be optimized to minimize stator losses for the given inlet flow angle (based on the distortion coming out of the rotor) and exit flow angle (tailored to minimize rotor losses) distributions, and thus mitigate the impact of BLI inlet distortion on fan stage performance.

Chapter 7

Summary, Conclusions, and Recommendations

7.1 Summary and Conclusions

1. Boundary layer ingestion (BLI) enables a reduction in required flow power P_K via an increase in propulsive efficiency at fixed fan size. The BLI benefit is due to reduced airframe wake dissipation and propulsor jet dissipation. For commercial aircraft applications, the former is small (approximately 10% of the benefit), and the latter is dominant, with the magnitude depending on the propulsor mass flow. For the D8 aircraft configuration, BLI and non-BLI propulsion systems optimized for minimum fuel burn have approximately equal diameters, and the BLI benefit is thus realized at approximately constant propulsor mass flow.

2. Propulsor simulators for wind tunnel models used to assess BLI benefit should be sized using direct scaling of propulsive efficiency to preserve the behavior of the BLI power savings of full-scale configurations at design Mach numbers. Experimental measurements of model flow power, over a range of representative propulsive efficiencies, in BLI and non-BLI configurations, are consistent with estimates based on mechanical energy analysis, confirming both the BLI benefit and the utility of the power balance analysis.

3. Reduced fan efficiency due to inlet distortion is not a barrier to realizing BLI benefits. For the D8.2 aircraft, fuel burn is estimated to increase 0.8% per 1% decrease in fan

cruise polytropic efficiency, compared to the 14% BLI fuel burn benefit. Previous research [5] has shown fan efficiency decreases of 1-2% with BLI inlet distortion. Further, changes in fan efficiency do not appreciably impact the optimal fan sizing, and the internal and external flow problems can be considered independently.

4. Two- and three-dimensional analyses have been developed to evaluate the response of fan stages to BLI distortion. Comparison of results of the two methods shows a three-dimensional flow description is required to capture the upstream flow redistribution. The rotor inlet conditions and resulting rotor performance can be described in terms of axial and swirl velocity non-uniformities, which, for a given inlet stagnation pressure distribution, depend on the stage stagnation enthalpy rise and flow coefficient. Downstream of the rotor inlet, the qualitative behavior of rotor distortion transfer, rotor-stator interaction, and stator performance are captured by the two-dimensional flow description.

5. Non-axisymmetric stator geometry can potentially mitigate the effect of BLI inlet distortion on fan stage performance. A non-axisymmetric stator exit angle distribution can be designed to reduce velocity non-uniformity in the rotor for a given upstream stagnation pressure distribution, and the stator blading geometry can also be designed to accomodate the stator inlet swirl distortion generated by the rotor.

6. Axisymmetric changes in the fan stage design result in tradeoffs in velocity non-uniformities between different blade sections. Further study is needed to determine whether these changes can yield a benefit in overall fan efficiency.

7.2 Recommendations for Future Work

Stator Design for Distortion Tolerant Fan Stage

Based on the findings, a next step is the design of a three-dimensional stator geometry to reduce losses due to BLI inlet distortion. A possible design process, for a given rotor geometry, would start with simulations using the source term model, then proceed with higher fidelity tools as follows:

1. Develop a non-uniform stator exit flow distribution, using current rotor and stator

source term model descriptions, to select the magnitude and phase of the stator stagger angle, as well as radial variations to minimize rotor flow distortion.

2. Design stator blading geometry based on the distributions of stator inlet and exit flow angles. Steady full-wheel calculations can be implemented with the rotor source term description and the stator blading geometry to evaluate the performance and improve the stator geometry if needed.
3. Conduct computational or experimental assessment of the stator geometry to determine the change in stage efficiency relative to the axisymmetric design.

Modifications to the Source Distribution Analysis

The analysis presented in Chapter 5 gives useful assessments of the sensitivity of non-uniform flow conditions to changes in the turbomachinery design and installation. With modifications, the computational model may be used to determine the effect of other design characteristics (e.g., casing treatments). We propose two immediate steps:

1. Blade loss description: Previous approaches have adequately captured the behavior of fan efficiency using energy and flow-parallel momentum sources as described in Chapter 5 [27]. Incorporation of a boundary layer loss estimate based on local velocity (representing the passage average) and blade loading would enable direct calculation of efficiency rather than relying on inviscid loading parameters as in Chapter 6.
2. Compressible flow: Contemporary fan stages are designed with transonic tip Mach numbers. The relevant BLI distortion mechanisms have been shown to be similar at high and low speed [5], but the details of the flow and the distortion efficiency penalty will likely change for higher Mach number. The analysis should be expanded to capture these effects.

BLI Propulsor Aeromechanics

The results in this thesis, both for the external configuration and the internal flow performance, suggest that increased fan losses due to inlet distortion do not represent a significant obstacle to the design of a BLI aircraft configuration. A more important issue may be the aeromechanical behavior of a BLI fan rotor, because the inlet distortion result in unsteady forces on the blades. Balancing requirements between aerodynamic performance and structural integrity may be challenging because the design that produces the most uniform flow may also have the largest variations in blade force. These issues have not been investigated for the D8 configuration, and this should be done. The source term analysis that has been developed to predict the flow field response also defines the circumferential variations in the blade force, and may thus be useful in early assessment of BLI fan blade structural response.

Appendix A

Two-Dimensional Linearized Flow Distortion Analysis

A.1 Equations of Motion

We begin with the equations of motion for inviscid, incompressible flow on the unrolled annular domain in Figure 4-1,

$$\frac{\partial u}{\partial x} + \frac{\partial v}{\partial y} + \frac{\partial w}{\partial z} = 0, \tag{A.1}$$

$$\frac{\partial (u^2)}{\partial x} + \frac{\partial (uv)}{\partial y} + \frac{\partial (uw)}{\partial z} = -\frac{1}{\rho}\frac{\partial p}{\partial x}, \tag{A.2}$$

$$\frac{\partial (uv)}{\partial x} + \frac{\partial (v^2)}{\partial y} + \frac{\partial (vw)}{\partial z} = -\frac{1}{\rho}\frac{\partial p}{\partial y}, \tag{A.3}$$

$$\frac{\partial (uw)}{\partial x} + \frac{\partial (vw)}{\partial y} + \frac{\partial (w^2)}{\partial z} = -\frac{1}{\rho}\frac{\partial p}{\partial z}. \tag{A.4}$$

The z-coordinate is taken as the direction across the height of the annulus h. For $h \ll R$ and small wall angles ($\frac{dh}{dx} \ll 1$), gradients of flow quantities in the radial direction can be neglected, and the equations of motion are expressed in terms of radially averaged quantites,

$$\overline{f} = \frac{1}{h}\int_0^h f dz. \tag{A.5}$$

Taking the z-integral of Equations (A.1)-(A.4), the equations of motion are reduced to three equations for the radially-averaged axial velocity, tangential velocity, and pressure in two dimensions,

$$\frac{\partial(h\overline{u})}{\partial x} + \frac{\partial(h\overline{v})}{\partial y} = 0, \tag{A.6}$$

$$\overline{u}\frac{\partial\overline{u}}{\partial x} + \overline{v}\frac{\partial\overline{u}}{\partial y} = -\frac{1}{\rho}\frac{\partial\overline{p}}{\partial x}, \tag{A.7}$$

$$\overline{u}\frac{\partial\overline{v}}{\partial x} + \overline{v}\frac{\partial\overline{v}}{\partial y} = -\frac{1}{\rho}\frac{\partial\overline{p}}{\partial y}. \tag{A.8}$$

We now assume small amplitude, two-dimensional perturbations in the radially averaged flow quantities and annulus height about an axisymmetric mean flow and geometry,

$$\overline{u}(x,y) = U(x) + u'(x,y), \tag{A.9}$$

$$\overline{v}(x,y) = V(x) + v'(x,y), \tag{A.10}$$

$$\overline{p}(x,y) = P(x) + p'(x,y), \tag{A.11}$$

$$h(x,y) = H(x) + h'(x,y). \tag{A.12}$$

Integrating Equations (A.6)-(A.8) with respect to y, we arrive at the equations of motion for the axisymmetric mean flow,

$$\frac{d}{dx}\left(U(x)H(x)\right) = 0, \tag{A.13}$$

$$\frac{d}{dx}\left(P(x) + \frac{1}{2}\rho U(x)^2 + \frac{1}{2}\rho V(x)^2\right) = 0, \tag{A.14}$$

$$\frac{d}{dx}\left(V(x)\right) = 0. \tag{A.15}$$

Equation (A.13) is conservation of mass for one-dimensional incompressible passage flow. Equations (A.14) and (A.15) are the momentum equations for axisymmetric swirling flow at constant radius. Equation (A.14) states the stagnation pressure is conserved along streamlines (Bernoulli's equation), and (A.15) states the circulation is constant for fixed R (Kelvin's Theorem).

The equations for the perturbation quantities are obtained by substituting Equation (A.9)-(A.12) into Equations (A.6)-(A.8), eliminating higher order terms, and using Equations (A.13)-(A.15) to eliminate terms that do not depend on perturbation quantities. We also cast the equations in terms of the stagnation pressure perturbation, rather than the static pressure,

$$p_t' = p' + \rho U u' + \rho V v', \tag{A.16}$$

and rearrange to present the equations as a set of equations for the perturbation flow quantities,

$$\frac{\partial u'}{\partial x} = -u'\frac{1}{H}\frac{dH}{dx} - \frac{\partial v'}{\partial y} - \left(\frac{U}{H}\frac{\partial h'}{\partial x} + \frac{V}{H}\frac{\partial h'}{\partial y} + \frac{h'}{H}\frac{dU}{dx}\right), \tag{A.17}$$

$$\frac{\partial v'}{\partial x} = \frac{\partial u'}{\partial y} - \frac{1}{\rho U}\frac{\partial p_t'}{\partial y}, \tag{A.18}$$

$$\frac{\partial p_t'}{\partial x} = -\frac{V}{U}\frac{\partial p_t'}{\partial y}. \tag{A.19}$$

A.2 Numerical Solution

Circumferential variations in the flow field perturbations u', v', p_t', and the annulus height h' can be represented using Fourier series,

$$f(x,y) = \sum_{n=-N}^{N} f_n(x) e^{i\frac{y}{R}}. \tag{A.20}$$

The equations of motion then reduce to a system of $6N$ first order ordinary differential equations for the $2N$ complex fourier coefficients ($f_0 = 0$ for perturbation quantities with a mean of zero) for u', v', and p_t',

$$\frac{\partial u_n'}{\partial x} = -u_n'\frac{1}{H}\frac{dH}{dx} - iv_n' - \left(\frac{U}{H}\frac{\partial h_n'}{\partial x} + i\frac{V}{H}h_n' + \frac{h'}{H}\frac{dU}{dx}\right), \tag{A.21}$$

$$\frac{\partial v_n'}{\partial x} = iu_n' - i\frac{1}{\rho U}p_{t,n}', \tag{A.22}$$

$$\frac{\partial p_{t,n}'}{\partial x} = -i\frac{V}{U}p_{t,n}'. \tag{A.23}$$

Equations (A.21)-(A.23) are integrated numerically using the `ode45` MATLAB function. Separate integrations are performed for the inlet region, rotor-stator gap, and downstream domains, with the inlet stagnation pressure, inlet tangential velocty, and exit static pressure boundary conditions, and changes across the actuator disks described in Chapter 4. The inlet axial velocity is found by solving the residual equation (4.15) using the `fsolve` MATLAB function.

Bibliography

[1] Drela, M., "Making an extraordinary machine better: the D8 aircraft concept." TEDxNewEngland, 2012.

[2] Drela, M., "Power Balance in Aerodynamic Flows," *AIAA Journal*, Vol. 47, No. 7, pp. 1761-1771, July 2009.

[3] Greitzer, E.M., Bonnefoy, P.A., de la Rosa Blanco, E., Dorbian, C.S., Drela, M., Hall, D.K., Hansman, R.J., Hileman, J.I., Liebeck, R.H., Lovegren, J., Mody, P., Pertuze, J.A., Sato, S., Spakovszky, Z.S., Tan, C.S., Hollman, J.S., Duda, J.E., Fitzgerald, N., Houghton, J., Kerrebrock, J.L., Kiwada, G.F., Kordonowy, D., Parrish, J.C., Tylko, J., and Wen, E.A., "N+3 Aircraft Concept Designs and Trade Studies, Final Report – Volume 2: Appendices–Design Methodologies for Aerodynamics, Structures, Weight, and Thermodynamic Cycles," NASA Contractor Report, NASA/CR-2010-216794/VOL2, December 2010.

[4] Greitzer, E.M., "N+3 Phase II Work Plan – Task 1: Assessment of D8.x Propulsion System," internal MIT memorandum, February 2011.

[5] Gunn, E.J., and Hall, C.A., "Aerodynamics of Boundary Layer Ingesting Fans," *Proceedings of ASME Turbo Expo 2014*, GT2014-26142, June 2014.

[6] Gearhart, W.S., Henderson, R.E., "Selection of a Propulsor for a Submersible System," *AIAA J. Aircraft*, Vol. 3, No. 1, pp. 84-90, Jan. 1966.

[7] Goldschmied, F.R., "Integrated Hull Design, Boundary-Layer Control, and Propulsion of Submerged Bodies," *AIAA J. Hydronautics*, Vol. 1, No. 1, pp. 2-11, July 1967.

[8] Betz, A., *Introduction to the Theory of Flow Machines*, First English edition, Pergamon Press, 1966.

[9] Smith, L.H., "Wake Ingestion Propulsion Benefit," *Journal of Propulsion and Power*, Vol. 9, No. 1, pp. 74-82, Feb. 1993.

[10] Diedrich, A., Hileman, J., Tan, D., Willcox, K. and Spakovszky, Z., "Multidisciplinary Design and Optimization of the Silent Aircraft," *44th AIAA Aerospace Sciences Meeting and Exhibit*, January 2006.

[11] Hileman, J.I., Spakovszky, Z.S., Drela M., "Airframe Design for 'Silent Aircraft'," *45th AIAA Aerospace Sciences Meeting and Exhibit*, January 2007.

[12] Hall, C.A., and Crichton, D., "Engine and Installation Configurations for a Silent Aircraft," *17th International Symposium on Airbreathing Engines (ISABE)*, September 2005.

[13] Plas, A.P., Sargeant, M.A., Madani, V., Crichton, D., Greitzer, E.M., Hynes, T.P., and Hall, C.A., "Performance of a Boundary Layer Ingesting (BLI) Propulsion System," *45th AIAA Aerospace Sciences Meeting and Exhibit*, AIAA2007-450, January 2007.

[14] Kawai, R.T., Friedman, D.M., and Serrano, L., "Blended Wing Body (BWB) Boundary Layer Ingestion (BLI) Inlet Configuration and System Studies," NASA Contractor Report, NASA/CR-2006-214534, December 2006.

[15] Hardin, L.W., Tillman, G., and Sharma, O.P, "Aircraft System Study of Boundary Layer Ingesting Propulsion," *48th AIAA/ASME/SAE/ASEE Joing Propulsion Conference & Exhibit*, AIAA2012-3993, July 2012.

[16] Greitzer, E.M., Bonnefoy, P.A., de la Rosa Blanco, E., Dorbian, C.S., Drela, M., Hall, D.K., Hansman, R.J., Hileman, J.I., Liebeck, R.H., Lovegren, J., Mody, P., Pertuze, J.A., Sato, S., Spakovszky, Z.S., Tan, C.S., Hollman, J.S., Duda, J.E., Fitzgerald, N., Houghton, J., Kerrebrock, J.L., Kiwada, G.F., Kordonowy, D., Parrish, J.C., Tylko, J., and Wen, E.A., "N+3 Aircraft Concept Designs and Trade Studies, Final Report – Volume 1," NASA Contractor Report, NASA/CR-2010-216794/VOL1, December 2010.

[17] Drela, M., "Development of the D8 Transport Configuration," *29th AIAA Applied Aerodynamics Conference*, AIAA2011-3970, June 2011.

[18] Sato, S., "The Power Balance Method for Aerodynamic Performance Assessment," Ph.D. Thesis, Massachusetts Institute of Technology, June 2012.

[19] Longley, J.P., Greitzer, E.M., "Inlet Distortion Effects in Aircraft Propulsion System Integration," AGARD Lecture Series 183: Steady and Transient Performance Prediction of Gas Turbine Engines, 1992.

[20] Hynes, T.P., Greitzer, E.M., "A Method for Assessing Effects of Circumferential Flow Distortion on Compressor Stability," *Journal of Turbomachinery*, Vol. 109, July 1987.

[21] Greitzer, E.M., Griswold, H.R., "Compressor-Diffuser Interaction with Circumferential Flow Distortion," *Journal of Mechanical Engineering Science*, Vol. 18, No. 1, pp. 25-38, 1976.

[22] Marble, F., "Three-Dimensional Flow in Turbomachines," *High Speed Aerodynamics and Jet Propulsion,* Hawthorne, W.R., ed., Vol. X, pp. 83-166, Princeton University Press, 1964.

[23] Horlock, J.H. and Marsh, H., "Flow Models for Turbomachines," *Journal Mechanical Engineering Science*, Vol. 13, No. 5, pp. 358-368, 1971.

[24] Gong, Y., Tan, C.S., Gordon, K.A., and Greitzer, E.M., "A Computational Model for Short-Wavelength Stall Inception and Development in Multistage Compressors," *Journal of Turbomachinery*, Vol. 121, Oct. 1999.

[25] Spakovszky, Z., Colas, D., "Propulsion System Integration of Very Quiet Hybrid Wing Body Subsonic Transport," Boeing Contractor Report, April 2011.

[26] Defoe, J.J., Spakovszky, Z.S., "Shock Propagation and MPT Noise From a Transonic Rotor in Nonuniform Flow," *Journal of Turbomachinery*, Vol. 135, Jan. 2013.

[27] Peters, A., Spakovszky, Z.S., Lord, W.K., and Rose, B., "Ultra-Short Nacelles for Low Fan Pressure Ratio Propulsors," *Proceedings of ASME Turbo Expo 2014*, GT2014-26369, June 2014.

[28] Hall, C.A., Crichton, D., "Engine Design Studies for a Silent Aircraft," *Journal of Turbomachinery*, Vol. 129, July 2007.

[29] Crichton, D., Xu, L., and Hall, C.A., "Preliminary Fan Design for a Silent Aircraft," *Journal of Turbomachinery*, Vol. 129, February 2006.

[30] Fidalgo, V.J., Hall, C.A., and Colin, Y., "A Study of Fan-Distortion Interaction Within the NASA Rotor 67 Transonic Stage," *Journal of Turbomachinery*, Vol. 134, May 2012.

[31] Gunn, E.J., Tooze, S.E., Hall, C.A., and Colin, Y., "An Experimental Study of Loss Sources in a Fan Operating with Continuous Inlet Stagnation Pressure Distortion," *Journal of Turbomachinery*, Vol. 135, June 2013.

[32] Florea, R.V., Voytovych, D., Tillman, G., Stucky, M., Shabbir, A., and Sharma, O., "Aerodynamic Analysis of a Boundary-Layer-Ingesting Distortion-Tolerant Fan," *Proceedings of ASME Turbo Expo 2013*, GT2013-94656, June 2013.

[33] Hileman, J.I., Katz, J.B., Mantilla, J.G., and Fleming, G., "Payload Fuel Energy Efficiency as a Metric for Aviation Environmental Performance," *26th International Congress of the Aeronautical Sciences*, 2008.

[34] Uranga, A., Drela, M., Greitzer, E.M., Titchener, N.A., Lieu, M.K., Siu, N.M., Huang, A.C., Gatlin, G.M., and Hannon, J.A., "Preliminary Experimental Assessment of the Boundary Layer Ingestion Benefit for the D8 Aircraft," *52nd Aerospace Sciences Meeting*, AIAA-2014-0906, January 2014.

[35] Siu, N., Casses, C., Huang, A., Uranga, A., Drela, M., and Greitzer, M., "Evaluating Propulsor Mechanical Flow Power in Powered Aircraft Wind Tunnel Experiments," *32nd Applied Aerodynamics Conference*, AIAA-2014-2566, June 2014.

[36] Pandya, S.A., Huang, A., Espitia, A., and Uranga, A., "Computational Assessment of the Boundary Layer Ingesting Nacelle Design of the D8 Aircraft," *52nd Aerspace Sciences Meeting*, AIAA-2014-0907, January 2014.

[37] Drela, M., *A User's Guide to MTFLOW 2.01*, June 2010.

[38] Drela, M., Youngren, H. *A User's Guide to MISES 2.63*, February 2008.

[39] Hughes, C. E., "Aerodynamic Performance of Scale-Model Turbofan Outlet Guide Vanes Designed for Low Noise," *40th AIAA Aerospace Sciences Meeting and Exhibit*, AIAA-2002-0374, January 2002.